Segregation effects in single-crystal fibers grown by the micro-pulling-down method

DISSERTATION

zur Erlangung des akademischen Grades
doctor rerum naturalium
(Dr. rer. nat.)
im Fach Physik

eingereicht an der
Mathematisch-Naturwissenschaftlichen Fakultät I
Humboldt-Universität zu Berlin

von
Dipl.-Phys. Dirk Maier
geboren am 22.4.1977 in Böblingen

Präsident der Humboldt-Universität zu Berlin:
Prof. Dr. Dr. h.c. Christoph Markschies

Dekan der Mathematisch-Naturwissenschaftlichen Fakultät I:
Prof. Dr. Lutz-Helmut Schön

Gutachter:

1. Prof. Dr. Roberto Fornari
2. Prof. Dr. Wolfgang Neumann
3. Prof. Dr. Mauro Tonelli

eingereicht am:	9.9.2008
Tag der mündlichen Prüfung:	20.3.2009

Abstract

Within this study segregations, which occur during micro-pulling-down growth of single-crystal fibers of oxide solid solutions, were analyzed in an experimental and theoretical manner.

Single-crystal fibers of high melting point oxide solid solutions with different equilibrium distribution coefficient k_0 have been grown. As a model system fibers of known binary systems, $(Cr, Al)_2O_3$ ($k_0 = 2$) and $(Ga, Al)_2O_3$ ($k_0 = 0.3$) have been grown. The results of these systems have been compared to material systems relevant for laser applications like $Gd_3(Cr, Ga)_5O_{12}$ ($k_0 > 1$), $(Gd, Yb)_3Ga_5O_{12}$ ($k_0 > 1$), $(Yb, Y)_3Al_5O_{12}$ ($k_0 > 1$) and $(Nd, Y)_3Al_5O_{12}$ ($k_0 < 1$). The radial segregations have been investigated on fibers grown with different melt meniscus heights, pulling speeds and oxygen partial pressures by electron probe microanalysis (EPMA) of the polished cross sections of the grown fibers. The axial segregations have been determined by inductively coupled plasma atomic emission spectrometry (ICP-AES) and EPMA. Growth with a thin melt meniscus of about 30-50 μm between the capillary and fiber and a diameter of the fiber equal to the outer diameter of the capillary leads to a higher or lower dopant concentration in the core of the fiber than in the rim for a $k_0 > 1$ or $k_0 < 1$, respectively. Growth with a higher melt meniscus of 100-150 μm and a diameter of the fiber of about 80% of the outer diameter of the capillary leads to less radial segregations than in the case of growth with a thin melt meniscus. The segregations also depend on the oxygen partial pressure of the growth atmosphere. Low oxygen partial pressures or reducing atmospheres induce a higher amount of suboxides, which are barely incorporated into the growing crystal and therefore influence the equilibrium distribution coefficient. Especially in the case of the $(Cr, Al)_2O_3$ the k_0 is shifted from 1.5 in a CO_2 atmosphere ($p_{O_2} = 20$ mbar) to 0.3 in a N_2 atmosphere ($p_{O_2} = 1 \cdot 10^{-3}$ mbar). This was also confirmed by simulation of the phase diagram. The dopant concentrations along the growth direction are constant which corresponds to an effective distribution coefficient of about 1. An exception is $(Cr, Al)_2O_3$, because the CrO evaporates at a low oxygen partial pressure and therefore a decrease of the Cr_2O_3 concentration could be found along the growth direction in the fiber. The growth front was mapped by pulling down the fiber rapidly and hence quenching the melt zone. In the case of growth with a thin melt meniscus the growth front is strongly bent into the capillary opening. The radial segregations could be explained by the curvature of the growth front. An analytical

approximation solution of the diffusion equation for curved interfaces is similar to the experimentally observed dopant profiles. A fully numerical analysis using the finite element method showed that the segregation profile mainly depends on the curvature of the growth front. The Buoyancy convection is negligible. Thermodiffusion could in principal influence the segregation, but the thermodiffusion factors are unrealistic high for this case. A theoretical model based on irreversible thermodynamics to calculate the thermodiffusion factors using the enthalpy and entropy was derived. This model was verified with published thermodiffusion factors of metals. The influence of thermodiffusion on the segregation profile in the numerical calculations, using the thermodiffusion factors calculated with this model, is negligible.

The segregations also induce mechanical stress in the grown $(Yb, Y)_3Al_5O_{12}$ fibers. Under crossed polarizers strain could be observed mainly for fibers with a considerable Yb_2O_3 segregation profile. For higher pulling rates the interface gets step-like roughened or faceted and the radial segregation and hence the induced strain is then influenced by this non-radial symmetric interface form and corresponds to the crystallographic planes. Ditches will be formed on step edges or facet edges in which supercooled melt is frozen. This frozen melt leads to high stresses and internal cracks in the fibers.

The effect of the effective distribution coefficient of about 1 was shown on the $YLiF_4$ system. Oxofluoride impurities, which are a fact of residual water and oxygen in the growth chamber, are homogeneously distributed along the fiber. There is no self cleaning effect compared to other growth techniques like Czochralski or Bridgman, where an $k_0 \ll 1$ leads to axial segregations and therefore to an increased precipitation of the impurity at the top of the crystal. Therefore, a very high purity atmosphere and source material have to be used in micro-pulling-down growth.

Keywords:
Crystal growth, Segregation, Single-crystal fiber, Oxides

Zusammenfassung

In dieser Arbeit wurden Segregationen, die bei der Züchtung einkristalliner Fasern von Oxidmischkristallsystemen mittels der Micro-Pulling-Down Methode auftreten, experimentell und theoretisch untersucht. Dazu wurden Fasern von hochschmelzenden Oxidmischkristallsystemen mit unterschiedlichen Gleichgewichtsverteilungskoeffizienten k_0 gezüchtet. Als Modellmaterialien wurden zunächst Fasern der bekannten binären Systeme $(Cr, Al)_2O_3$ ($k_0 = 2$) und $(Ga, Al)_2O_3$ ($k_0 = 0.3$) gezüchtet. Diese Erkenntnisse wurden mit für Laseranwendungen interessanten Materialsystemen wie $Gd_{3.05}(Cr, Ga)_{4.95}O_{12}$ ($k_0 > 1$), $(Yb, Gd)_{3.05}Ga_{4.95}O_{12}$ ($k_0 > 1$), $(Yb, Y)_3Al_5O_{12}$ ($k_0 > 1$) und $(Nd, Y)_3Al_5O_{12}$ ($k_0 < 1$) verglichen. Die radialen Segregationen wurden, abhängig von der Schmelzmeniskushöhe, der Ziehgeschwindigkeit und des Sauerstoffpartialdrucks während des Ziehprozesses mittels Elektronenstrahlmikroanalyse an Querschliffen der gezüchteten Fasern bestimmt. Die axialen Segregationen wurden mittels der induktiv gekoppelten Plasma - Atomemissionsspektrometrie (ICP-AES) und EPMA bestimmt. Die Züchtung mit einem nur sehr dünnen Schmelzmeniskus von ungefähr 30-50μm zwischen Tiegelkapillarrohr und Faser, sowie einer Breite der Faser, die der des Aussendurchmessers des Kapillarrohres entspricht, zeigen Fasern mit einem $k_0 > 1$ einen höheren Dotierstoffanteil in der Mitte der Faser, wobei die Fasern mit einem $k_0 < 1$ einen höheren Dotierstoffanteil am Rand zeigen. Die Züchtung mit einem ausgeprägten Schmelzmeniskus von 100-150 μm und einem Faserdurchmesser von 80% des Aussendurchmessers des Kapillarrohres zeigt eine wesentlich geringere radiale Segregation als im Fall der Züchtung mit einem dünnen Schmelzmeniskus. Die radialen Segregationen sind auch abhängig vom Sauerstoffpartialdruck der Züchtungsatmosphäre. Geringe Sauerstoffpartialdrücke oder reduzierende Atmosphären beeinflussen den Gleichgewichtsverteilungskoeffizienten durch einen erhöhten Anteil von Suboxiden, die nur sehr gering in den wachsenden Kristall eingebaut werden. Speziell im Fall des $(Cr, Al)_2O_3$ ($k_0 = 2$) verschiebt sich k_0 von 1.5 in einer CO_2 Atmosphäre ($p_{O_2} = 20\,\text{mbar}$) zu 0.3 in einer N_2 Atmosphäre ($p_{O2} = 1 \cdot 10^{-3}\,\text{mbar}$). Dies wurde auch rechnerisch mittels Phasendiagrammsimulation bestätigt. Die axiale Dotierstoffkonzentration ist in der Regel entlang der Wachstumsrichtung konstant und entspricht einem effektiven Verteilungskoeffizienten von ungefähr 1. Ausnahme ist $(Cr, Al)_2O_3$ bei einem niedrigen Sauerstoffpartialdruck, da CrO abdampft und daher eine axiale Abnahme des Cr_2O_3 Gehaltes entlang der Faser festgestellt wurde. Zusätzlich wurde die Wachstumsfront durch ein schnelles Abziehen der Faser und somit einem Einfrieren

der Schmelze bestimmt. Die Wachstumsfront ist bei einem dünnen Schmelzmeniskus in die Tiegelöffnung gebogen. Die Segregationen lassen sich durch diese Krümmung der Wachstumsfront erklären. Die analytische Näherungslösung der Diffusionsgleichung für gekrümmte Wachstumsfronten liefert ähnliche Dotierstoffprofile wie die experimentell bestimmten. Eine vollständig numerische Modellierung mittels der Finite Elemente Methode ergab, dass die Dotierstoffprofile hauptsächlich durch die Krümmung der Wachstumsfront gegeben sind. Die Buoyancy Konvektion ist vernachlässigbar. Die Marangoni Konvektion beeinflusst das Dotierstoffprofil nur am Rand. Thermodiffusion kann aufgrund der hohen Temperaturgradienten prinzipiell zur Verstärkung der Segregation führen. Allerdings sind die dafür notwendigen Thermodiffusionskoeffizienten unrealistisch hoch. Um die Koeffizienten realistisch abzuschätzen, wurde ein Modell basierend auf der irreversiblen Thermodynamik zur Berechnung der Thermodiffusionskoeffizienten mittels Enthalpie und Entropie hergeleitet. Dieses Modell wurde mit publizierten Messungen an Metallen verglichen und zeigt deutliche Übereinstimmung. Die damit berechneten Werte für die Oxide beeinflussen das Dotierstoffprofil bei den numerischen Rechnungen kaum.

Die Yb_2O_3 Segregationen induzieren Verspannungen in den gezüchteten $(Yb, Y)_3Al_5O_{12}$ Fasern. Unter gekreuzten Polarisatoren kann man Verspannungen hauptsächlich für Fasern mit deutlicher Yb_2O_3 Segregation erkennen. Bei höheren Ziehgeschwindigkeiten kommt es zur stufenähnlichen Vergröberung oder Facettierung der Wachstumsfront. Die radialen Segregationen und die dadurch induzierten Verspannungen sind dann durch die nicht mehr radial symmetrische Wachstumsfront beeinflusst und verhalten sich entsprechend den kristallographischen Ebenen. Ausserdem können sich Gräben an den Stufen- oder Facettenrändern ausbilden, in denen unterkühlte Schmelze eingefroren wird. Diese erzeugt dann erhebliche Verspannungen, die zu Rissen in der Faser führen.

An dem System $YLiF_4$ wurde die Auswirkung des effektiven Verteilungskoeffizenten von ungefähr 1 gezeigt. Oxofluorid Verunreinigungen, die durch Wasser- und Sauerstoffrestanteile im Rezipienten bedingt sind, sind homogen über die gesamte Faser verteilt. Es gibt keinen Selbstreinigungseffekt wie in anderen Züchtungsverfahren (z.B. Czochralski, Bridgman), wo es durch ein $k_0 \ll 1$ zu axialen Segregationen kommt und damit zur verstärkten Ausscheidung der Verunreingung am Anfang des Kristalls. Daher muss bei der Micro-Pulling-Down Züchtung auf eine möglichst reine Atmosphäre und hochreine Ausgangsstoffe geachtet werden.

Schlagwörter:
Kristallzüchtung, Segregation, Einkristallfasern, Oxide

Contents

Chapter 1

Introduction

1.1 Fiber crystals for laser applications

Single-crystal fibers have become the subject of intense research in the last years. The definition of single-crystal fibers are crystalline rods with diameters from the micrometer to millimeter range and a length of a multiple of the diameter. These single-crystal fibers have special characteristics, especially for laser applications.

Usual solid state laser rods have the maximum beam waist in the middle of the rod for a Gaussian beam and because of this only a part of the laser rod is really used as gain medium. Furthermore thermal lensing can arise because heat dissipation is only possible at the surface of the rod. The heat concentrates at the front of the rod, where the pump light is injected and most of the pump power is absorbed. This leads to different refractive indices over the radius of the rod and therefore to beam distortions and lower beam quality. Lowly doped and long single-crystal fibers have pump-light guiding properties and a better surface to volume ratio. Therefore, the heat could be dissipated more effectively to get a homogeneous heat distribution over the fiber. Therefore, it should be possible to increase the pump-power in a fiber setup without damaging the crystal and with less thermal lensing compared to an usual laser rod. [Didierjean et al., 2006] achieved for a two mirror 18 cm cavity laser setup with a 50 mm long 0.2% Nd doped YAG fiber (figure 1.1), pumped with 54 W an output power of 10.1 W. For a Gaussian beam, the waist was 250 μm at middle of the fiber. They also compared by finite element calculations the heat distribution in an usual $3 \times 3 \times 3\,\mathrm{mm}^3$ Nd:YAG laser rod with a Nd-doping of 1% and in a Nd:YAG single-crystal fiber. It can be clearly seen in figure 1.2 that there is a much better thermal management in the fiber than in the usual laser rod.

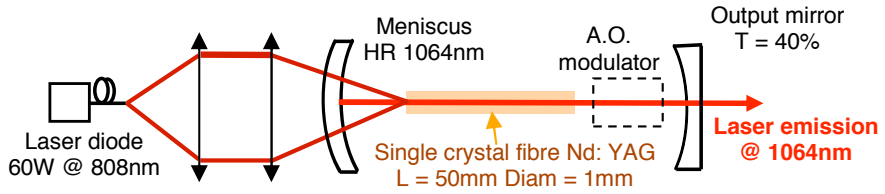

Figure 1.1: Fiber laser setup used by [Didierjean et al., 2006]

The results of [Didierjean et al., 2006] have been obtained for a cavity without guiding the laser light but guiding the pump light. But as-grown fibers often have rough and sometimes faceted surfaces. The light is scattered at these surface faults and leads to power losses and bad beam quality (figure 1.3). To overcome this problem a step or graded refractive index profile could be useful to confine the beam inside the fiber and to select fundamental modes. This also increases the beam quality and gives a better overlap between pump and laser mode [Lo et al., 2002, Siegman, 2003, Digonnet and Graeta, 1985, Bhutta et al., 2002]. A promising segregation effect, which may give a kind of graded index profile was found for micro-pulling-down growth. Uda found radial Mn segregation for Mn doped $LiNbO_3$, which was explained by assuming an interfacial electrical field acting on the different charged ions [Uda et al., 1997]. Ganschow also reported strong radial segregations in the case of olivine fiber growth, which is a solid solution of fayalite (Fe_2SiO_4) and forsterite (Mg_2SiO_4) [Ganschow and Klimm, 2005]. This radial segregation in solid-solution crystals leads to an inner interface between

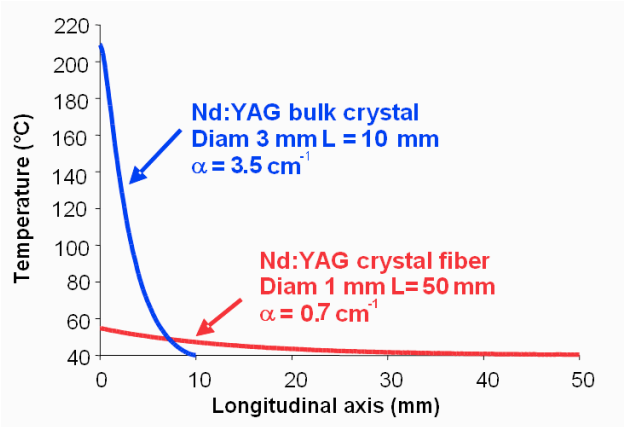

Figure 1.2: Calculated thermal profile to compare a conventional bulk laser rod with a single-crystal fiber setup [Didierjean et al., 2006]

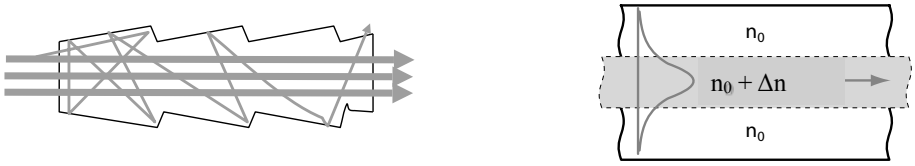

Figure 1.3: The guided light is scattered at faceted and rough surfaces. The beam can be guided in a core with higher refractive index without high scattering losses at the rough surface

a core and a rim region of different composition. This is shown in a backscattered electron image and an electron probe microanalysis scan (figure 1.4a and 1.4b) over the axial cross-section of the fiber reported by Ganschow. This may give different refractive indices for the core and rim region of laser materials, where the laser active ion is concentrated in the core region. In contrast, if one wants to use the fiber as a "conventional" micro laser rod, where the modes are selected by the mirror geometry, this segregation effect may lead to beam distortions, especially if the dopant is concentrated in the rim region. One of the principal goals of this thesis is to study this radial segregation effect, which occurs during micro-pulling-down growth to find conditions for getting a core doped fiber or a radial homogeneous doped

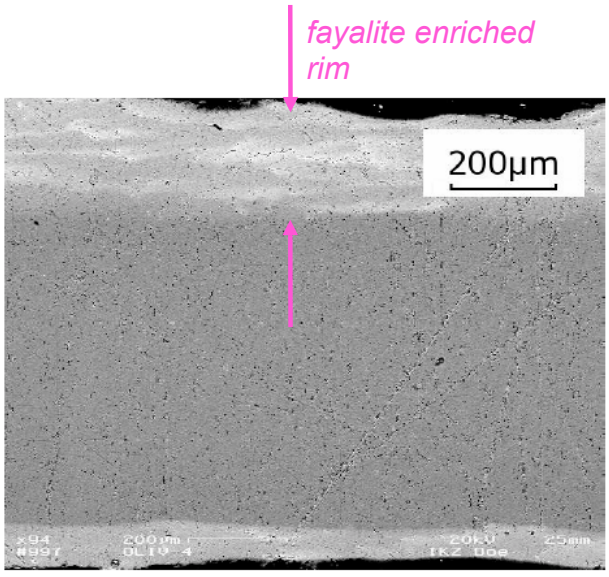

(a) Electron backscattered image

Figure 1.4: (continued)

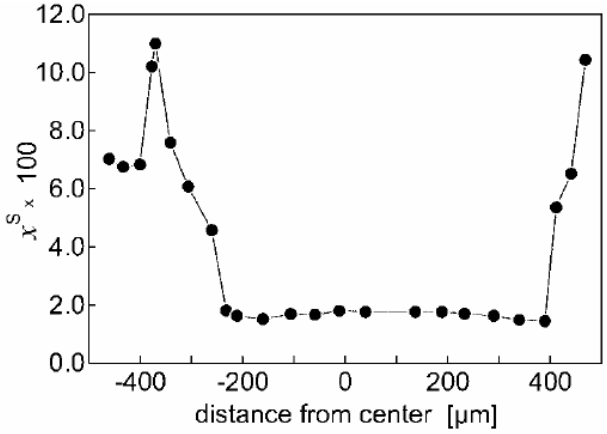

(b) Corresponding radial concentration profile

Figure 1.4: Olivine fiber investigated by [Ganschow and Klimm, 2005]

fiber for potential laser applications.

1.2 Micro-pulling-down method

1.2.1 Setup

The micro-pulling-down method was established at the Fukuda Laboratory [Rudolph and Fukuda, 1999]. Yoon has grown lithium niobate single-crystal fibers by resistively heating a Pt-crucible having a micro nozzle with a capillary opening in the bottom. After a thin seed crystal is touched to the melt at the capillary the fiber is pulled down with velocities in the range 0.5 - 5 mm/min [Yoon et al., 1994]. High temperature gradients of about 1500 K/cm have been measured. Also an inductively heated system for growth of high melting point oxides can be used. For the experiments in

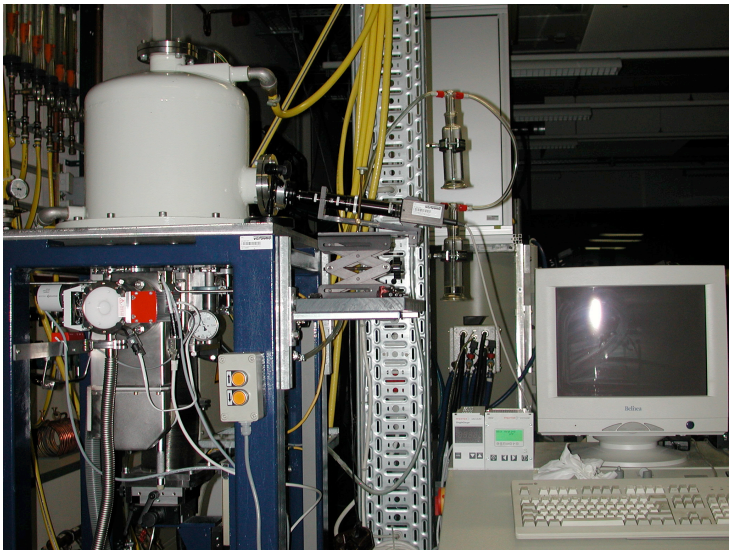

(a) The whole micro-pulling-down machine

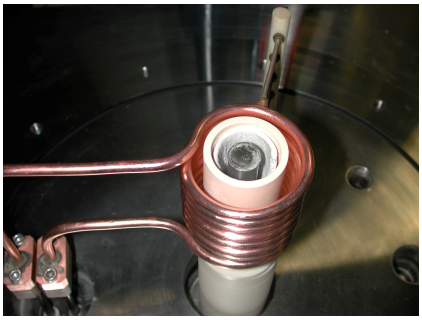

(b) Oxide setup

(c) Fluoride setup

Figure 1.5: Photographs of the setup used in this thesis

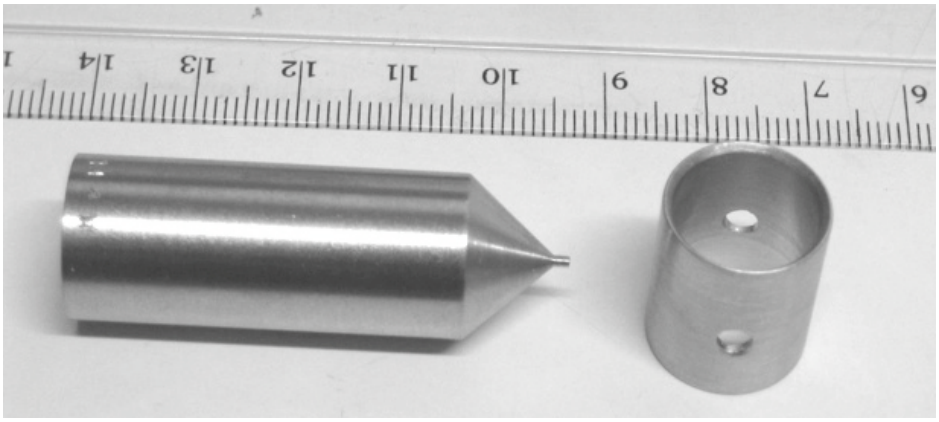

(a) Crucible with an attached capillary and after-heater

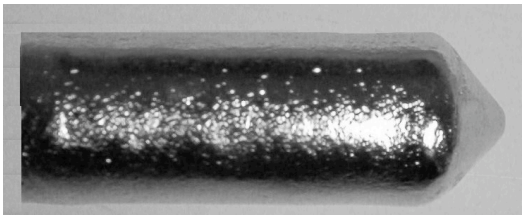

(b) Iridium crucible without an attached capillary

Figure 1.6: Photographs of different crucibles

this thesis only such a system was used. A 5 ml Ir crucible for oxides or a Pt crucible with an attached capillary at the bottom have been put on an after-heater tube with an observation hole (figure 1.6a). The crucible was closed by an Ir lid with a degassing hole in case of oxide growth. For oxide growth this crucible after-heater arrangement was placed on an alumina ceramic pedestal and surrounded by a zirconia fiber mat and a alumina ceramic tube for thermal insulation (figure 1.8 and 1.5b). For fluoride growth the crucible after-heater arrangement was put on a quartz pedestal and surrounded by a quartz tube (figure 1.7 and 1.5c). The heating was in both cases indirectly done by a 10 kW r.f. generator, which could be controlled in 1 W steps manually or by an analog-digital converter (LABJACK UE 9). The whole setup was in a vacuum-tight ($2 \cdot 10^{-6}$ mbar) steel chamber, which is equipped with a Pfeiffer turbo molecular pump for evacuation and a gas in- and outlet (figure 1.5a). Gases can be mixed by a gas manifold composed of needle valves and a flow-meter.

The seeds are made from Laue-oriented Czochralski grown crystals by ultra sonic drilling or wire sawing. The seed crystals were glued into alumina

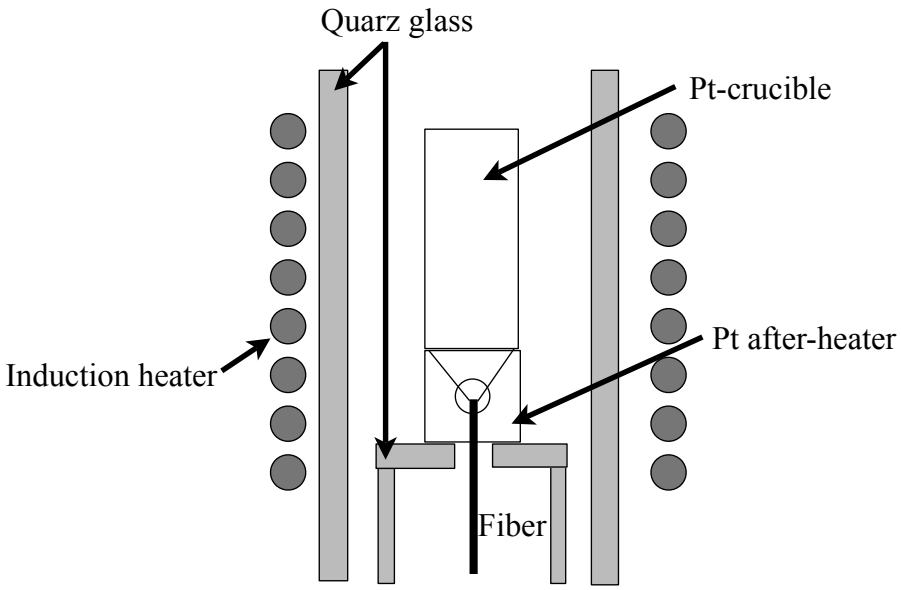

Figure 1.7: Schematic drawing of the setup used for fluorides

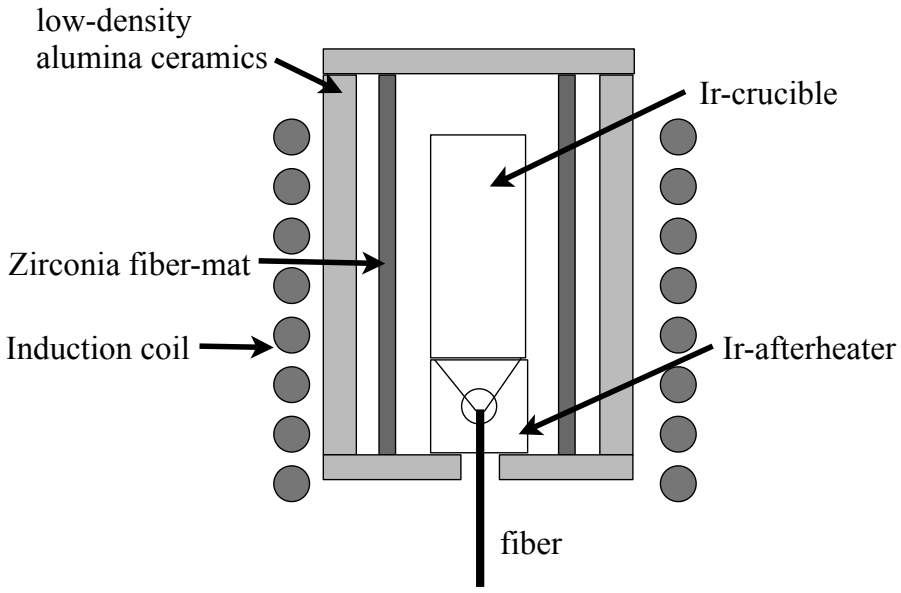

Figure 1.8: Schematic drawing of the setup used for oxides

tubes with alumina glue for oxides or clamped into Pt tubes for fluoride growth.

1.2.2 Control software

The control computer is running SuSE linux version 9.3. The control software was written in python (htp://www.python.org/) and has an TKinter user-interface for controlling all necessary growth parameters and writing a log file. The program is written fully multi-threaded for a better response to inputs. The power control of the rf-generator is done by an analog-digital converter (LABJACK UE 9) addressed over a TCP/IP network connection. The control box of the step motor for pulling is addressed over a serial port connection. Every action is logged into a log file and into the editable log window. The camera output is viewed with the vlc media player (http://videolan.org/) over a bttv-chipset based tv grabber card (figure 1.9). The vlc can also stream the output over the network and so one can observe the growth process remotely. To make the control possible also from another computer the control-software window is shared by the vnc shared app program (http://shared-app-vnc.sourceforge.net/). Therefore, the micro-pulling-down machine can be controlled remotely, using a very low-cost solution with the possibility to write a growth log file, in real time.

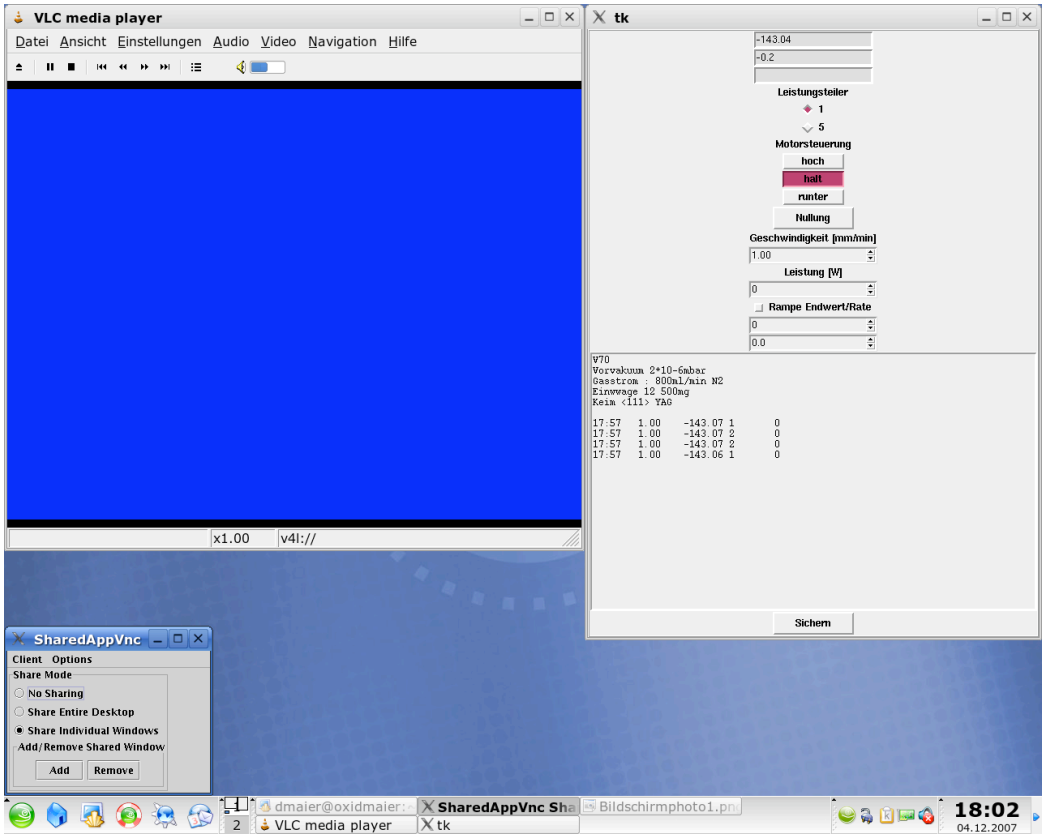

Figure 1.9: Screenshot of the control computer. The vlc media player, the control software, and the VNC shared app program are opened

1.3 Materials

1.3.1 Model materials $(Cr, Al)_2O_3$ and $(Ga, Al)_2O_3$

To study the segregation phenomena simple model materials with melt properties similar to laser materials have been chosen – binary systems of Al_2O_3 with different equilibrium distribution coefficients k_0. The Ga_2O_3 doped Al_2O_3 with a $k_0 \approx 0.3$ (figure 1.18) and Cr_2O_3 doped Al_2O_3 with a oxygen partial pressure depended k_0 ranging from 1.5 for $p_{O_2} = 10^{-2}$ bar to 0.3 for $p_{O_2} = 10^{-8}$ bar (figure 1.10 - 1.17). The phase diagrams in figure 1.10 - 1.17 are calculated using FactSage [GTT, 2007] according to the publication [Degterov and Pelton, 1996], where a thermodynamical assessment of the Cr_2O_3-Al_2O_3 system can be found. The Cr can be in a 2+ and 3+ oxidation state and therefore from the initial Cr_2O_3 concentration an equilibrium of CrO and Cr_2O_3 sets up in the melt depending on the oxygen partial pres-

sure. The Cr_2O_3 has a $k_0 \approx 1.6$ and the CrO is ideally not incorporated in the crystal. Therefore, at oxygen partial pressures, at which the melt contains more CrO than Cr_2O_3, the residual Cr_2O_3 in the melt is still incorporated into the crystal with a $k_0 \approx 1.6$, but based on the initial Cr_2O_3 concentration the total effect is a $k_0 < 1$.

For the experiments in chapter 2 doping concentrations have been chosen, which are low enough to allow moderate pulling speeds without running into constitutional supercooling and high enough to give a significant peak in energy dispersive X-ray spectrometry (EDS) measurements. The doping concentrations used for the experiments in this thesis and the abbreviations of the materials can be found in table 2.1.

1.3.2 Garnet laser materials $Gd_3Ga_5O_{12}$ and $Y_3Al_5O_{12}$

The garnet structure is built from three types of oxygen coordination polyhedra (figure 1.21). This leads to the formula $A_3B_2Z_3O_{12}$. The cation on the A-site is coordinated by 8 oxygen atoms forming a dodecahedron. The B-site is coordinated by a strained oxygen octahedron. The Z-site is coordinated by an oxygen tetrahedron. In rare-earth garnets the octahedral and tetrahedral site is occupied by the same cation like in $Gd_3Ga_5O_{12}$ (GGG) and $Y_3Al_5O_{12}$ (YAG). The laser active ions are placed in the dodecahedral site. The relevant phase diagrams for YAG and GGG are shown in figure 1.19 and 1.20. These are both congruent melting compounds. For the experiments in this thesis Yb_2O_3 was chosen as a dopant for YAG, because of a similar ionic radius of Yb^{3+} to the ionic radius of Y^{3+}. It has an equilibrium distribution coefficient $k_0 > 1$. The dopant concentration was chosen again low enough (5.7 mol% Yb_2O_3) to allow moderate pulling speeds without running into constitutional supercooling and high enough to give a significant peak in EDS measurements. The same is valid for Yb and Cr in GGG. The equilibrium distribution coefficients are both $k_0 > 1$, in the case of Cr even about 3.

In all cases, the compounds and doping concentrations used in this thesis maintain congruent melting behavior as well as the undoped garnet (figure 1.19 and 1.20), even if they are ternary compounds.

1.3.3 $LiYF_4$

Since the 1970's, rare-earth doped $LiYF_4$ is well known as laser-active medium. However, up to now it is still hard to grow even undoped $LiYF_4$ crystals without any inclusions. Many phase diagrams and studies for the melting behavior exist, but the controversy wether the material melts congruently

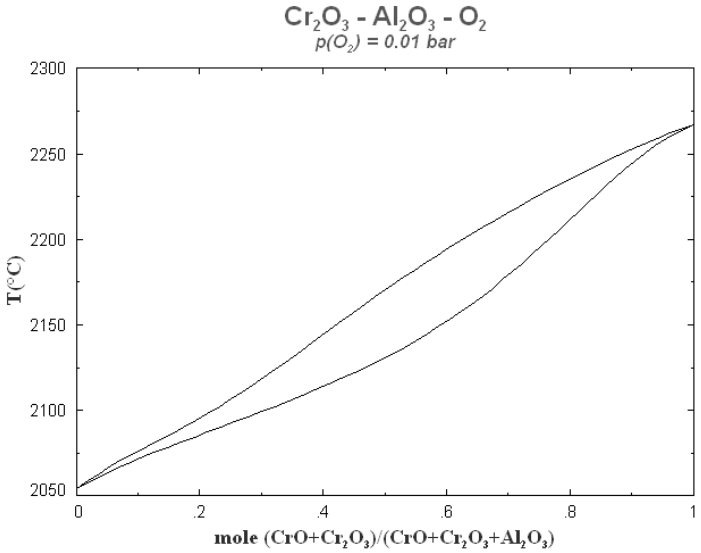

Figure 1.10: Calculated phase diagram of Cr_2O_3 - Al_2O_3 at $p_{O_2} = 10^{-2}$ bar

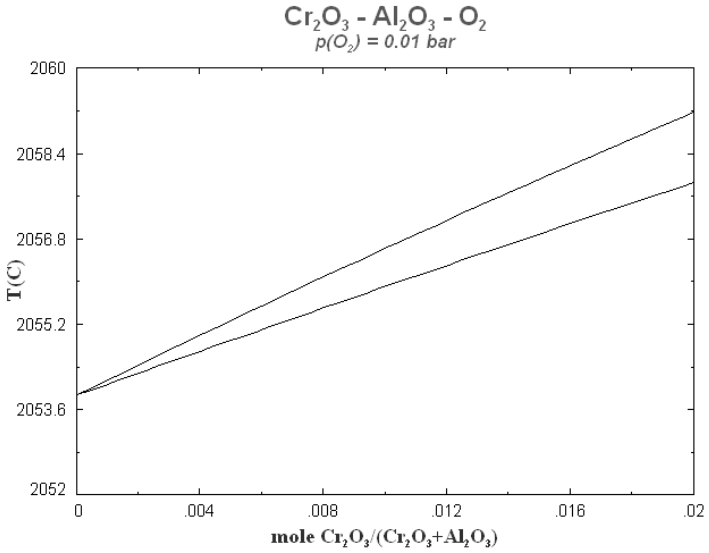

Figure 1.11: Detailed region in the calculated phase diagram of Cr_2O_3 - Al_2O_3 at $p_{O_2} = 10^{-2}$ bar relevant to the experiments in this thesis

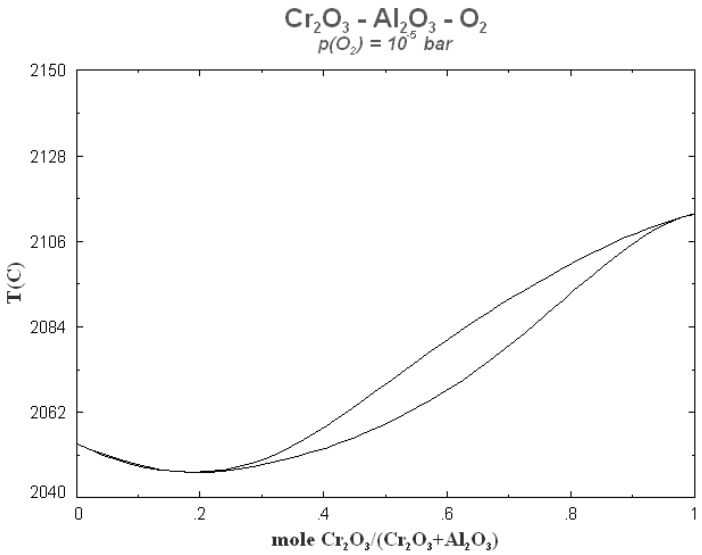

Figure 1.12: Calculated phase diagram of Cr_2O_3 - Al_2O_3 at $p_{O_2} = 10^{-5}$ bar

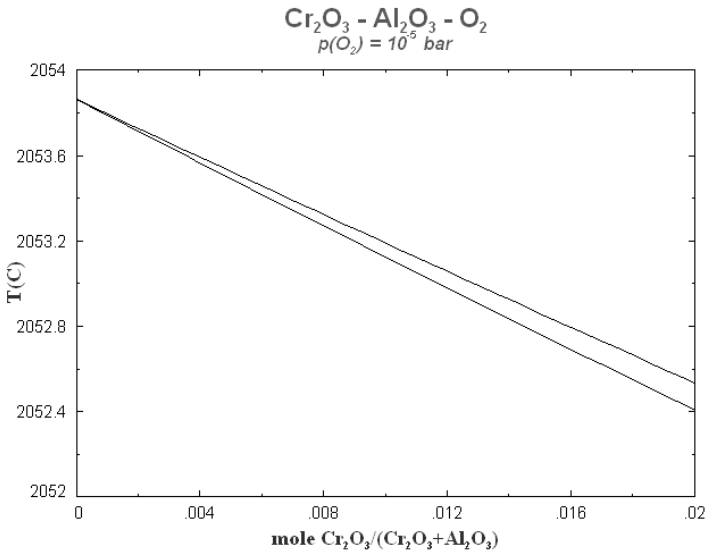

Figure 1.13: Detailed region in the calculated phase diagram of Cr_2O_3 - Al_2O_3 at $p_{O_2} = 10^{-5}$ bar relevant to the experiments in this thesis

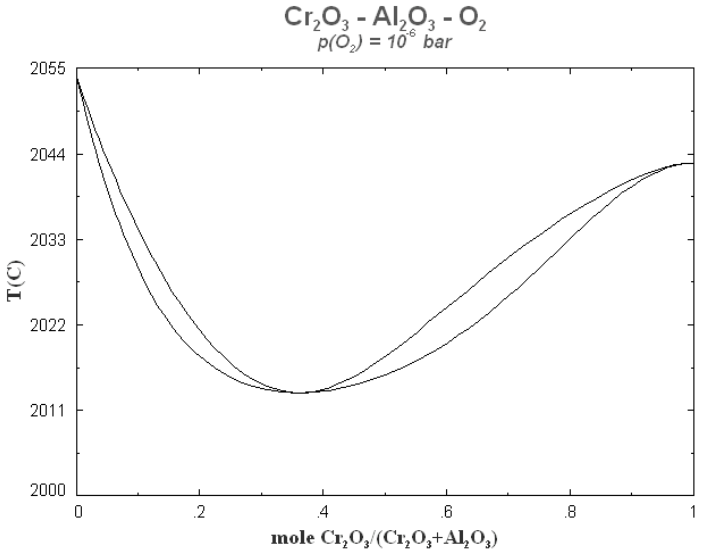

Figure 1.14: Calculated phase diagram of Cr_2O_3 - Al_2O_3 at $p_{O_2} = 10^{-6}$bar

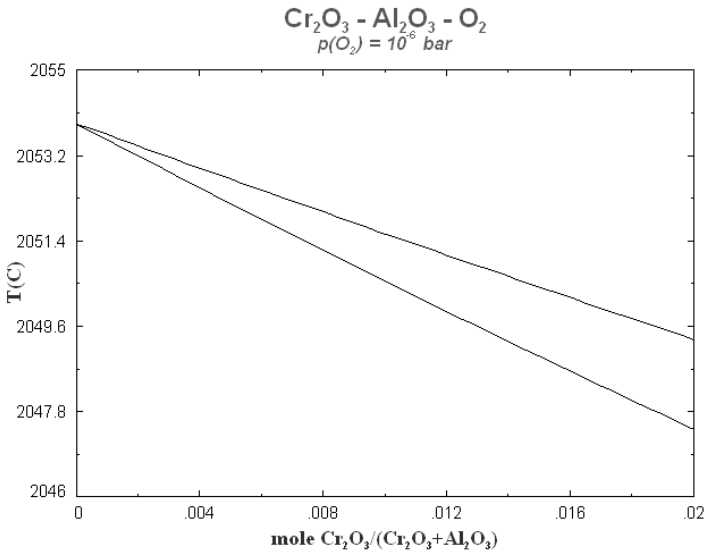

Figure 1.15: Detailed region in the calculated phase diagram of Cr_2O_3 - Al_2O_3 at $p_{O_2} = 10^{-6}$ bar relevant to the experiments in this thesis

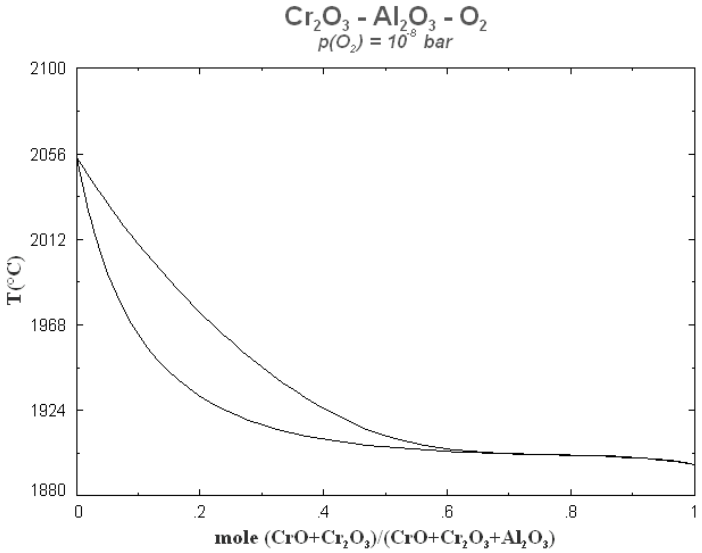

Figure 1.16: Calculated phase diagram of Cr_2O_3 - Al_2O_3 at $p_{O_2} = 10^{-8}$ bar

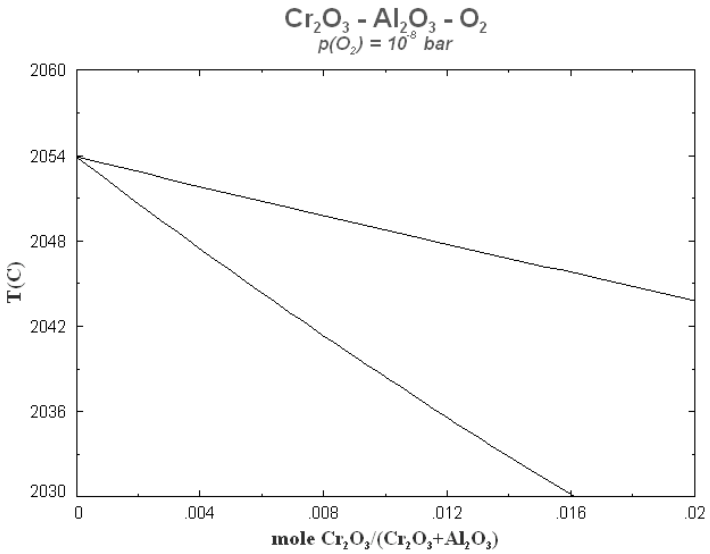

Figure 1.17: Detailed region in the calculated phase diagram of Cr_2O_3 - Al_2O_3 at $p_{O_2} = 10^{-8}$ bar

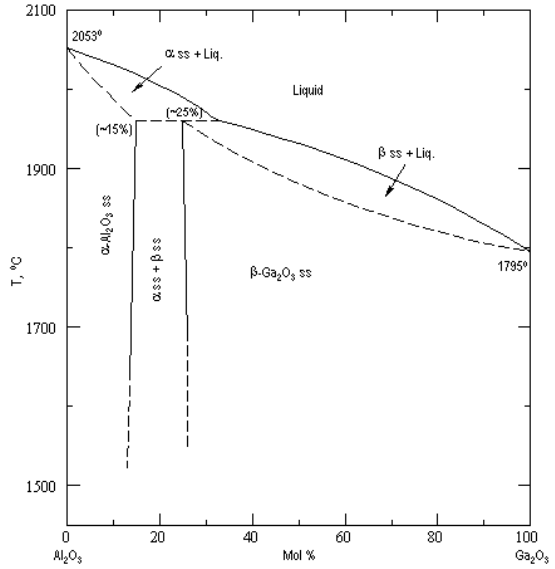

Figure 1.18: Phase diagram of Ga_2O_3 - Al_2O_3 [ACerS-NIST, Version 3.0.1]

or incongruently is still discussed. [Pastor et al., 1975] reported congruent melting of $LiYF_4$ in HF atmosphere. [Abell et al., 1976] reported congruent melting when using high purity starting material and purified Argon atmosphere, while [Thoma et al., 1961] showed in their phase diagram incongruent melting with peritectic point at 52 mol% LiF / 48 mol% YF_3. The Czochralski [Shimamura et al., 2001], Bridgman [Malankiewicz et al., 2005] and micro-pulling-down technique [Santo et al., 2004] have been used to grow $LiYF_4$ using an off-stoichiometric composition. However, except for the reported Czochralski growth [Shimamura et al., 2001], where the atmosphere was purified, the crystals contained some opaque part full of inclusions, which have been assigned to YF_3.

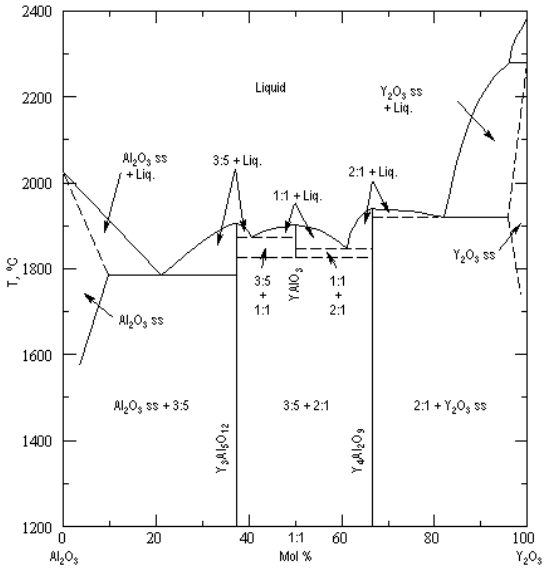

Figure 1.19: Phase diagram of Y_2O_3 - Al_2O_3 [ACerS-NIST, Version 3.0.1]

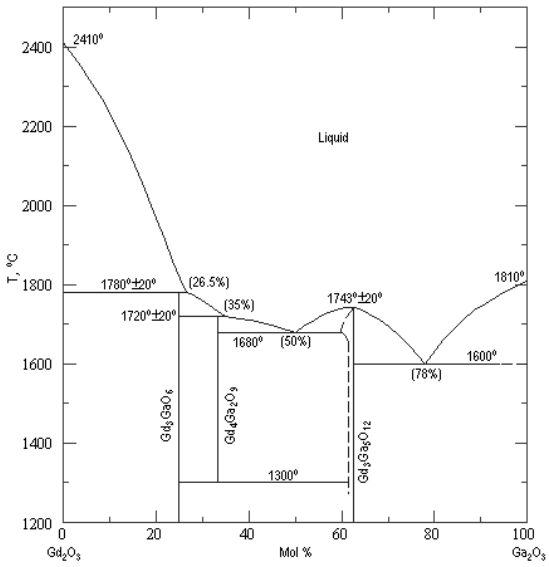

Figure 1.20: Phase diagram of Ga_2O_3 - Gd_2O_3 [ACerS-NIST, Version 3.0.1]

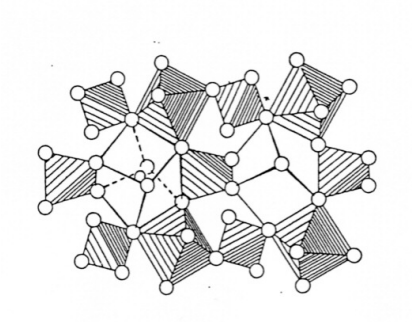

Figure 1.21: Structure of garnets [Gibbs and Smith, 1965]

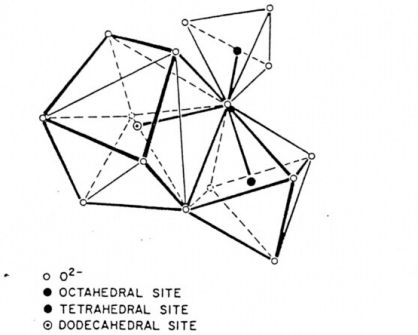

Figure 1.22: Coordination polyhedron of garnets [Nassau, 1980]

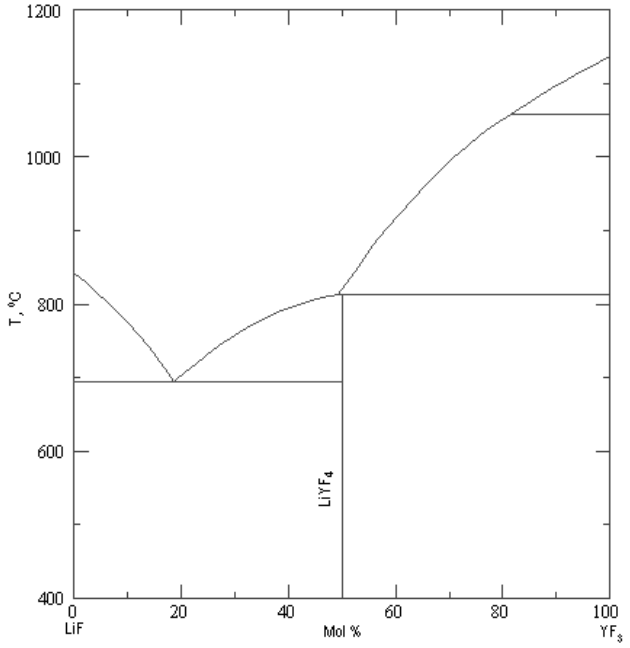

Figure 1.23: Phase diagram of the LiF - YF_3 system [ACerS-NIST, Version 3.0.1]

1.4 Theoretical Background

Mass transport

At steady-state solidification the solid/liquid interface moves with constant speed in the frame of the moving interface ($x = 0$) (figure 1.24a). Any change due to diffusion is compensated exactly by the fact that the interface is advancing, so that

$$D\frac{d^2C}{dx^2} + v\frac{dC}{dx} = 0 \tag{1.1}$$

where v is the solidification front velocity, C the dopant concentration and D the diffusion coefficient in the liquid. The solute diffusive flux next to the interface must equal the rate at which solute is partitioned

$$-D\frac{dC}{dx} = (C_{LS} - C_{SL})\, v \tag{1.2}$$

where C_{SL} is the concentration in the solid at the interface with the liquid and C_{LS} is the concentration in the liquid at the interface with the solid. The solution of this two equations is

$$C(x) = C_{SL} + (C_{LS} - C_{SL})e^{-\frac{x}{D/v}} = C_0 + \frac{C_0(1-k)}{k}e^{-\frac{x}{D/v}} \tag{1.3}$$

where $k = \frac{C_{SL}}{C_{LS}}$ is the equilibrium segregation coefficient. D/v is the diffusion length.

When there is only a diffusive boundary layer of length δ followed by a convectively mixed region (figure 1.24b) the equations are

$$C(x) = C_{SL} + (C_{LS} - C_{SL})e^{-\frac{x}{D/v}}, x \leq \delta \tag{1.4}$$

$$C(x) = C_0, x > \delta \tag{1.5}$$

This was analyzed by [Burton et al., 1953] and gives an effective segregation coefficient

$$k_{eff} = \frac{k_0}{k_0 + (1-k_0)e^{-\frac{v}{D}\delta}} \tag{1.6}$$

This means, if the boundary layer is large compared to the diffusion length one gets a $k_{eff} \approx 1$.

Constitutional supercooling

Solute is partitioned into the liquid ahead of the solidification front. This causes a corresponding variation in the liquidus temperature (the temperature below the freezing begins). Depending on the temperature gradient there

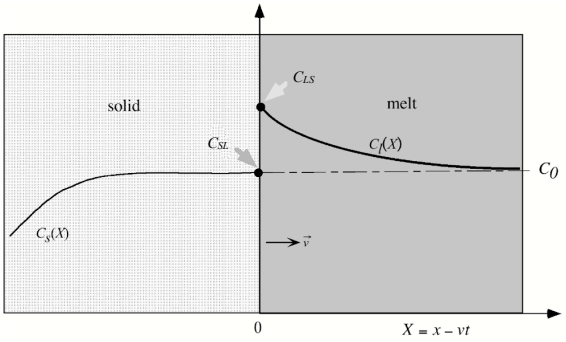

(a) Without convection in the melt

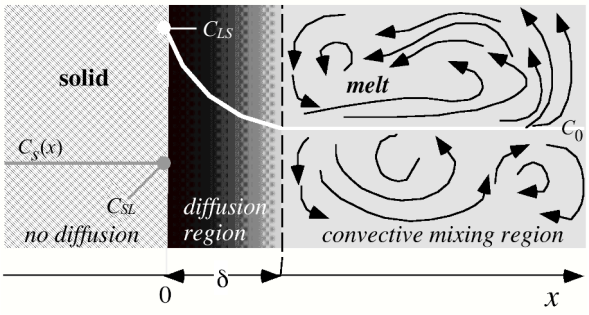

(b) Melt boundary layer of width δ without convection followed by melt with convection

Figure 1.24: Schematic drawings of directional solidification

might be a zone of the melt with a temperature below the liquidus temperature for the specific melt composition. This gives rise to a supercooled zone of liquid ahead of the interface (figure 1.25). This is called constitutional supercooling because it is caused by composition changes. A small perturbation on the interface will therefore expand into a supercooled liquid. This gives rise to cellular structures and in the most critical case to dendrites. It follows that a supercooled zone only occurs when the liquidus temperature (T_L) gradient at the interface is larger than the actual temperature gradient:

$$\left.\frac{\partial T_L}{\partial x}\right|_{x=0} > \frac{\partial T}{\partial x} \tag{1.7}$$

$$m\left.\frac{\partial C_L}{\partial x}\right|_{x=0} > \frac{\partial T}{\partial x} \tag{1.8}$$

where $m = \frac{\partial T_L}{\partial C_L}$ is the magnitude of the slope of the liquidus phase boundary on the phase diagram. With equation 1.2 and 1.3 we can see that the

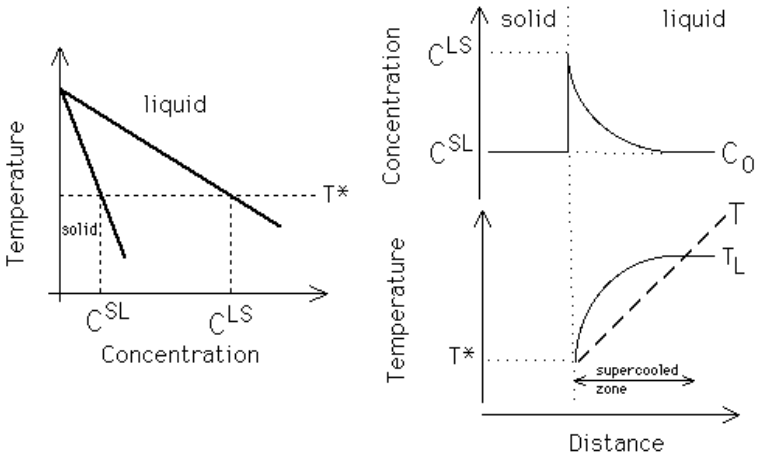

Figure 1.25: Constitutional supercooling demonstrated on the basis of a phase diagram and the concentration profile in the boundary layer. If the temperature gradient is lower than the slope of the liquidus temperature, which corresponds to the concentration profile, a supercooled zone will be formed.

minimum thermal gradient required for a stable solidification front is

$$\frac{\partial T}{\partial x} > \frac{-mC_0(1-k)v}{kD} \tag{1.9}$$

1.5 Analytical methods

1.5.1 Electron probe microanalysis (EPMA)

In the electron microprobe, electrons emitted by an thermal or field emission gun are accelerated by 1-30 kV and scanned over a sample. The electrons interact with the sample and produce secondary and backscattered electrons and X-rays. The secondary electrons are emitted from the surface and can be detected by secondary electron detectors, which are showing surface features. The backscattered electrons are coming from a deeper region of the sample, the interaction volume of 100-1000 nm^3, by elastic scattering processes. The backscattered electron (BSE) detectors yielding images where different phases of differing mean atomic numbers stand out sharply. The X-ray production is the most important case for quantitative analysis. Continuum radiation or "Bremsstrahlung" is produced by inelastic scattering processes and characteristic X-ray energies by energy transitions of electrons

in the atomic shells. The X-rays can be detected by an energy dispersive X-ray spectrometer (EDS) or an wavelength dispersive spectrometer (WDS). The EDS is a liquid nitrogen cooled solid state detector, which collects the X-rays in parallel by 10eV per channel. The resolution is defined by the FWHM of a peak and is around 100-150 eV. Therefore, peak overlaps can occur. A WDS detector consists of a crystal adjusted to the Bragg-angle of the elements characteristic X-ray wavelength. The diffracted X-rays are then counted in a gas-filled proportional counting tube. WDS has a resolution of about 1eV and has a much higher peak to background ratio than EDS. Because of serial analysis about 4 spectrometers are attached to a microprobe to measure 4 elements at the same time. Also higher beam currents are needed to produce more X-rays because of a very small acceptance angle for the X-rays entering into the spectrometer. But the spectrometer can handle higher count rates than EDS and gets therefore better counting statistics in shorter time.

To quantify the production of X-rays in materials a standard is used along with the unknown specimen for purpose of determining the ratio of X-ray intensities in order to eliminate calibrations pertaining to spectrometer efficiency, and second, to scale the ratio of those intensities to the elemental mass fraction within the specimen, seen here

$$\frac{c_i^{sample}}{c_i^{standard}} = \frac{I_i^{sample}}{I_i^{standard}} \tag{1.10}$$

with c_i the mass fractions and I_i the measured intensities of element i. For quantitative analysis several corrections have to be made. First, the background originated from bremsstrahlung has to be subtracted. Then, the intensities of the element peaks have to be corrected for the atomic number (Z), the absorption (A) and fluorescence (F), namely the ZAF correction.

Atomic Number Correction (Z)

The atomic number correction is used to describe electron scattering in specimens of various composition. The two primary mechanisms creating the atomic number effect are changes in trajectory due to high angle scattering that cause little or no reduction in the energy of the electron (elastic scattering) and can result in a significant loss of electrons backscattered out of the sample and hence no longer be involved in the production of characteristic X-rays and in the reduction in energy of the incident electrons involved in various elastic processes such as continuum and characteristic X-ray production as well as phonon, Auger, and secondary electron production.

Absorption Correction (A)

Absorption is often the largest correction made to the X-ray intensities in quantitative microanalysis and therefore the accuracy with which we calculate the correction most directly influences the accuracy of the quantitative results that we may obtain. The absorption is defined as the absorption of an X-ray by the atoms present in the sample. In either case, the most important parameters for the correction are the incident electron energy, the X-ray takeoff angle and the mass attenuation coefficients.

Fluorescence Correction (F)

The fluorescence correction is required due to the fact that not only electrons can cause X- ray fluorescence but X-rays generated by the incident electron beam can also cause additional X-ray fluorescence in other elements that may also be present.

The complete quantification for element i is given by

$$c_i^{sample} = \frac{I_i^{sample}}{I_i^{standard}} \frac{ZAF^{sample}}{ZAF^{standard}} c_i^{standard} \tag{1.11}$$

At this equation, it can be seen that the closer the composition of the standard is to the composition of the sample the better the quantification will be, because the ZAF correction will be for both nearly the same. Therefore, one has to find a standard as similar as possible to the sample which should be measured. The importance of this will be shown in chapter 2.1.2. For the standard-less quantification used in EDS analysis, the standard data is calculated or stored in tables.

1.5.2 Sample preparation for EPMA

The fibers have been roughly cut by a diamond cutter and been fixed into holes on a glass or acrylic-glass disk of 1 inch in diameter. The holes are then filled with methyl methacrylate to embed the sample completely. This is necessary to keep the volume of methyl methacrylate for embedding as small as possible, because it slightly degases carbon-hydrates into the vacuum of the electron microprobe and contaminates the sample and the chamber. The disks are then polished. First, on SiC paper with descending roughness (240, 400, 800) to get a flat and equal surface. Then, the disks were polished with diamond suspension with descending grade (15 μm, 9 μm, 6 μm, 3 μm, 1 μm, 1/4 μm) for 5 minutes each grade on polishing sheets. The disks are then cleaned and coated with a thin carbon layer, by evaporating a carbon wire to get the surface conducting.

1.5.3 Inductively coupled plasma atomic emission spectrometry (ICP-AES)

ICP-AES is a multi-element analysis technique. The sample is milled, dissolved in acid in a micro-wave furnace and introduced into the plasma as a solution. The sample solution is pumped using a peristaltic pump to a nebulizer, where it is converted to a fine spray and mixed with argon in a spray chamber. The purpose of the spray chamber is to make sure that only droplets in a narrow size range make it through into the plasma. Most of the sample drains away from the chamber, the rest is carried into the plasma and instantly excited by the high temperatures (5000-10,000 K) to level where they emit light of a characteristic wavelength. A detector measures the intensity of the emitted light and calculates the concentration of the particular element in the sample. ICP-AES utilises UV and visible spectrometry to image the plasma at the exact wavelength of ionic excitation of the element of interest. Atoms become ionised with 99% efficiency (arsenic and selenium are a couple of exceptions, ionising only at 52% and 33%).

1.6 Numerical method

1.6.1 Finite Element Method (FEM)

The starting point for the finite element method is a mesh, a partition of the geometry into small units of a simple shape. In 2D the subdomains are approximated by mesh elements, which are in FEMLAB [Com, 2007] triangles. Similarly, the boundaries defined in the geometry are partitioned approximately into mesh edges that must conform with the triangles if there is an adjacent subdomain.

With such defined mesh, approximations to the dependent variables can be introduced. Considering a single variable, u, the idea is to approximate u with a function that is described with a finite number of parameters, the so-called degrees of freedom. Inserting this approximation into the weak form of the equation, this generates a system of equations for the degrees of freedom.

For example, consider linear elements in 1D with a mesh consisting of just two mesh intervals $0 < x < 1$ and $1 < x < 2$. Linear elements means that on each mesh interval the continuous function u is linear. To characterize u uniquely the only thing which has to be known is its values at the node points $x_1 = 0$, $x_2 = 1$ and $x_3 = 2$. Denoting these as $U_1 = u(0)$, $U_2 = u(1)$, $U_3 = u(2)$, which are the degrees of freedom. This gives

$$u(x) = U_1\phi_1(x) + U_2\phi_2(x) + U_3\phi_3(x) \tag{1.12}$$

where $\phi_i(x)$ are certain piecewise linear functions. Namely, $\phi_i(x)$ are the basis functions which are linear on each mesh interval, equals 1 at the ith node point, and equals 0 at the other node points. For example,

$$\phi_1(x) = \begin{cases} 1-x & 0 \leq x \leq 1 \\ 0 & 1 \leq x \leq 2 \end{cases} \tag{1.13}$$

The set of functions $u(x)$ is then a linear function space called the finite element space. For better accuracy another finite element space corresponding to quadratic elements can be used. The functions u in this space are second-order polynomials on each mesh interval. To characterize such a function new node points at the midpoint of each mesh interval: $x_4 = 0.5$ and $x_5 = 1.5$ and the corresponding degrees of freedom $U_i = u(x_i)$ are introduced. Therefore, on each mesh interval, the second-degree polynomial $u(x)$ is determined by the degrees of freedom at the endpoints and the midpoint. In fact, you get

$$u(x) = U_1\phi_1(x) + U_2\phi_2(x) + U_3\phi_3(x) + U_4\phi_4(x) + U_5\phi_5(x) \tag{1.14}$$

where the basis functions $\phi_i(x)$ now have a different meaning. Specifically, $\phi_i(x)$ is the function that is quadratic on each mesh interval, equals 1 at the ith node point, and equals 0 at the other node points. For example,

$$\phi_1(x) = \begin{cases} (1-x)(1-2x) & 0 \leq x \leq 1 \\ 0 & 1 \leq x \leq 2 \end{cases} \tag{1.15}$$

In general, a finite element space is specified by giving a set of basis functions. The description of the basis functions is simplified by the introduction of local coordinates. Considering a mesh element of dimension d in an n-dimensional geometry (whose space coordinates are denoted $x_1, ..., x_n$) and also the standard d-dimensional simplex

$$\xi_1 \geq 0, \xi_2 \geq 0, ..., \xi_d \geq 0, \xi_1 + ... + \xi_d \leq 1 \tag{1.16}$$

which resides in the local coordinate space parametrized by the local coordinates $\xi_1 ... \xi_d$. If $d = 1$, then this simplex is the unit interval. If $d = 2$, it is a triangle with two 45 degree angles, and if d = 3 it is a tetrahedron. Now the mesh element can be considered as a linear transformation of the standard simplex. Namely, by letting the global space coordinates x_i be suitable linear functions of the local coordinates, the mesh element is the image of the standard simplex. When described in terms of local coordinates, the basis functions assume one of a few basic shapes. These are the shape functions. In the example with linear elements in 1D, any basis function on any mesh element is one of the following:

$$\Phi = \xi_1, \Phi = 1 - \xi_1, \Phi = 0 \tag{1.17}$$

Thus, the first two are the shape functions in this example (0 is not counted as a shape function). In the example with quadratic elements in 1D, the shape functions are

$$\Phi = (1 - \xi_1)(1 - 2\xi_1), \Phi = 4\xi_1(1 - \xi_1), \Phi = \xi_1(2\xi_1 - 1) \tag{1.18}$$

The Lagrange element

The preceding examples are special cases of the Lagrange element. With a positive integer k, the order of the Lagrange element, the functions u in this finite element space are piecewise polynomials of degree k. That means, on each mesh element u is a polynomial of degree k. To describe such a function it suffices to give its values in the Lagrange points of order k. These are the points whose local coordinates and are integer multiples of $1/k$. For example, for a triangular mesh in 2D with $k = 2$, this means that there are node points at the corners and side midpoints of all mesh triangles. For each of these node points p_i, there exists a degree of freedom $U_i = p_i$ and a basis function ϕ_i. The restriction of the basis function ϕ_i to a mesh element is a polynomial of degree k in the local coordinates such that $\phi_i = 1$ at node i, and $\phi_i = 0$ at all other nodes. Thus, the basis functions are continuous and u becomes

$$u = \sum_i U_i \phi_i \tag{1.19}$$

Curved mesh elements

When using higher-order elements (that is, elements of an order > 1), the solution has a smaller error. The error also depends on how well the mesh approximates the true boundary. To keep errors in the finite element approximation and the boundary approximation at the same level, it is wise to use curved mesh elements. They are distorted mesh elements that can approximate a boundary better than ordinary straight elements (if the problem‘s boundary is curved). Curved mesh elements are elements that can be achieved by writing the global coordinates x_ii as polynomials of order k (the geometry shape order) in the local coordinates ξ_j. For mesh elements that do not touch the boundary, there is no reason to make them curved, so they are straight.

Discretization of the Equations

The starting point is the weak formulation of the problem. The discretization of the constraints is

$$0 = R^2 \text{ on subdomain } \Omega \tag{1.20}$$
$$0 = R^1 \text{ on boundary } B \tag{1.21}$$
$$0 = R^0 \text{ on point } P \tag{1.22}$$

where R is the constraint vector. For each mesh element in B (that is, each mesh edge in B), with the Lagrange points of some order k denoted by $x^{(1)}_{mj}$, where m is the index of the mesh element, the discretization of the constraint is

$$0 = R^{(1)}(x^{(1)}_{mj}) \tag{1.23}$$

This means, the constraints must hold pointwise at the Lagrange points. The Lagrange point order k can be chosen differently for various components of the constraint vector R^B, and it can also vary in space. The constraints on subdomains Ω and points P are discretized in the same way. These pointwise constraints are collected in one equation $0 = M$, where M is the vector consisting of all the right-hand sides. M depends only on U, the vector with the degrees of freedoms U_i as its components, so the constraints can be written $0 = M(U)$.

The weak equation:

$$\begin{aligned} 0 = &\int_\Omega W^{(2)} dA + \int_B W^{(1)} ds + \sum_P W^{(0)} \\ &- \int_\Omega v \cdot h^{(2)T} \mu^{(2)} dA + \int_B v \cdot h^{(1)T} \mu^{(1)} ds + \sum_P v \cdot h^{(0)T} \mu^{(0)} \end{aligned} \tag{1.24}$$

where $h = \partial R / \partial u$ and μ is the Lagrange multiplier, can be discretized by expressing the dependent variables in terms of the degrees of freedom. Similarly, the test functions are approximated with the same finite elements (this is the Galerkin method):

$$v_l = \sum_i V_i \phi^{(l)}_i \tag{1.25}$$

Because the test functions occur linearly in the integrands of the weak equation, it is enough to require that the weak equation holds when the test functions are chosen as basis functions:

$$v_l = \phi^{(l)}_i \tag{1.26}$$

When substituted into the weak equation, this gives one equation for each i. Now the Lagrange multipliers must be discretized. Let

$$\Delta_{mj}^{(d)} = \mu^{(d)}(x_{mj}^{(d)})\omega_{mj}^{(d)} \tag{1.27}$$

where $x_{mj}^{(d)}$ are the Lagrange points defined earlier, and $\omega_{mj}^{(d)}$ are certain weights. The term

$$\int_B \phi_i \cdot h^{(1)T}\mu^{(1)} ds \tag{1.28}$$

is approximated as a sum over all mesh elements in B. The contribution from mesh element number m to this sum is approximated with the Riemann sum

$$\sum_j \phi_i(x_{mj}^{(1)})h^{(1)T}(x_{mj}^{(1)})\mu^{(1)}(x_{mj}^{(1)})\omega_{mj}^{(1)} = \sum_j \phi_i(x_{mj}^{(1)})h^{(1)T}(x_{mj}^{(1)})\Delta_{mj}^{(1)} \tag{1.29}$$

where $\omega_{mj}^{(1)}$ is the length (or integral of ds) over the appropriate part of the mesh element. The integral over Ω and the sum over P is approximated similarly. All this means that the discretization of the weak equation is

$$0 = L - N^T\Delta \tag{1.30}$$

where L is a vector whose ith component is

$$\int_\Omega W^{(2)} dA + \int_B W^{(1)} ds + \sum_P W^{(0)} \tag{1.31}$$

evaluated for $v = \phi_i^{(l)}$. Δ is the vector containing all the discretized Lagrange multipliers $\Delta_{mj}^{(d)}$. N is a matrix whose i^{th} column is a concatenation of the vectors

$$h^{(d)T}(x_{mj}^{(d)})\phi_{mj}^{(d)} \tag{1.32}$$

For problems given in general or weak form, N is the Jacobian of M:

$$-N = \frac{\partial M}{\partial U} \tag{1.33}$$

To sum up, the discretization of the stationary problem is

$$0 = L(U) - N(U)^T\Delta \tag{1.34}$$

$$0 = M(U) \tag{1.35}$$

This system has to be solved for the solution vector U and the Lagrange multiplier vector Δ. L is called the residual vector, M is the constraint residual, and N is the constraint matrix.

Numerical quadrature

The integrals occurring in the components of the residual vector L as well as K are computed approximately using a quadrature formula. Such a formula computes the integral over a mesh element by taking a weighted sum of the integrand evaluated in a finite number of points in the mesh element. The order of a quadrature formula on a 1D, triangular, or tetrahedral element is the maximum number k such that it exactly integrates all polynomials of degree k. For a quadrilateral element, a formula of order k integrates exactly all products $p(\xi_1)q(\xi_2)$, where p and q are polynomials of degree k in the first and second local coordinates, respectively. A similar definition holds for hexahedral and prism elements. Thus, the accuracy of the quadrature increases with the order. On the other hand, the number of evaluation points also increases with the order.

Weak Form

A stationary PDE problem for a single dependent variable, u, in two space dimensions

$$\nabla \cdot \Gamma = F \tag{1.36}$$

with $\Gamma = -a\nabla u - bu + c$ and $F = f - d\nabla u - eu$ where a, b, c, d, e, f are constants. Multiplying the PDE with an arbitrary test function v and integrating leads to

$$\int_\Omega v\nabla \cdot \Gamma dA = \int_\Omega vF dA \tag{1.37}$$

where dA is the area element. With Green‘s formula (Gauss‘ formula) to integrate by parts it gives

$$\int_{\partial\Omega} v\Gamma \cdot \vec{n} ds - \int_\Omega \nabla v \cdot \Gamma dA = \int_\Omega vF dA \tag{1.38}$$

where ds is the length element. With the Neumann boundary condition

$$-\vec{n} \cdot \Gamma = G + \frac{\partial R}{\partial u}\mu \tag{1.39}$$

it gives the following equation:

$$0 = \int_\Omega (\nabla v \cdot \Gamma + vF)dA + \int_{\partial\Omega} v\left(G + \frac{\partial R}{\partial u}\mu\right) ds \tag{1.40}$$

Together with the Dirichlet condition, this is a weak reformulation of the original PDE problem. The requirement is that the above weak equation should hold for all test functions v. If the functions u and μ satisfy the weak

formulation, then they also satisfy the original formulation. However, this holds true only if the solutions and coefficients are sufficiently smooth. For instance, in the case of discontinuities in material properties, you can have a solution of the weak formulation while the strong formulation has no meaning. The names "weak" and "strong" stem from this distinction: the weak formulation is a weaker condition on the solution than the strong formulation. A benefit of the weak formulation is that it requires less regularity of Γ. This is important in the finite element method.

Weak constraints can be implemented by using finite elements on the constraint domain for the Lagrange multipliers, and by solving for the Lagrange multipliers along with the original problem.

Chapter 2

Experimental

2.1 Experimental observation of dopant segregation in oxide fibers

2.1.1 Growth conditions

The starting materials (see table 2.1) were prepared from 4N Al_2O_3, Cr_2O_3, Ga_2O_3, Gd_2O_3, Y_2O_3 and Yb_2O_3 powders by grinding a total weight of 5g in a plastic mortar, pressing into pellets and sintering at 2/3 of the melting temperature in platinum-gold crucibles. Then, the fibers were grown in the micro-pulling-down apparatus described in chapter 1.2.1 using 500 mg of the starting material. The growth chamber was evacuated before each experiment to $2.5 \cdot 10^{-6}$ mbar and then filled with gas. During growth a constant gas flow of about 900 ml/min was kept.

The axial temperature profile was measured for $(Cr, Al)_2O_3$ and Yb:YAG

Abbreviation	Chemical formula	dopant conc. [mol%]	k_0^*
$(Cr, Al)_2O_3$	$(Cr, Al)_2O_3$	1.75% Cr_2O_3	0.3-1.5
$(Ga, Al)_2O_3$	$(Ga, Al)_2O_3$	1.5% Ga_2O_3	0.3
Cr:GGG	$Gd_{3.05}(Cr, Ga)_{4.95}O_{12}$	1.75% Cr_2O_3	≈ 3
Yb:GGG	$(Yb, Gd)_{3.05}(Cr, Ga)_{4.95}O_{12}$	5% Yb_2O_3	>1
Yb:YAG	$(Yb, Y)_3Al_5O_{12}$	5.7% Yb_2O_3	>1
Nd:YAG	$(Nd, Y)_3Al_5O_{12}$	1.5% Nd_2O_3	< 1

Table 2.1: Starting melt compositions and the corresponding equilibrium distribution coefficients used for the oxide fibers. (* values taken from section 1.3)

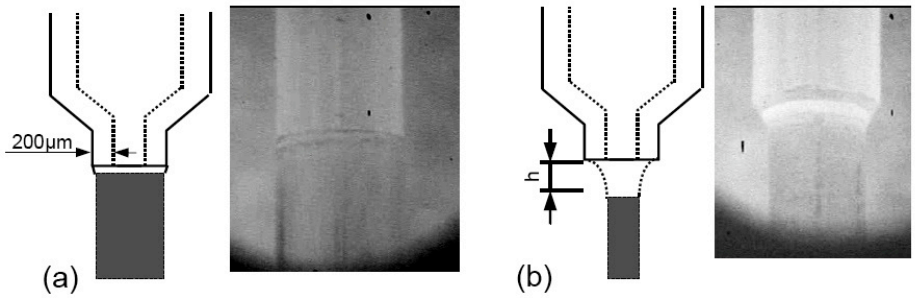

Figure 2.1: Photographs and schematic drawing of the two different growth modes. (a) Type 1 growth with a small meniscus of 30-100μm and (b) Type 2 growth with a considerable meniscus greater than 100 μm

(figure 2.2) to estimate the temperature gradient close to the growth front. This is necessary to estimate the maximum allowed pulling rate by Tiller's criterion (equation 1.9). It was seeded with a W5Re/W26Re thermocouple, consisting of a W5Re and a W26Re wire, each 30μm in diameter, placed in an alumina capillary and connected directly at the top of the capillary. Then it was pulled down with a speed of 0.5 mm/min and the temperature was measured every 0.5 mm. The temperature gradient in front of the growth front was then determined to 400 K/cm and 230 K/cm for $(Cr, Al)_2O_3$ and Yb:YAG, respectively. This leads according to Tiller's criterion (equation 1.9) to an estimated maximum pulling rate of about 0.7 mm/min and 0.35 mm/min for $(Cr, Al)_2O_3$ ($D_{Cr} = 2 \cdot 10^{-5}\,cm^{-2}$) and Yb:YAG ($D_{Yb} = 5 \cdot 10^{-6}\,cm^{-2}$), respectively. The diffusion coefficients mentioned have been estimated by the numerical study in chapter 3. If the pulling rate is much higher, cellular structures of dopant inclusions are formed. This can be seen for $(Cr, Al)_2O_3$ grown with 2 mm/min in figure 2.3, for example. To study the effect of the oxygen partial pressure on the dopant segregation different gases have been used. For the model material $(Cr, Al)_2O_3$, which is according

Abbreviation	Growth rates [mm/min]	growth type
$(Cr, Al)_2O_3$	0.5	1 + 2
$(Ga, Al)_2O_3$	0.3	1 + 2
Cr:GGG	0.3	1
Yb:GGG	0.3	1
Yb:YAG	0.01, 0.1, 0.3, 0.5	1 + 2

Table 2.2: Growth rates and growth types used for the oxide fibers.

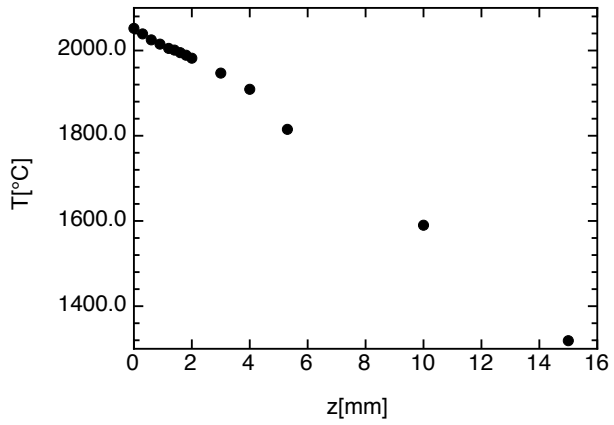

(a) $(Cr, Al)_2O_3$

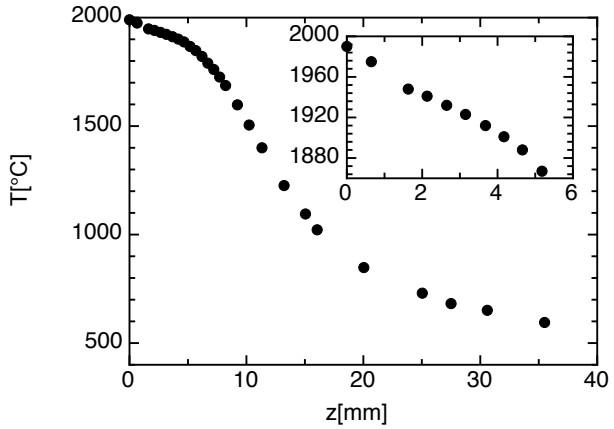

(b) Yb:YAG

Figure 2.2: Temperature profile measured by seeding on an W5Re/W26Re thermocouple and pulling with 0.5 mm/min

to the phase diagram very sensitive to the oxygen partial pressure, N_2 of 5N purity (99.999 %) and CO_2 gas have been used. The 5N N_2 has an oxygen partial pressure p_{O_2} of around $2 \cdot 10^{-6}$ bar when we consider the residual impurities as air. In case of CO_2 at temperatures above 1600°C the reaction

$$CO_2 \rightleftharpoons CO + \frac{1}{2}O_2 \tag{2.1}$$

supplies O_2. At 2000°C the oxygen partial pressure is around $p_{O_2} \approx 2 \cdot 10^{-2}$ bar. The use of Ir crucibles is limited to a maximum of an oxygen partial pressure of $p_{O_2} = 2 \cdot 10^{-2}$ bar at 2000°C, because the Ir reacts with oxygen to the volatile IrO_2 which condenses as tinsel on the crystal surface.

Figure 2.3: Half cross section of a $(Cr, Al)_2O_3$ fiber grown with too high pulling rate of 2 mm/min. Cellular structures of inclusions are formed

To suppress the reduction of Ga_2O_3 to the volatile Ga_2O and to keep the oxidation of Ir to volatile IrO_2 as low as possible, about 50% CO_2 was added to the N_2 for growth of $(Ga, Al)_2O_3$, Cr:GGG and Yb:GGG . To study the effect of a reducing atmosphere on Yb:YAG, 10% of forming gas (5% H_2, 95% N_2) in N_2 was used.

To get the dopant distributions as reproducible as possible it was important to have a flat crucible nozzle. This was done by polishing the crucible nozzle with 3 μm diamond paste on a glass plate. During growth the height of the molten zone was carefully controlled by manually increasing or decreasing the rf-power. Two growth arrangements with different heights of the molten zone have been selected by adjusting the rf-power. Type 1 with only a melt film of about 30-70μm between crucible nozzle and crystal and a crystal diameter equal to the capillary outer diameter (figure 2.1(a)). Type 2 with a considerable meniscus of about 150μm height and a crystal diameter of about 85% of the capillary outer diameter (figure 2.1(b)). The growth arrangements and pulling speeds used for the different materials is listed in table 2.2. Radial and axial cross-sections of the grown fibers have been prepared and concentration profiles were determined by EPMA.

2.1.2 Standardization of garnet materials for EPMA

For garnets like YAG and GGG compound standards are commercially available. These materials are doped with several mol% of Yb_2O_3 in the experiments for this thesis, which is a substitution of Y by Yb. Using a commercial

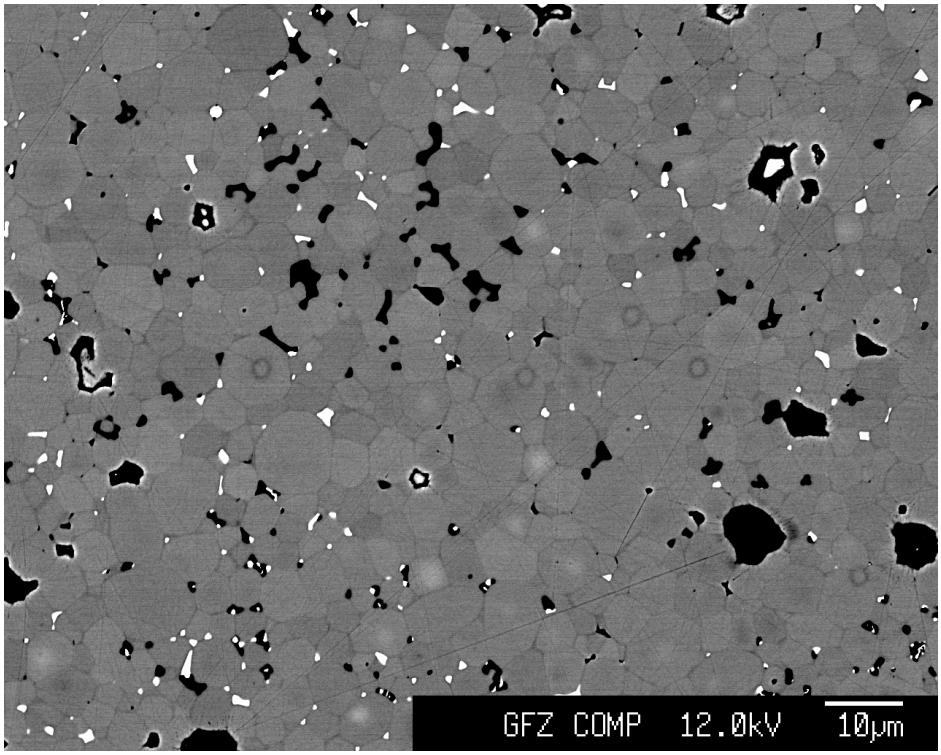

Figure 2.4: BSE image of the ceramic standard sample. White points are Zr particles from abrasion of the Zr-ball mill.

$YbPO_4$ or Yb-glass standard combined with a commercial host material standard, or only using commercial phosphate standards leads nearly independent of acceleration voltage to a wrong $Al/(Yb + Y)$ or $Ga/(Gd + Yb)$ cation ratio in measured samples compared to the ideal 5/3 cation ratio of garnets. This was found for the Yb:YAG and Yb:GGG single-crystal fibers measured by WDS or EDS. The following study is performed on a JEOL Hyperprobe 8500F thermal field-emission electron microprobe with four WDS detectors. But a difference in cation ratio to the ideal garnet cation ratio is discussed as a local source of strain in these materials [Kitamura et al., 1983]. Therefore, reliable concentration measurements with high spatial resolution are needed, especially in reference to paragraph 2.1.4. The fibers were also measured by ICP-AES in an average volume to get the average cation ratio, which was found to be close to the ideal 3/5 garnet ratio ($Y_{2.52}Yb_{0.43}Al_{5.05}O_{12}$). This average volume measurement can be compared to local electron probe microanalysis measurements, because the measured cation ratios also do not change for all measurement points.

It was observed from ZAF correction factors used by the microprobe

software that aluminium and yttrium have to be corrected more than 20%. The mass attenuation coefficients found in tables [Goldstein, 1992] of aluminum K-alpha in ytterbium (1464 cm^2/g) are close to the mass attenuation coefficients of aluminum K-alpha in yttrium (1501 cm^2/g), but the mass attenuation coefficient for yttrium L-alpha in ytterbium (3514 cm^2/g) is much higher than for yttrium L-alpha in yttrium (803 cm^2/g). Therefore, in the case of substitution of only several mol% of yttrium by ytterbium the calculated absorption correction for aluminum is only slightly changed while for yttrium higher corrections are needed. And because of the overestimation of aluminum and underestimation of yttrium it can be concluded that in the Yb:YAG matrix the mass attenuation coefficient for aluminum K-alpha in ytterbium is higher and for yttrium L-alpha in ytterbium lower than the mass attenuation coefficients found in tables. Normally, decreasing the accelerating voltage reduces the absorption correction, but because in this case wrong mass attenuation coefficients were used, also the calculation of absorption correction factors for a lower acceleration voltage does not lead to better results. This is shown for two measurements of 20 kV and 12 kV (table 2.3). Therefore, a Yb:YAG compound standard with a composition close to the measured sample has to be chosen to minimize the effect of the wrong absorption correction (table 2.3).

But such standards are not available commercially. The standards can be prepared by solid state sintering. 5g in total weight of Yb_2O_3, Al_2O_3 and Y_2O_3 powders of 4N purity were mixed and ground in ethanol by a ZrO_2 ball mill. The powders are then dried, pressed to pellets isostatic at 2 kbar and sintered at 1400 °C for 24 h in a platinum crucible. This was repeated two times with the reground pellet. The pellet was phase pure in terms of XRD measurements, but still of low density. Therefore, as a final step the pellet was sintered again at 1750 °C for 10 h on a low density Al_2O_3 ceramic sheet. The resulting pellet was dense, milky white and slightly translucent. A rim of 1 mm thickness of the pellet was cut off to avoid impurities which might have

measured composition in cation numbers with O = 12 $Al_2O_3/Y_2O_3/Yb_2O_3$	kV	standards
5.215 / 2.325 / 0.460	12	$YbPO_4$ and YAG compound
5.28 / 2.278 / 0.444	20	$YbPO_4$ and YAG compound
5.035 / 2.530 / 0.435	20	Yb:YAG compound

Table 2.3: EPMA measurements on the Yb:YAG standard sample with different kV and different standards

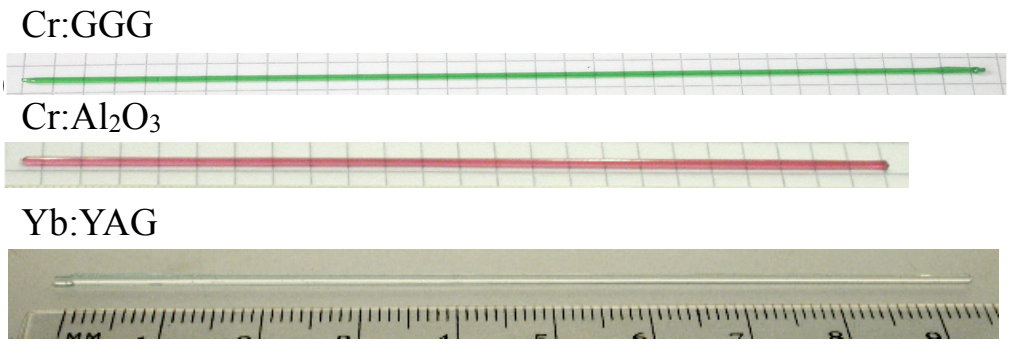

Figure 2.5: Photographs of the type 1 oxide fibers

come from contact with the Al_2O_3 ceramic sheet during the sintering process. From the resulting pellet a 2x2x2 mm^3 part of the middle was cut out for the use as standard. It was embedded and polished for electron microscopy purpose. The residual surrounding parts were used for X-ray powder diffraction (XRD) and ICP-AES measurements. For the ICP-AES measurement 300mg have been used and have been dissolved in 50 ml of H_3PO_4/HNO_3 acid. The resulting composition was 41.08±0.38 wt% Al_2O_3 / 45.35±0.37 wt% Y_2O_3 / 13.53±0.06 wt% Yb_2O_3. XRD showed phase purity. Grains greater than 5 μm and a low porosity were observed in the BSE image (figure 2.4). But one can see white particles which were identified as ZrO_2. This is an abrasion from the ball mill and does not alter the composition needed for standardization. Qualitative electron probe microanalysis measurements over several grains showed good homogeneity even some grains are looking brighter than others in the BSE image. The composition obtained by ICP-AES was then used for EPMA standardization. When the crystal fibers mentioned above are now measured using this ceramic compound standard the resulting cation ratios are found to be equal to ratios measured by ICP-AES. This can also be seen in table 2.3 when the measurements are done on the Yb:YAG standard sample.

2.1.3 Results

As it can be seen in figure 2.5 the type 1 fibers are constant in diameter and have a smooth surface. This is mainly controlled by the very stable melt film in growth of type 1, even in the case of the strongly wetting and creeping Cr:GGG melt. Type 2 fibers have a rough surface due to a less stable molten zone. The growth of Cr:GGG with type 2 is not possible because of the strong creeping melt in this case. Except in the case of $(Cr, Al)_2O_3$ all fibers

have a constant dopant concentration along the growth direction, which was confirmed by ICP-AES at 3 equidistant pieces of the fibers (table 2.4). The advantage of the ICP-AES method compared to EPMA is that one has the average composition over the full volume of the fiber pieces. With EPMA it is difficult to map the axial segregation profile because of the strong radial inhomogeneity and the limited size of the electron beam. This constant axial concentration suggests a fully diffusive transport regime in the crucible nozzle. Due to relative high pulling rate and absent convective mixing in the capillary the diffusion length $\beta = D/v$ (v: growth rate, D: diffusion rate) is lower than the inner length of the crucible capillary (3.5 mm). Therefore, if we use equation 1.6 and use the inner length of the capillary for δ we get an effective segregation coefficient of approximately 1. In the case of $(Cr, Al)_2O_3$ grown in a N_2 atmosphere, the Cr_2O_3 concentration decreases in growth direction (figure 2.6a and 2.6b) because of the evaporation of the volatile CrO. Therefore, after the growth run the alumina insulation ceramics became slightly red. When evacuating only to a vacuum of $3 \cdot 10^{-2}$ mbar by the rotary pump before filling with N_2, the dependence of the oxygen partial pressure on the radial and axial segregation can be seen for type 1 growth in figure 2.6a (compared to the phase diagrams in chapter 1.3.1). At the beginning of the fiber the oxygen partial pressure is equivalent to the prevacuum around 10^{-2} mbar, which is changed by the N_2 flow while growth more and more to the oxygen partial pressure equivalent to the 5N N_2 gas. This can be seen in figure 2.6a by the increasing radial segregation due to a decreasing k_0 (spreading Cr_2O_3 concentration curves of rim and core) and the raising axial decrease of the Cr_2O_3 concentration along the fiber due to raising evaporation of CrO. For the growth in CO_2 atmosphere, where we have higher oxygen partial pressure of around $p_{O_2} = 2 \cdot 10^{-2}$ bar and therefore less CrO in the melt, the axial concentration stays constant.

All type 1 fibers show strong radial segregations. This has been investigated first for the model materials with different equilibrium distribution coefficients and different oxygen partial pressures (figure 2.9). The fibers

Fiberpart	$(Ga, Al)_2O_3$	Yb:YAG	Yb:GGG	Cr:GGG
Begin	1,00	5,70	5,15	1,71
Middle	1,12	5,67	5,14	1,85
End	1,03	5,69	5,13	1,8
initial	1,5	5,65	5,0	1,75

Table 2.4: ICP-AES measurements of the axial dopant distribution in oxide fibers in mol%

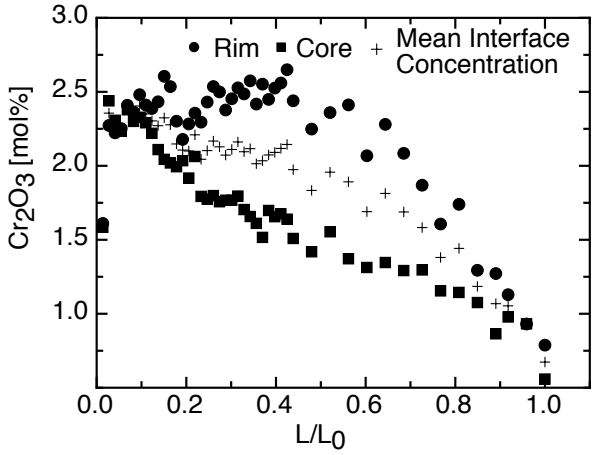

(a) Type 1 growth

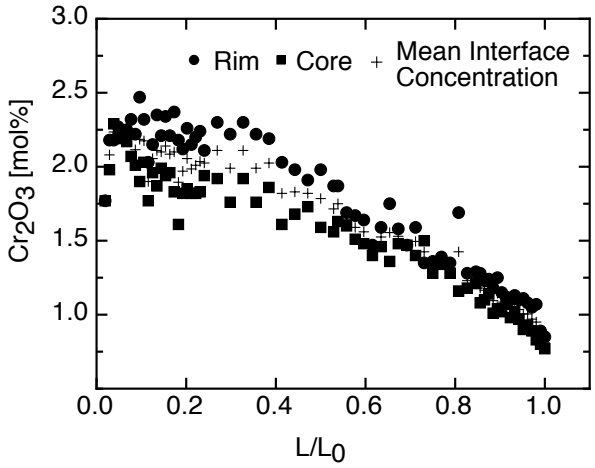

(b) Type 2 growth

Figure 2.6: Axial concentration profiles measured by EPMA for $(Cr, Al)_2O_3$

grown in the pure diffusive regime have a lower or higher dopant concentration in the rim region than the core region for $k_0 > 1$ or $k_0 < 1$, respectively. These results are reproduced for doped laser host materials (figure 2.10). This can be explained by the form of the growth interface. Figure 2.7 shows an axial cross-section BSE image of a quenched melt zone (by rapidly pulling down with 100 mm/min) of a Yb:YAG fiber grown with 0.5 mm/min pulling speed in N_2 atmosphere.

The contrast in BSE images is sensitive to the chemical composition. For comparison of BSE image contrast to the dopant concentration in figure 2.7

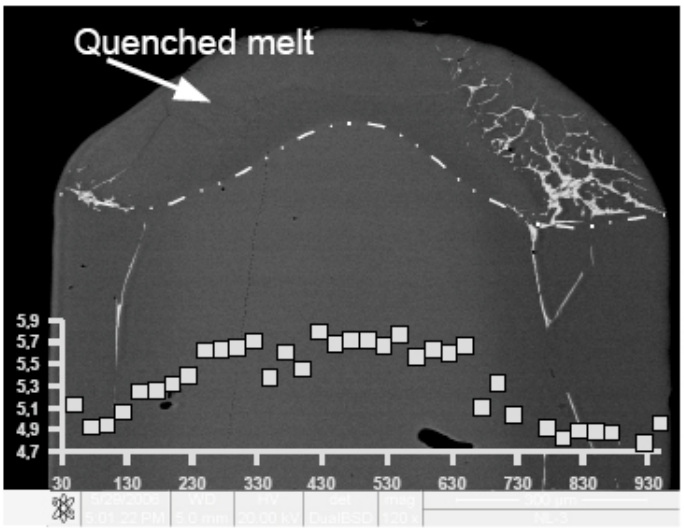

Figure 2.7: BSE image of a cross-section of an Yb:YAG fiber with quenched melt zone (0.5 mm/min pulling speed in N_2 atmosphere)

an EDS line-scan is overlapped. So one can clearly see the growth interface and the surrounding quenched melt (sketched by a dashed line). The growth interface is convex towards the melt. The bump in the interface is shaped by the diameter of the capillary outlet. During growth with very small melt meniscus the radial movement of the fiber was blocked by the capillary wall, which shows that in this case the bump reaches into the capillary. Therefore, in the fully diffusive range and for a small diffusion length, which is the case in micro-pulling-down growth of oxides, the radial distribution can be explained by the solution of the diffusion equation (equation 1.1 and 1.2) with a curved growth front as boundary condition by singular perturbation theory as done by [Coriell et al., 1981]. Two theoretical curves calculated by this theory for a cosine shaped interface, which could be used as a simplification, and $k_0 > 1$ and $k_0 < 1$ are shown in figure 2.8. The equilibrium distribution coefficient and the growth rate were taken similar to the experiment and the diffusion coefficient in the range as it is common for oxide melts. The solution is comparable to the experimental data. Note, the variable δ is chosen because used in [Coriell et al., 1981] and means the interface deflection or the amplitude of the cosine. Fitting was not possible because of a non-symmetric growth interface, but the theory depends on an interface with radial symmetry and we have a more complex geometry than a simple Bridgman setup used by [Coriell et al., 1981]. However, the results look very comparable.

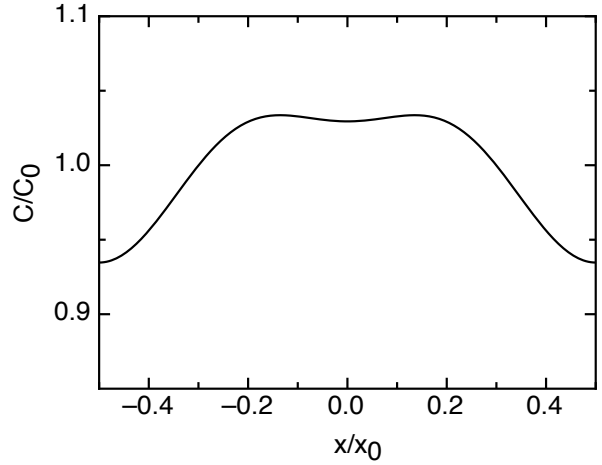

(a) $D = 1 \cdot 10^{-5}\, cm^{-2}$, $k_0 = 1.5$, $v = 0.5\,\mathrm{mm/min}$, δ=0.03

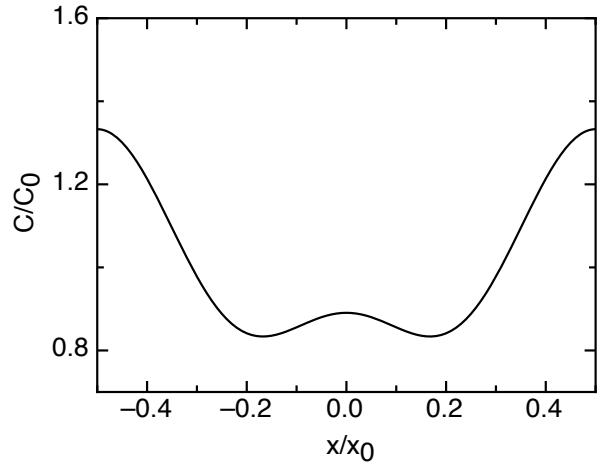

(b) $D = 5 \cdot 10^{-5}\, cm^{-2}$, $k_0 = 0.3$, $v = 0.5\,\mathrm{mm/min}$, δ=0.004

Figure 2.8: Radial concentration profiles calculated with Coriell's theory

For the growth of Yb:YAG also the influence of the pulling speed was investigated by growing fibers with 0.3, 0.1 and 0.01 mm/min. One can see clearly that the slower the pulling speed the flatter the segregation profile gets (figure 2.10c-2.10e). Therefore, for inducing a core/rim dopant profile a higher pulling speed is necessary. In contrast, for a homogeneous fiber an as low as possible pulling speed is necessary.

The effect of the oxygen partial pressure can be seen for $(Cr, Al)_2O_3$ and Yb:YAG. The $(Cr, Al)_2O_3$ grown under a N_2 atmosphere shows a concen-

tration profile corresponding to $k_0 < 1$ and the $(Cr, Al)_2O_3$ grown in a CO_2 atmosphere shows a concentration profile corresponding to $k_0 > 1$. This is comparable to the calculated phase diagrams for $p_{O_2} = 10^{-6}$ bar (N_2) and $p_{O_2} = 10^{-2}$ bar (CO_2) in figure 1.15 and 1.11, respectively. This can also be seen for Yb:YAG. When using forming gas, more of the Yb^{3+} is reduced to Yb^{2+} and therefore the equilibrium distribution coefficient is lowered similar as described for $(Cr, Al)_2O_3$ in chapter 1.3.1. Figure 2.10f shows therefore a much flatter concentration profile than in the N_2 grown sample (figure 2.10c).

The type 2 fibers show the same axial segregation behaviour like the type 1 fibers but the radial concentration profile is flatter than in the type 1 fibers and more irregular (figure 2.11). During growth it is observed that the interface is slightly spherical and radial movement of the fiber during growth is easily possible. So we have less interface deflection and a stronger Marangoni convection at the free melt/gas interface of the considerable meniscus and therefore a flatter radial dopant distribution. The irregularities in the type 2 $(Ga, Al)_2O_3$ (figure 2.11b) are maybe due to strong Marangoni swirls caused by the melt/gas interface, which enrich the melt with dopant close to the growth interface or due to a beginning constitutional supercooling.

2.1.4 Mechanical stress due to segregation

The Yb:YAG fibers show internal cracks and strain when grown at pulling speeds greater than 0.01 mm/min. The strain can be seen in polished cross-sections under crossed polarizers (figure 2.14) for different growth orientations. It is remarkably, that for pulling speeds greater than 0.1 mm/min, the strain pattern is observed to be congruent with possible facets for the chosen growth direction. For the <100> growth direction the strain pattern has a 4-fold symmetry (figure 2.14d) and a 6-fold symmetry for the <111> growth direction (2.14e), which corresponds to the (110) and (211) crystallographic planes, respectively.

The crystal is growing normally with a microscopically rough growth interface, which follows the melt isothermal surface (or the dopant dependent solidification temperature surface) with small supercooling, which is necessary for growth. When the solidification-temperature surface coincides some crystallographic plane, a facet can be formed. The faceted region will have a flat growth interface with a different growth mechanism in which a higher supercooling is needed for growth. The degree of supercooling is dependent on the growth speed [Wilke and Bohm, 1988]. For intermediate supercooling the growth interface mostly first gets roughened by forming steps of crystallographic planes rather than immediately forming facets.

In the case when facets or roughening occurs, the growth front is not

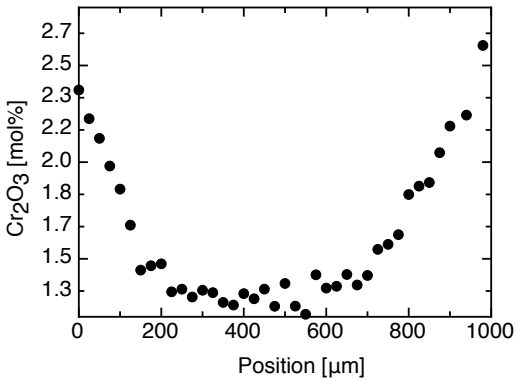

(a) $(Cr, Al)_2O_3$ in N_2 atmosphere

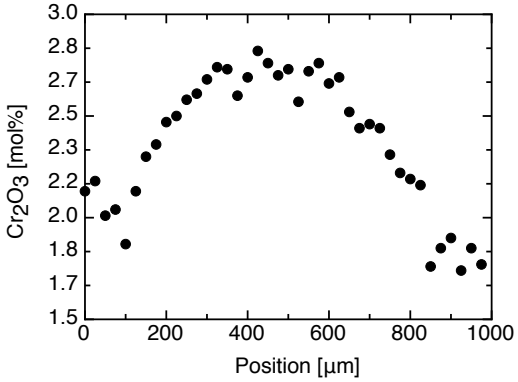

(b) $(Cr, Al)_2O_3$ in CO_2 atmosphere

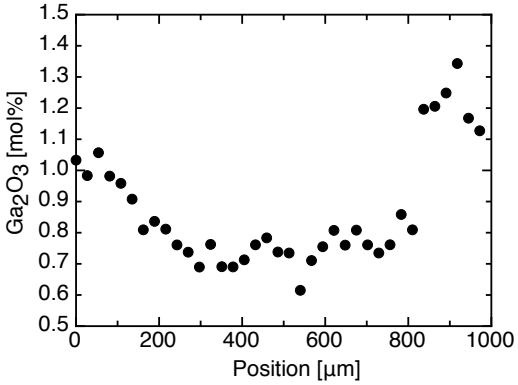

(c) $(Ga, Al)_2O_3$

Figure 2.9: Radial concentration profiles measured by EPMA for type 1 grown model materials

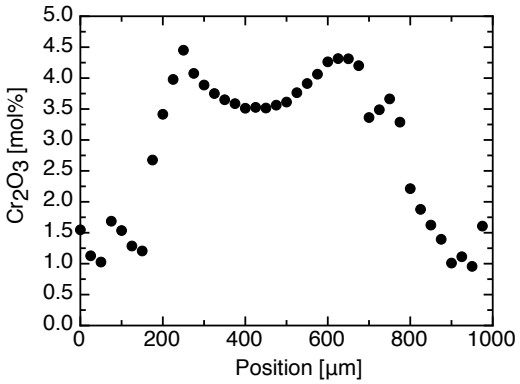

(a) Cr:GGG

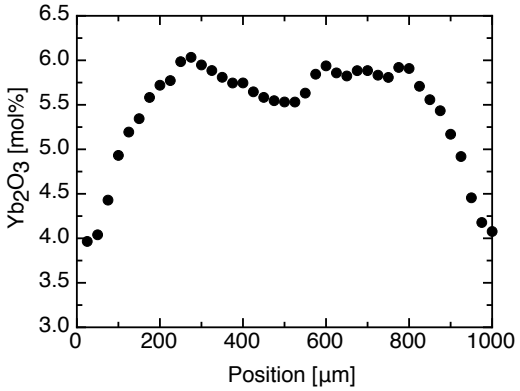

(b) Yb:GGG

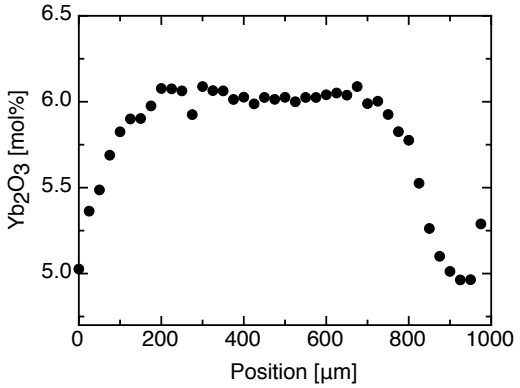

(c) Yb:YAG with 0.3 mm/min pulling speed in N_2 atmosphere

Figure 2.10: (continued)

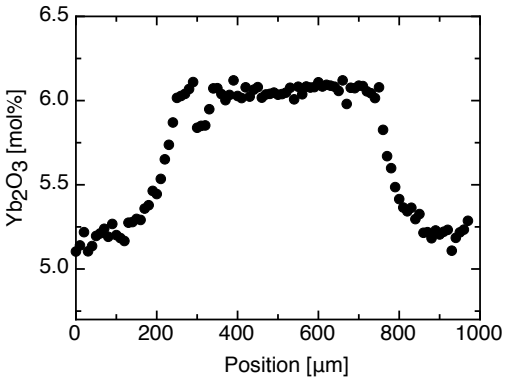

(d) Yb:YAG with 0.1 mm/min pulling speed in N_2 atmosphere

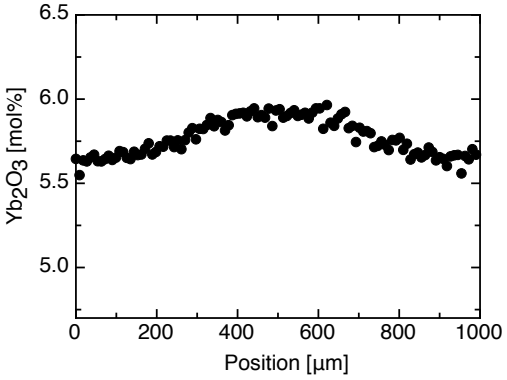

(e) Yb:YAG with 0.01 mm/min pulling speed in N_2 atmosphere

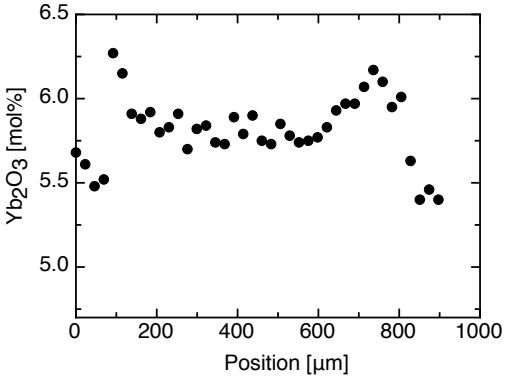

(f) Yb:YAG with 0.3 mm/min pulling speed in forming gas

Figure 2.10: (continued)

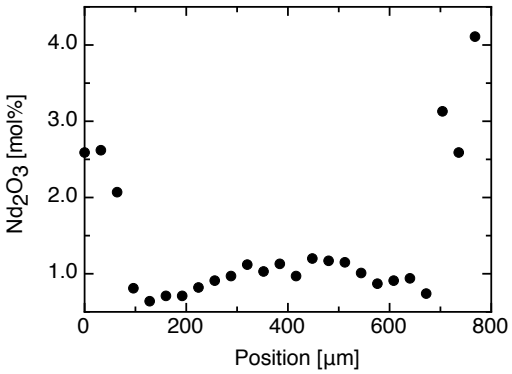

(g) Nd:YAG

Figure 2.10: Radial concentration profiles measured by EPMA for type 1 grown fibers

radial symmetric anymore but is taken as an assumption for the calculation of the dopant distribution by an analytical solution 2.1.3 or by the numerical calculations in chapter 3. Therefore the dopant distribution, which strongly depends on the form of the growth front, is not radial symmetric but dependent on the crystallographic planes of the faceted regions. This can be seen in the BSE image of the cross-sections by means of bright straight lines or bright planes of chemical contrast, which correlate to the step edges or the facet planes, respectively (figure 2.14c and figure 2.14b, respectively).

The effect of faceting or roughening can also be seen by comparing the cross-sections under crossed polarizers for the growth with 0.1 mm/min and 0.3 mm/min pulling speed. For 0.1 mm/min pulling speed no indication for faceting or step-like roughening can be found in the BSE image (figure 2.14h) and the corresponding polarized micrograph shows homogeneous radial symmetric strain along the trailing edge of the radial Yb_2O_3 concentration profile in the crystal (figure 2.14g). At higher pulling speed of 0.3 mm/min, and therefore a higher supercooling, the interface gets step-like roughened, as can be seen in the BSE image (figure 2.14b). The corresponding polarized micrograph shows strain dependent to the step-like roughened regions (figure 2.14a). So it can be concluded that the segregation is not radial symmetric in this case.

For slow pulling speed of 0.01 mm/min there is nearly no segregation and nearly no faceting (figure 2.10e and 2.14j) and the strain pattern also nearly vanishes (figure 2.14i). The undoped YAG fiber grown under the same conditions and a pulling speed of 0.3 mm/min (grown from a Czochralski-crystal piece as starting material to exclude impurity effects) also shows no

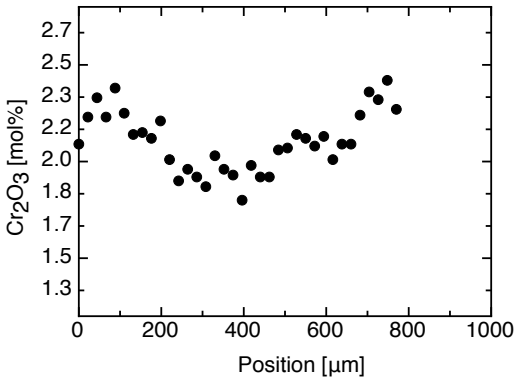

(a) $(Cr, Al)_2O_3$

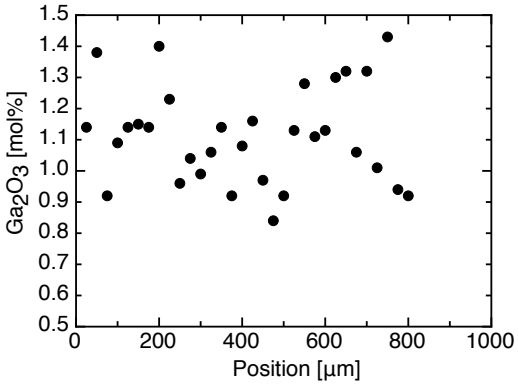

(b) $(Ga, Al)_2O_3$

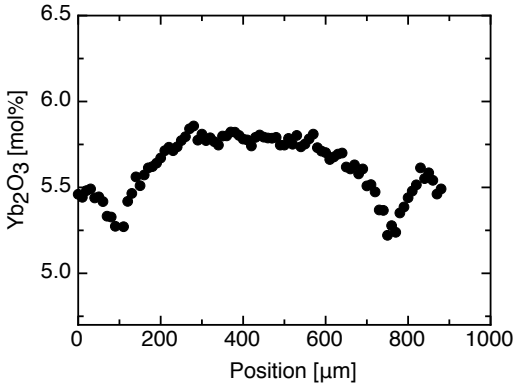

(c) Yb:YAG with 0.3 mm/min pulling speed

Figure 2.11: (continued)

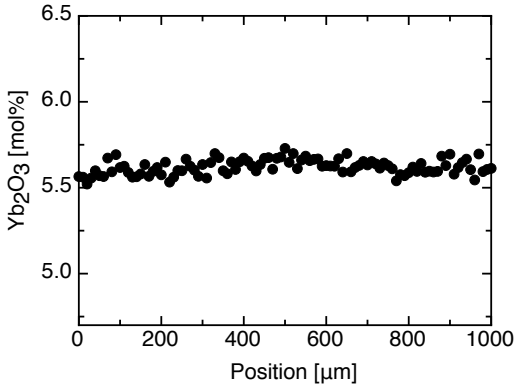

(d) Yb:YAG with 0.01 mm/min pulling speed

Figure 2.11: Radial concentration profiles measured by EPMA of type 2 grown fibers

strain effects. This suggests, that if there is no dopant or impurity which can be incorporated, no strain is produced by possible facets or roughening itself (figure 2.14f). Therefore, one can conclude that the strain in Yb:YAG fibers is a fact of changing Yb_2O_3 content in the crystal due to the segregation phenomena.

But the cracking could not be explained by the local stress induced by segregation, because the stress induced by the change of the lattice constant due to the Yb_2O_3 concentration profile in the YAG matrix is less than the breaking stress. This can be seen in the numerical calculations in chapter 3.5.4. The stress calculations show a stress concentration at the position of the crack, but the maximum calculated stress of 33 MPa is much lower than the breaking stress of 200 MPa ([RP-Photonics, 2008]). It is noteworthy that the cracks are also congruent with the facet orientation. This is can be explained by constitutional supercooling.

The faceted or step-like region with some degree of supercooling joins a region of the rough interface without supercooling at the inflexion point of the slope of the bend interface near the rim of the fiber. It is likely that a ditch in the interface will be formed at this point. In this ditch supercooled melt can be frozen ([Wilke and Bohm, 1988]). This can be seen in the WDS mappings in figure 2.13b. Inside the cracks a higher Yb_2O_3 and Y_2O_3 concentration was found similar to the region of the quenched melt. This ingrown melt acts as a stress concentrator ([Eakins et al., 2004]) and will give enough stress to the ditch apex that a crack will form.

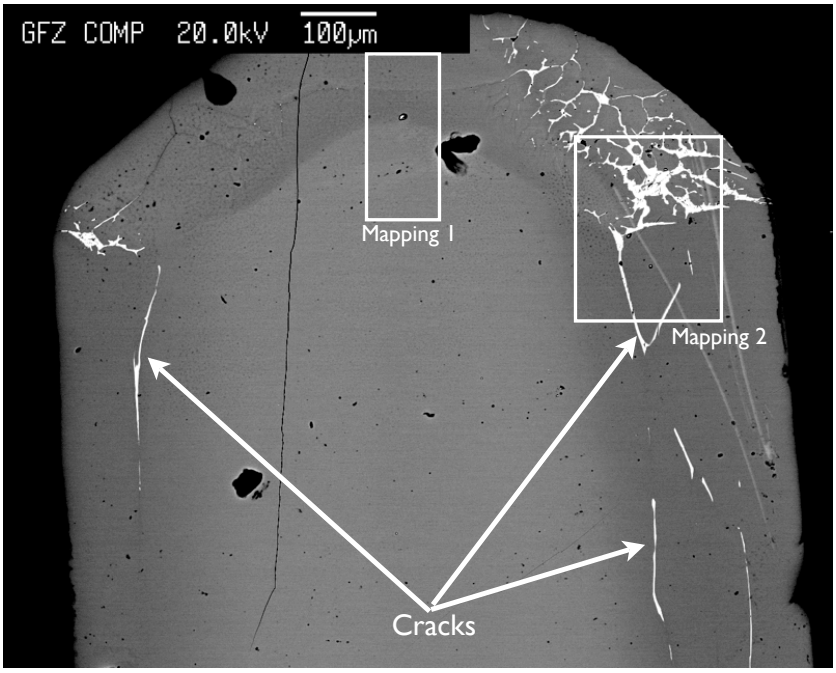

Figure 2.12: BSE image of the axial cross-section of the Yb:YAG fiber with the quenched melt zone. Two regions are marked where WDS concentration mappings were performed. Also cracks are shown by arrows.

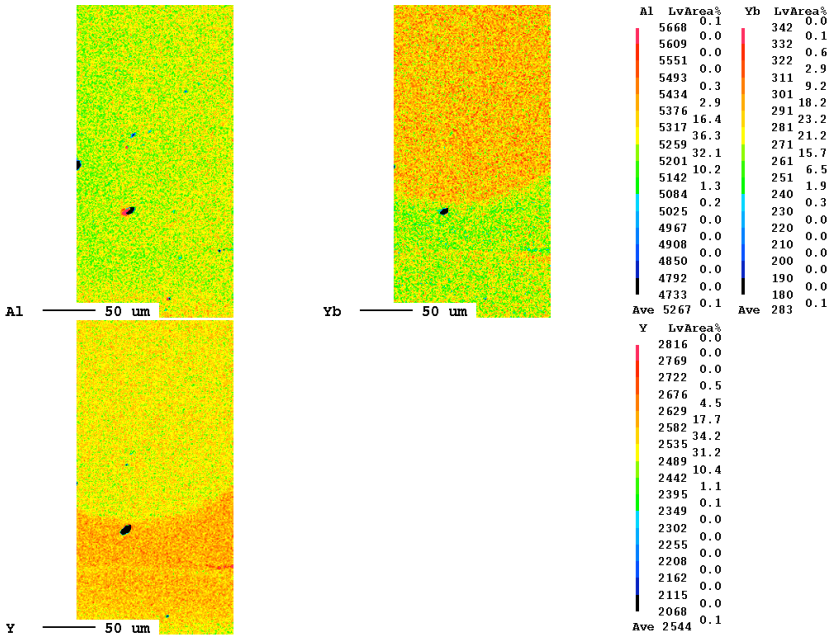

(a) Region 1

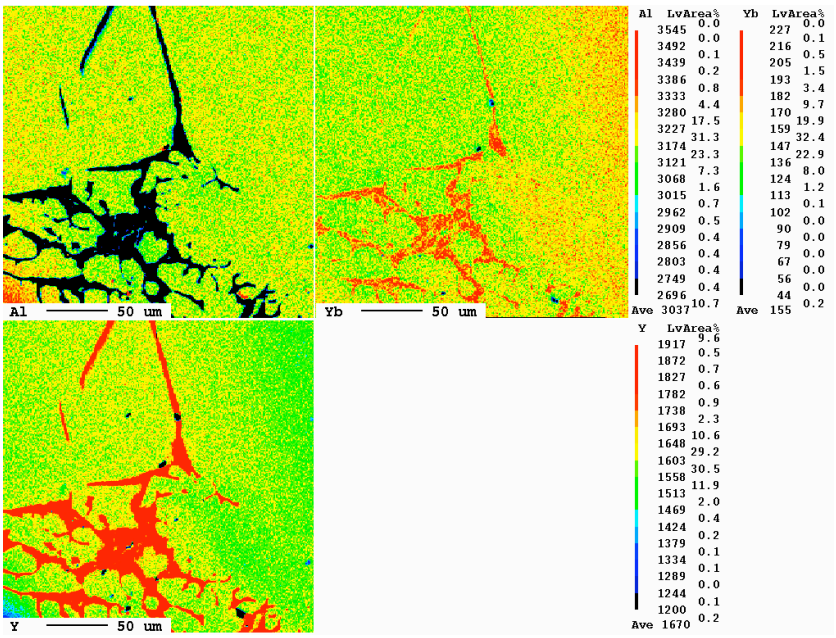

(b) Region 2

Figure 2.13: WDS mappings of the growth front
WDS mappings of the regions marked in figure 2.12. The images of the mappings are upside down compared to the marked area in the BSE image

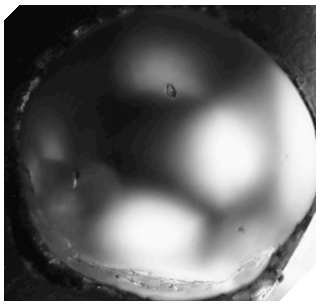

(a) "Unoriented" type 1 fiber grown with 0.3 mm/min under crossed polarizers

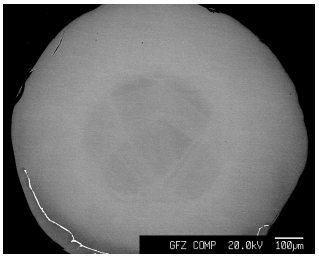

(b) BSE image of the fiber shown in figure 2.14a (faceted parts are bright)

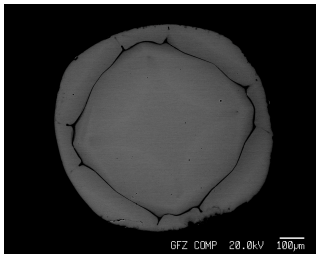

(c) BSE image of a <100> oriented type 2 fiber grown with 0.3 mm/min

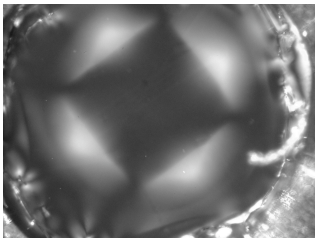

(d) A <100> oriented type 1 fiber grown with 0.3 mm/min under crossed polarizers

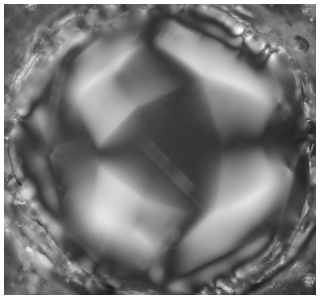

(e) A <111> oriented type 1 fiber grown with 0.3 mm/min under crossed polarizers

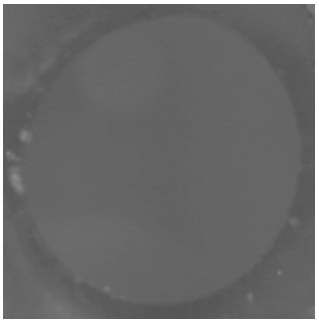

(f) A <100> oriented type 1 fiber of undoped YAG grown with 0.3 mm/min under crossed polarizers

Figure 2.14: (continued)

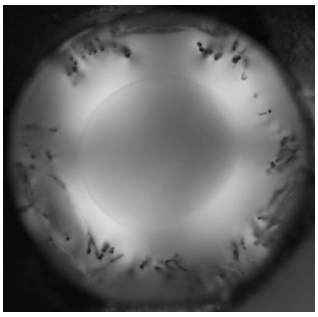

(g) A <100> oriented type 1 fiber grown with 0.1 mm/min under crossed polarizers

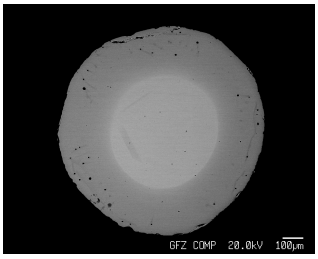

(h) BSE image of a <100> oriented type 1 fiber grown with 0.1 mm/min

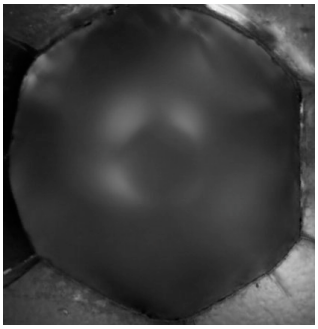

(i) A <100> oriented type 1 fiber grown with 0.01 mm/min under crossed polarizers

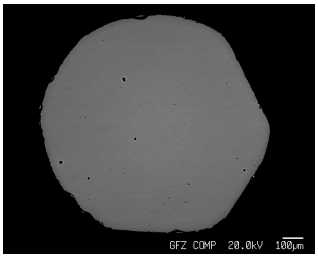

(j) BSE image of a <100> oriented type 1 fiber grown with 0.01 mm/min

Figure 2.14: Cross-sections of Yb:YAG / YAG fibers under crossed polarizers (stress is concentrated at the bright parts) and corresponding BSE images

2.2 Growth of $LiYF_4$

In this section more attention is paid to the axial segregation. Due to the nearly absent axial segregation in micro-pulling-down-growth and therefore missing self-cleaning effect by segregation, this growth method demands for very pure initial substances and clean atmospheres. As described in chapter 1.3.3, the $LiYF_4$ is very sensitive to water and oxygen traces and is sometimes discussed as incongruently melting, and therefore an ideal system to investigate the question of purity and composition.

2.2.1 Fiber crystal growth

$LiYF_4$ fibers were grown using a 5 ml platinum crucible on an active platinum after heater placed on a quartz pedestal and surrounded by a quartz tube. About 200 mg of $LiYF_4$ optical transparent single-crystal pieces from prior Czochralski experiments were used as a starting material and placed in the platinum crucible. The chamber was evacuated in two ways: for 24 h to $3 \cdot 10^{-3}$ mbar by a rotary pump or to $2 \cdot 10^{-6}$ mbar by a turbo molecular pump, respectively. Then the chamber was filled either with 5N Argon, 5% CF_4 in Argon or with 99.995% CF_4 gas and a flow of 150 ml/min was adjusted. The seed, 1 mm in diameter was cut from a $LiYF_4$ Czochralski crystal. After seeding the fibers were pulled with 0.5 mm/min. The rf power was manually controlled to keep the diameter of the fibers at about 1 mm.

Photographs of the fibers that were obtained under different growth conditions are shown in figure 2.15. It can be clearly seen in figure 2.15a that residual oxygen or water in the chamber, resulting from insufficient evacuation prior to filling with gas, leads to completely white and brittle fibers. In this case, even a pure CF_4 atmosphere does not produce enough HF to suppress oxidation of the melt, as the reaction

$$CF_4 \rightleftarrows CF_3 + F \tag{2.2}$$

supplies the reactive fluorine insufficiently at the low melting point $T_f = 828\,^{\circ}C$ of $LiYF_4$ ($k^{(2.2)}_{828,1\,bar} = 8.4 \cdot 10^{-18}\,bar^{-1}$, calculation performed with FactSage [GTT, 2007]). EDS spectra of the white parts show a significant oxygen peak (figure 2.16c). Therefore, this white parts can be attributed to oxyfluorides, as oxygen is known to solve in YF_3 to $\approx 2\%$ [Sobolev et al., 1976]. The exact chemical composition could not be determined by EDS because Li is not detectable by EDS. But it seems, that it is rather a slightly oxidized YF_3 than the stoichiometric YOF. Since the lattice constants will not change significantly by a slight oxidation of YF_3 the XRD spectra were

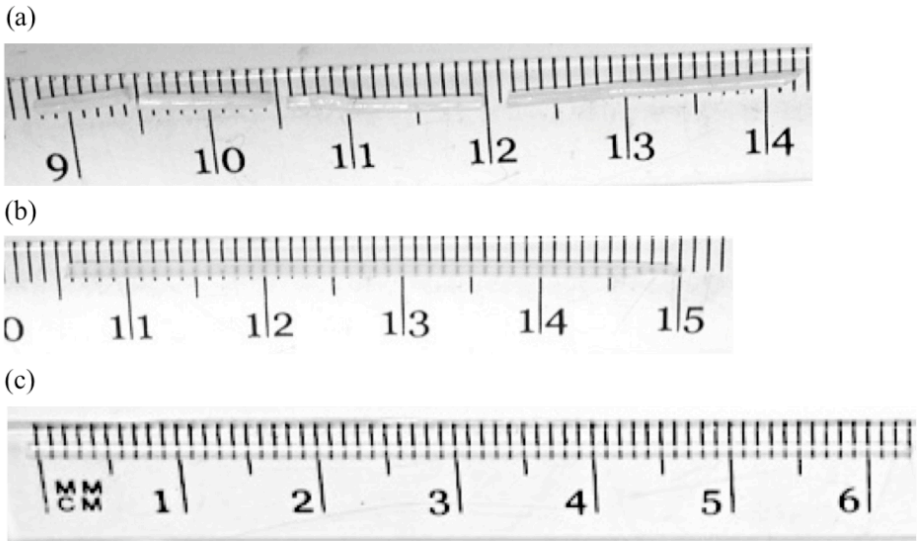

Figure 2.15: Photographs of fibers grown in different atmospheres: (a) $3 \cdot 10^{-3}$ mbar / CF_4 (b) $2 \cdot 10^{-6}$ mbar / 5% CF_4 in Argon (c) $2 \cdot 10^{-6}$ mbar/CF_4

misinterpreted by assigning the additional peaks (arrow in figure 2.17a) to YF_3 and therefore concluding erroneously that the white precipitates were due to incongruent melting [Malankiewicz et al., 2005, Santo et al., 2004]. There is nearly no axial segregation for the micro-pulling-down growth, in opposite to Bridgman or Czochralski growth, where one gets, because of an effective segregation coefficient $k < 1$, a first part of the crystal full of white precipitates followed by a clear part of the crystal. This cleaning effect of the melt during growth is not present for micro-pulling-down growth of fiber crystals. This is due to the dominant diffusional regime in the relatively high inner length of the capillary (2−4 mm), which leads to an effective segregation coefficient of $k \approx 1$ [Burton et al., 1953]. Therefore, the oxyfluoride inclusions are distributed over the whole fiber.

If the chamber is evacuated prior growth to a high vacuum of $2 \cdot 10^{-6}$ mbar for 24 h to remove water and oxygen, and subsequently 5N Argon gas or a even gas mixture of 5% CF_4 in argon is used for growth, residual oxygen or water impurities in the source material lead to small oxyfluoride micro-crystallites segregating to the rim of the grown fiber. The fiber is mostly transparent but has a slightly white and rough surface due to these micro-crystallites (figure 2.15b). EDS measurements of the starting material showed that a small amount of oxygen or water is present in the crystal pieces (figure 2.16a).

When evacuating the chamber to a vacuum of $2 \cdot 10^{-6}$ mbar for 24 h and

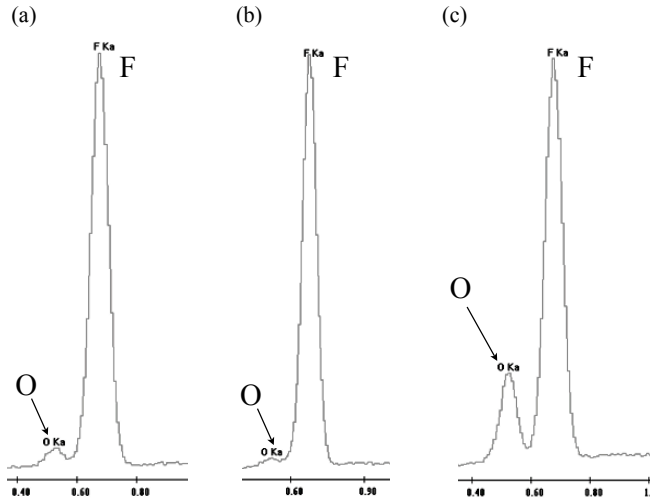

Figure 2.16: Cut-out of the oxygen and fluorine peak of the EDS spectra of (a) starting material (b)transparent region (c) milky-white needle precipitates

using pure 99.995% CF_4 gas for growth the grown fiber is completely transparent (figure 2.15c) and free from secondary phases (figure 2.17b). A chemical analysis by ICP-AES gave a composition of 50.5 mol% YF_3 and 49.5 mol% LiF, which shows that the composition of the fiber is very close to the expected stoichiometric $LiYF_4$ composition. It was also observed, that the melt is less viscous and less wetting than in the other experiments with oxofluorides still present. Therefore, in this case it was possible to completely crystallize the whole melt without leaving any melt droplets inside the crucible.

The CF_4 is in chemical equilibrium with reactive F and CF_x ($x = 3, 2, 1$) at the melting temperature for our compound (equation 2.2). The fluorine can react with water traces to HF, or can even fluorinate the slightly oxidized melt, if the concentration of impurities is not too large. Therefore, pure CF_4 is needed to supply sufficiently reactive fluorine via this equilibrium reaction at the relatively low melting temperature of $LiYF_4$. Diluting the CF_4 in Argon does not allow to reach a comparable equilibrium reaction.

2.2.2 Differential scanning calorimetry

Differential scanning calorimetry (DSC) was performed with a NETZSCH STA 449C "Jupiter" with DSC/TG sample carrier (thermocouples type S) in argon (99.999% purity) flowing at a rate of 20 ml/min. Before filling with argon, the apparatus was evacuated to approximately $6 \cdot 10^{-4}$ mbar. Pieces broken from transparent $LiYF_4$ fibers (sample masses = 5 − 14 mg) were

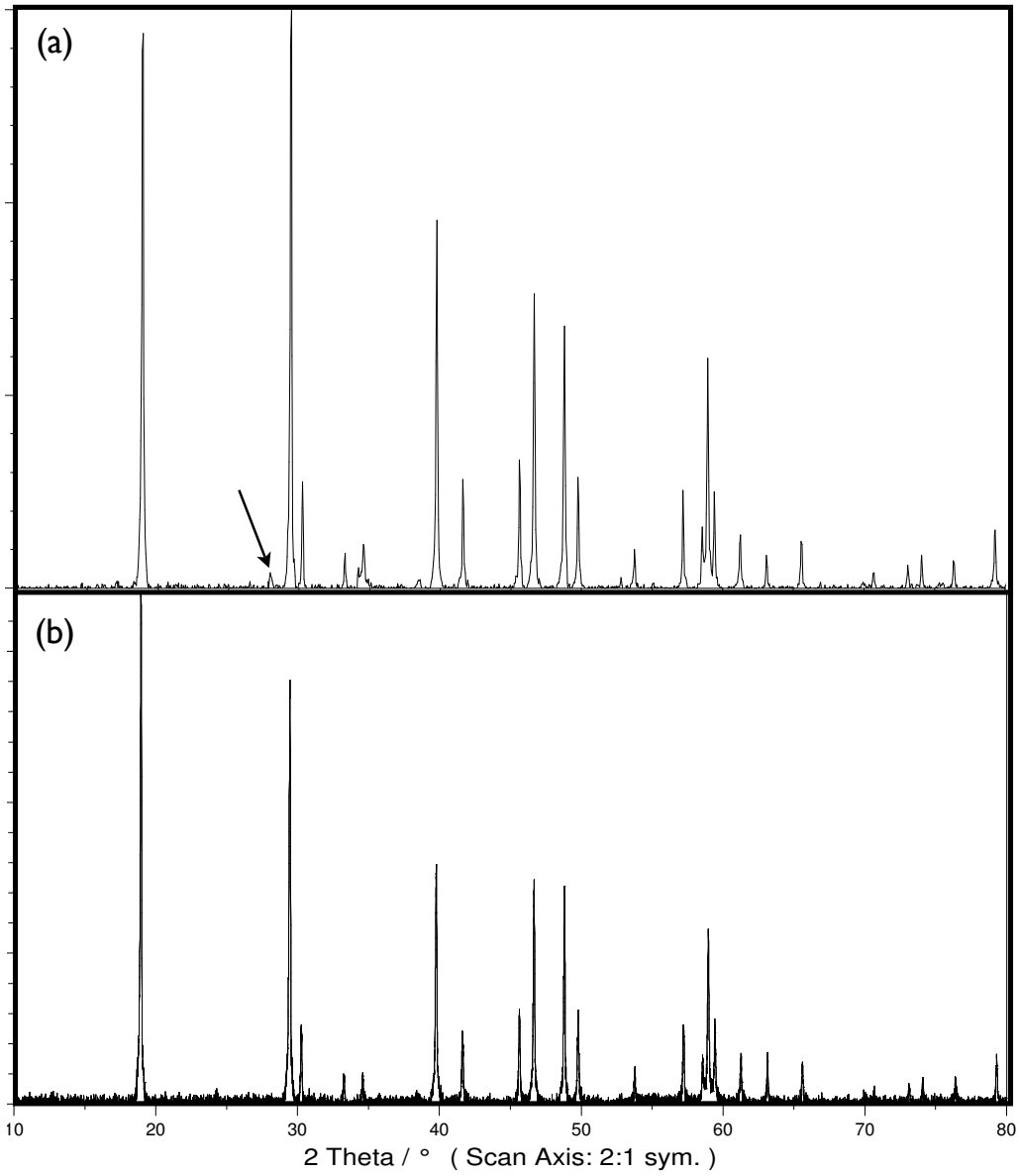

Figure 2.17: XRD spectra of a (a) fiber containing oxyfluorides (b) transparent fiber. The arrow marks the peak often assigned wrongly to YF_3

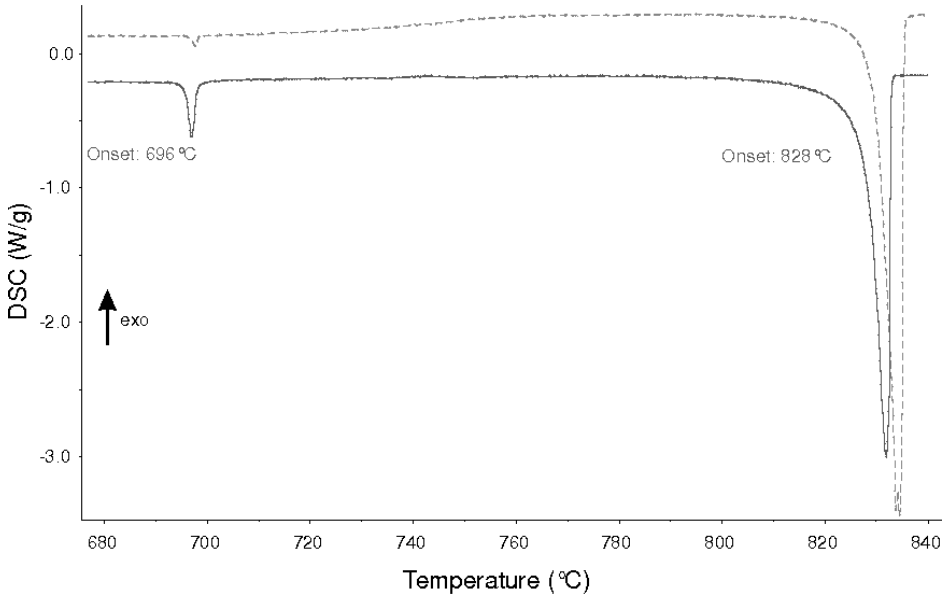

Figure 2.18: First (dashed line) and second heating of an optically clear $LiYF_4$ fiber. Sample mass: 5.62 mg. Heating rate 2 K/min.

placed in Pt/Rh crucibles with lid. To obtain good thermal resolution, low heating rates of 1 or 2 K/min, respectively, were used up to $T_{max} = 840 - 850$ °C. Immediately after the first heating a second heating was performed under identical conditions without intermediate opening of the apparatus. The mass loss due to evaporation was $\approx 1\%$.

The first and the second DSC heating curve of a $LiYF_4$ fiber are shown in figure 2.18. It is surprising, that already in the first run a minor endothermal effect can be observed at 696 °C, which is almost identical to the eutectic temperature in the LiF–YF_3 binary system, which is reported at 694 °C [Thoma et al., 1961] (figure 1.23). The observation of this effect can be explained by the partial reaction of the YF_3 component with oxygen or water tracer impurities within the argon rinsing gas that was used during the measurement to yttrium oxofluorides. Therefore, the remaining composition shifts to the LiF side in the phase diagram and an eutectic composition melts. The area of the eutectic peak was measured to be 2.5 J/g, which is minor compared to the main melting peak at 828 °C (445 J/g). After melting the YF_3 component gets further oxidized and precipitates as yttrium oxofluoride (the solidified melt is slightly white), which has a higher melting point than the temperature range used in this study. So the melt composition shifts more to the LiF side in the phase diagram. Therefore, during the second heating a significant eutectic peak is found. This again illustrates the high sensitivity

of YF_3 to oxidation as found while growth in non CF_4 atmosphere. But no indication of a high-temperature shoulder of the main melting peak could be observed. Such shoulder would have been an indication for incongruent melting of $LiYF_4$ postulated by some authors [Thoma et al., 1961, Santo et al., 2004].

Chapter 3

Numerical simulation of the micro-pulling-down method

In this chapter, the micro-pulling-down growth for oxides is physically described. Because of the complex geometry and the need of nonlinear coupled differential equations a numerical method is needed. The theory in chapter 2 is a qualitative model and gives only a phenomenological description of the physics which is responsible for the segregation effect. But for a more reliable description of the solid / liquid interface curvature and hence of the diffusion, the analytical methods fail and numerical calculations become necessary. For the calculations described below, the finite element method was chosen and performed with the COMSOL FEMLAB 3.3a software package [Com, 2007].

3.1 Model geometry

The model is described by an radial symmetric simplified setup taking a part of the crystal, the melt zone and only the capillary part of the crucible into account. The melt reservoir is assumed as a container with a much larger volume compared to the capillary inner volume containing mixed melt of constant concentration and constant temperature. Therefore, the melt reservoir is neglected in the calculations. The symmetry line is at $r = 0$. The equations are written in cylindrical coordinates r, ϕ, z, but because of radial symmetry the equations are independent of the azimuthal coordinate ϕ. So the equations are only dependent on the r and z components. The radial symmetry is not really fulfilled in the real experiment, but was chosen as a simplification to reduce the calculation time. This is the reason, why the fits to the experimental values (see below) are sometimes not perfect and are calculated only for one half of the measured values over the diameter. Of

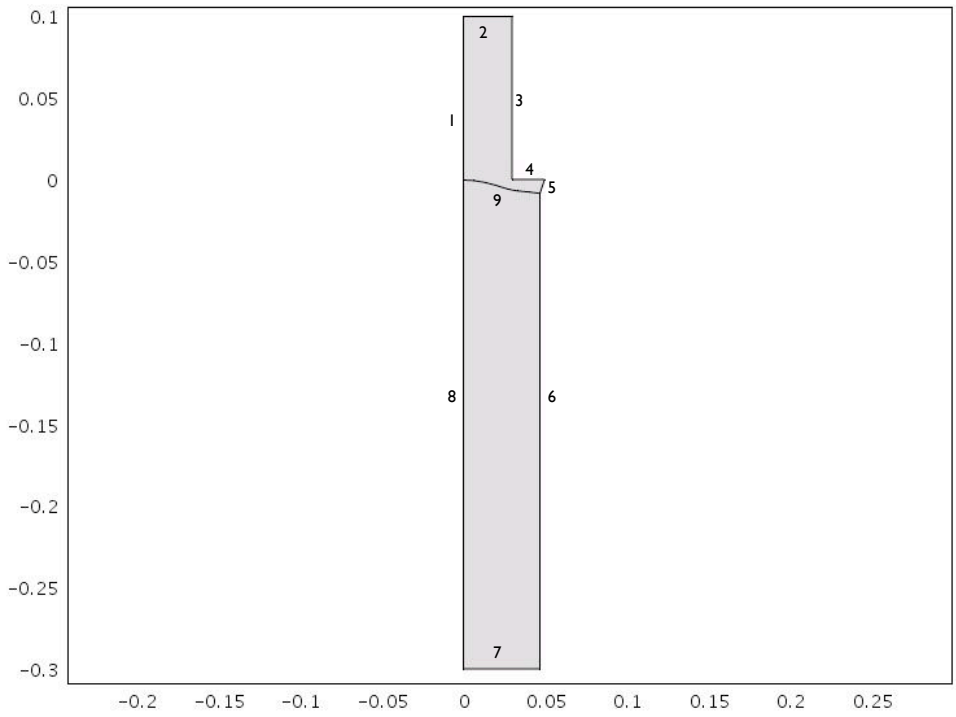

Figure 3.1: Geometry of the radial symmetric model. The symmetry line at r=0 (boundaries 1,8), boundaries 3 and 4 are the capillary inner walls, boundary 5 is the melt/gas interface, boundary 2 is the capillary inlet connected to the melt reservoir and boundary 9 is the growth front. Boundary 6 is the crystal surface and boundary 7 the crystal end. The boundary conditions are associated with these boundary numbers according to table 3.1

course, the other half could also be calculated by a slightly changed geometry and/or other thermal conditions. So the aim of this calculations is mainly to explain the segregation effect and the validity of the equations and obtained values for the experiments done in this thesis.

3.2 Equations

In this section the necessary equations are described. The boundary conditions are associated with the boundary numbers in figure 3.1 according to table 3.1

3.2.1 Mass transport: Navier-Stokes equations

It is assumed that the melt is a non-compressible fluid which can be described by the Navier-Stokes equations. Equation 3.1 describes the momentum balance and equation 3.2 is the continuity of the incompressible fluid.

$$\vec{\nabla} \cdot \left[-\rho \vec{I} + \eta \left(\vec{\nabla} \cdot \vec{u} + (\vec{\nabla} \cdot \vec{u})^T \right) \right] + \rho(\vec{u} \cdot \vec{\nabla})\vec{u} = \vec{F} \tag{3.1}$$

$$\vec{\nabla} \cdot \vec{u} = 0 \tag{3.2}$$

where $\vec{u}$, η, $\vec{I}$ and p are the velocity vector, dynamic viscosity and the pressure. The volume force $\vec{F}$ is chosen to account for the concentration and thermal induced density differences in the melt (Buoyancy convection) by the following equation

$$\vec{F} = \vec{g}\beta_T \rho(T - T_t) + \vec{g}\beta_c \rho(c - c_0) \tag{3.3}$$

with $\vec{g}$ as the gravitational acceleration and β_T, β_c as the temperature and concentration depended volume expansion coefficient, respectively. The system is described similar to a tubular flow. The melt flows from the top of the capillary, which corresponds to the inlet, to the growth front, which corresponds to the outlet.

Boundary conditions

N-1 Marangoni condition at the free surface:

$$\vec{K} = \tau \vec{n} = \eta \left(\vec{\nabla} \cdot \vec{u} + (\vec{\nabla} \cdot \vec{u})^T \right) \vec{n} \tag{3.4}$$

$$\vec{t} \cdot \vec{K} = \vec{t} \cdot (\gamma \vec{\nabla} T) \tag{3.5}$$

$$\vec{n} \cdot \vec{u} = 0 \tag{3.6}$$

N-2 No-slip

$$u = 0,\ v = 0 \tag{3.7}$$

N-3 Constant pressure / Inflow

$$\vec{n} \cdot \vec{K} = 0,\ p = p_0,\ \vec{t} \cdot \vec{u} = 0 \tag{3.8}$$

N-4 Outflow

$$u = 0,\ v = -v_g \tag{3.9}$$

The growth front fluid velocity is set to the pulling velocity $v = -v_g$ (N-4). The capillary inlet is a neutral condition, which keeps the normal viscous force $\vec{n} \cdot \vec{K} = 0$, at constant pressure p. Therefore, the fluid velocity is adjusted just by the geometry and the outflow velocity at the growth front (N-3).

On the melt/gas interface, the Marangoni condition is chosen. The Marangoni condition describes the balance between the tangential viscous force $\vec{t} \cdot \vec{K}$ and the tangential temperature gradient. The velocity in the normal direction is of course $\vec{u} = 0$, since there is no outflow (N-1).

The crucible walls have a no-slip condition, which means the velocity is $v = 0$ (N-2).

3.2.2 Heat transport: Thermal conduction and convection equation with internal radiation transport

The heat transport through crystal and melt is described by the thermal convection and diffusion equation (equation 3.10) coupled with the equation for internal heat radiation transport (equation 3.11). The convection part of the equation is coupled to the Navier-Stokes equations by the velocity $\vec{u}$. The internal radiation equation is calculated by a differential approximation [Korpela et al., 1996], where the equation of transfer is described by its first two moment equations.

$$\vec{\nabla} \cdot \left(-k_i \vec{\nabla} T + \frac{1}{3a_{Ri}} \vec{\nabla} J_i \right) + \rho_i C_{pi} \vec{u} \cdot \vec{\nabla} T = 0 \quad (i = m, c) \tag{3.10}$$

$$\vec{\nabla}^2 J_i + 3a_{Ri} a_{Pi} (4\pi^2 \sigma_s T^4 - J_i) = 0 \quad (i = m, c) \tag{3.11}$$

where a_{R_i}, a_{P_i}, C_{pi}, T, $\vec{n}$, J_i, σ_s are the mean Rosseland, mean Planck absorption coefficient, heat capacity, temperature, radiation flux and the Stefan-Boltzmann constant.

The mean Rosseland and Planck absorption coefficients are calculated with the following equations

$$\begin{aligned} a_P &= \frac{\pi}{n^2 \sigma_s T^4} \sum_{0}^{4000\,nm} a_\nu B_\nu \Delta\nu \\ \frac{1}{a_R} &= \frac{\pi}{4n^2 \sigma_s T^3} \sum_{0}^{4000\,nm} \frac{1}{a_\nu} \frac{dB_\nu}{dT} \Delta\nu \\ B_\nu &= \frac{2h^3 \nu^3}{c^2 e^{\frac{h\nu}{kT}} - 1} \end{aligned} \tag{3.12}$$

where a_ν, n, h, σ_s and k are the spectral absorption coefficient, refractive index, Planck constant, Stefan-Boltzmann constant and the Boltzmann constant, respectively. The Rosseland and Planck mean absorption coefficients have been calculated by dividing the experimental observed absorption spectra of Yb:YAG [Denker et al., 2007], Nd:YAG [Galazka et al., 2003] and $(Cr, Al)_2O_3$ [Velickov, 2006] into $\Delta\nu = 50\,nm$ bands and summing with equation 3.13.

Boundary conditions

T-1 Thermal radiation

$$\vec{n}\left(-k_i\vec{\nabla}T + \frac{1}{3a_{Ri}}\vec{\nabla}J_i + \rho_i C_{pi}\vec{u}T\right) = 0 \quad (i = m, c) \tag{3.13}$$

$$-\vec{n}\cdot\vec{\nabla}J_i = \frac{3a_{Ri}}{2}\left(\frac{1-\rho}{1+\rho}\right)(J_i - 4n^2\sigma_s T_a^4) \quad (i = m, c) \tag{3.14}$$

T-2 Temperature

$$T = T_0 \tag{3.15}$$

$$-\vec{n}\cdot\vec{\nabla}J_i = \frac{3a_{Ri}\epsilon_w}{2(2-\epsilon_w)}(J_i - 4n^2\sigma_s T_0^4) \quad (i = m, c) \tag{3.16}$$

T-3 Flux discontinuity: Latent heat of fusion

$$\vec{n}\cdot\left(-k_m\vec{\nabla}T + \frac{1}{3a_{Rm}}\vec{\nabla}J_m + \rho_m C_{pm}\vec{u}T\right)\Big|_m \times$$
$$-\vec{n}\cdot\left(-k_c\vec{\nabla}T + \frac{1}{3a_{Rc}}\vec{\nabla}J_c + \rho_c C_{pc}\vec{u}T\right)\Big|_c = \rho_c L_f v_g \tag{3.17}$$

where ρ and ϵ_w are the reflectivity and emissivity, respectively. As a simplification the crucible walls, the capillary inlet and the crystal end are set to a temperature condition (T-2). A constant temperature at the top which decreases linearly by a $\Delta T_{capillary} = 5K$ along the capillary wall was assumed. Also after 3 mm the crystal end was set to a constant temperature of a measured value (section 2.1.1). This is a valid simplification, because after some trial calculations, one can see that the isothermal lines stay horizontal.

The melt and the crystal wall have a heat radiation condition (T-1). For simplification, the effective ambient temperature T_a, which the crystal or melt sees for radiative heat transport is set constant over this 3mm and is about 150K lower than the melting temperature. This is about the value which a free standing thermocouple gives at this position. At the growth front, heat flux discontinuity exists because of the latent heat of fusion, which is released by the growing crystal (T-3).

3.2.3 Mass transport: Diffusion and thermodiffusion equation

The mass transport is described by two convection-diffusion equations (equation 3.18). For taking the effect of the oxygen partial pressure into account, the variable c_1 is the concentration of the 3+ dopant metal-oxide (Me^{3+}) and the variable c_2 is the concentration of the 2+ oxide. The two convection-diffusion equations are then coupled by the constraint in equation 3.19, which describes the concentration c_2 in terms of c_1 multiplied by a factor $F(c_1, c_2)$. This factor is the oxygen partial pressure dependent fraction of the 3+/2+ dopant oxide.

Both convection-diffusion equations also include a term for thermodiffusion. This is taken into account, because we have high temperature gradients in the system and therefore the diffusion along a temperature gradient can not be neglected.

$$\vec{\nabla} \cdot (-D_i \vec{\nabla} c_i - c_i(1 - c_i) D_i^T \vec{\nabla} T) + \vec{u} \cdot \vec{\nabla} c_i = 0 \quad (i = 1, 2) \tag{3.18}$$

$$c_2 = F(c_1, c_2) c_1 \tag{3.19}$$

where D_i and D_i^T are the diffusion coefficient and the thermodiffusion coefficient, respectively for the species 1 and 2.

Boundary conditions

D-1 Insulation

$$- D\vec{\nabla} c_i - c_i(1 - c_i) D^T \vec{\nabla} T + c_i \vec{u} = 0 \tag{3.20}$$

D-2 concentration

$$c_i = C_0 \tag{3.21}$$

D-3 Flux: Growth front

$$- D\vec{\nabla} c_i - c_i(1 - c_i) D^T \vec{\nabla} T + c_i \vec{u} = k_0 c_i \vec{u} \tag{3.22}$$

where k_0 is the equilibrium distribution coefficient. The growth front is set to a flux condition which is describes the incorporation of dopant into the crystal dependent of the equilibrium distribution coefficient. This means, the flux leaving or entering the growth front is $k_0 c_i \vec{u}$. The k_0 for c_2 is set to 0.001 to simulate that the suboxide is nearly not incorporated into the crystal. The inlet is set to a constant concentration, which is equal to the dopant concentration in the melt reservoir.

3.2.4 Stress-strain equations

The stresses and strains in axial symmetry are calculated by the global displacement (u, v, w) in the r and z directions. The displacements v in ϕ direction and the $r\phi$ and ϕz components of the shear strain γ and shear stresses τ are zero. Loads are also independent of ϕ. The strain-displacement relationship for small displacements is then

$$\epsilon_r = \frac{\partial u}{\partial r} \tag{3.23}$$

$$\epsilon_\phi = \frac{u}{r} \tag{3.24}$$

$$\epsilon_z = \frac{\partial w}{\partial z} \tag{3.25}$$

$$\gamma_{rz} = \frac{\partial u}{\partial z} + \frac{\partial w}{\partial r} \tag{3.26}$$

where ϵ is the strain. The strain consists of the elastic contribution $\vec{\epsilon}$, the thermal contribution $\vec{\epsilon_{th}}$ and the concentration contribution $\vec{\epsilon_{conc}}$. The relationship between the stress σ and the strain is

$$\vec{\sigma} = E(\vec{\epsilon} + \vec{\epsilon}_{th} + \vec{\epsilon}_{conc}) \tag{3.27}$$

where E is the young‘s modulus. The perpendicular stresses are correlated by the Poisson‘s ratio ν as

$$\epsilon_\perp = \nu_P \epsilon_\parallel \tag{3.28}$$

The thermal stress is

$$\epsilon_{th} = \alpha_T (T - T_0) \tag{3.29}$$

where α_T is the thermal expansion coefficient. In the same way the concentration dependent strain is calculated

$$\epsilon_{conc} = \alpha_c (c_c - c_0) \tag{3.30}$$

where α_c is the concentration dependent expansion coefficient. This coefficient is the relative change of lattice constant per mol% of dopant concentration. The concentration in the crystal is calculated by taking the melt concentration c_1 at the growth front and multiplying by k_0 as $c_c = k_0 c_1$ and applying to the whole fiber.

Finally the equilibrium equations are then solved

$$\frac{\partial \sigma_r}{\partial r} + \frac{\partial \tau_{rz}}{\partial z} + \frac{\sigma_r - \sigma_\phi}{r} + K_r = 0 \tag{3.31}$$

$$\frac{\partial \sigma_z}{\partial z} + \frac{\partial \tau_{rz}}{\partial r} + \frac{\tau_{rz}}{r} + K_z = 0 \tag{3.32}$$

$$\tag{3.33}$$

Boundary	Diff. c	Diff. c_2	N. S.	Thermal
1	r=0	r=0	r=0	r=0
2	D-2	D-1	N-3	T-2
3	D-1	D-1	N-2	T-2
4	D-1	D-1	N-2	T-2
5	D-1	D-1	N-1	T-1
6	N.A.	N.A.	N.A.	T-3
7	N.A.	N.A.	N.A.	T-2
8	N.A.	N.A.	N.A.	r=0
9	D-3	D-3	N-4	T-3

Table 3.1: Boundary conditions for the diffusion equations, the Navier-Stokes equation (N.S.) and the thermal convection, conduction and internal radiation equations associated with boundary numbers shown in the model geometry figure 3.1

where $\vec{\sigma}$ is the stress and $\vec{K}$ is the external load. The result is plotted as the Tresca-stress, an equivalent stress, which is the maximum shear stress independent to the direction. This equivalent stress is used to compare the breaking strength to the maximum shear stress at each point.

3.3 Growth front and melt/gas interface

The growth front was calculated with the help of a FEMLAB script. A calculation was performed on a flat interface, then the isothermal line of the melting point was extracted. This isothermal line was fitted by a polynomial and included in the new geometry. Then the calculation was repeated. After 3 to 4 iterations the growth front converges to the calculated isothermal line.

The melt/gas interface was not calculated numerically. From the height of the melting isothermal line, the radius of the crystal was calculated from the Young‘s equation [Rudolph and Fukuda, 1999] for a stable meniscus at every iteration step mentioned above. Then a Bézier curve (a parametrically modeled curve), similar to a meniscus observed in experiments, was drawn for the melt/gas interface. The Bézier curve fulfills the growth angle at the join to the growth interface.

	$(Cr, Al)_2O_3$	YAG
$k_c[erg/(s \cdot cm \cdot K)]$	$0.058 \cdot 10^7$ [Kopetsch, 1990]	$0.08 \cdot 10^7$ [Xiao and Derby, 1994]
$k_m[erg/(s \cdot cm \cdot K)]$	$0.1 \cdot 10^7$ [Langlois, 1980]	$0.04 \cdot 10^7$ [Xiao and Derby, 1994]
$\rho_c[g/cm^3]$	3.97 [Kopetsch, 1990]	4.3 [Xiao and Derby, 1994]
$\rho_m[g/cm^3]$	3.05 [Langlois, 1980]	3.6 [Xiao and Derby, 1994]
$C_{p_c}[erg/(g \cdot K)]$	$1.43 \cdot 10^7$ [Kopetsch, 1990]	$0.8 \cdot 10^7$ [Xiao and Derby, 1994]
$C_{p_m}[erg/(g \cdot K)]$	$1.26 \cdot 10^7$ [Langlois, 1980]	$0.8 \cdot 10^7$ [Xiao and Derby, 1994]
$\eta[g/(cm \cdot s)]$	0.27 [Langlois, 1980]	0.46 [Xiao and Derby, 1994]
$L_f[erg/g]$	$1067 \cdot 10^7$ [Kopetsch, 1990]	$455 \cdot 10^7$ [Xiao and Derby, 1994]
$T_0[K]$	2323	2253
$\Delta T_{capilary}[K]$	5	5
$\Delta T_{crystal}[K/cm]$	400	210
$T_{radiation}[K]$	T_0-150	T_0-150
α_{R_c}	3.7	Yb: 0.44 Nd: 0.177
α_{P_c}	0.033	Yb: 0.041 Nd: 0.059
α_{R_m}	$80\alpha_{R_c}$	$80\alpha_{R_c}$
α_{P_m}	$80\alpha_{P_c}$	$80\alpha_{P_c}$
n	1.72 [Wikipedia, 2008]	1.82 [Banerjee and Muralidhar, 2006]
ϵ_m	0.33 [Tavakoli, 2006]	0.33 [Xiao and Derby, 1994]
ϵ_c	0.3 [Tavakoli, 2006]	0.3 [Xiao and Derby, 1994]
ρ_c	0.8 [Tavakoli, 2006]	0.8 [Tavakoli, 2006]
$\gamma[dyn \cdot K/cm]$	$-3.5 \cdot 10^{-2}$ [Tavakoli, 2006]	$-3.5 \cdot 10^{-2}$ [Banerjee and Muralidhar, 2006]
k_2	0.001	0.001

Table 3.2: (continued)

	$(Cr, Al)_2O_3$	YAG
$E[barye]$	–	$3 \cdot 10^{12}$ [Yagi et al., 2007] [RP-Photonics, 2008]
ν	–	0.25 [Yagi et al., 2007] [RP-Photonics, 2008]
$\alpha_T[1/K]$	–	$8 \cdot 10^{-6}$ [Aggarwal et al., 2005] [RP-Photonics, 2008]
$\alpha_c[1/mol\%(Yb_2O_3)]$	–	$-1.2 \cdot 10^{-4}$

Table 3.2: Physical constants used in modeling for $(Cr, Al)_2O_3$ and YAG in cgs units. Values taken from literature are referenced. Other values are calculated (see text) or taken from experimental data

3.4 Mesh

The mesh was generated by the auto-mesher of the FEMLAB software package. For the calculations a triangular mesh was chosen. The mesh consisted of 3421 elements with a mean element quality of 0.75 on a scale from 0 (bad) to 1 (optimal) quality. The quality of a mesh element depends on the angles between the edges. Non-ideal angles can lead to convergence problems. The mesh was refined close to the walls and growth front in the melt domain (figure 3.2).

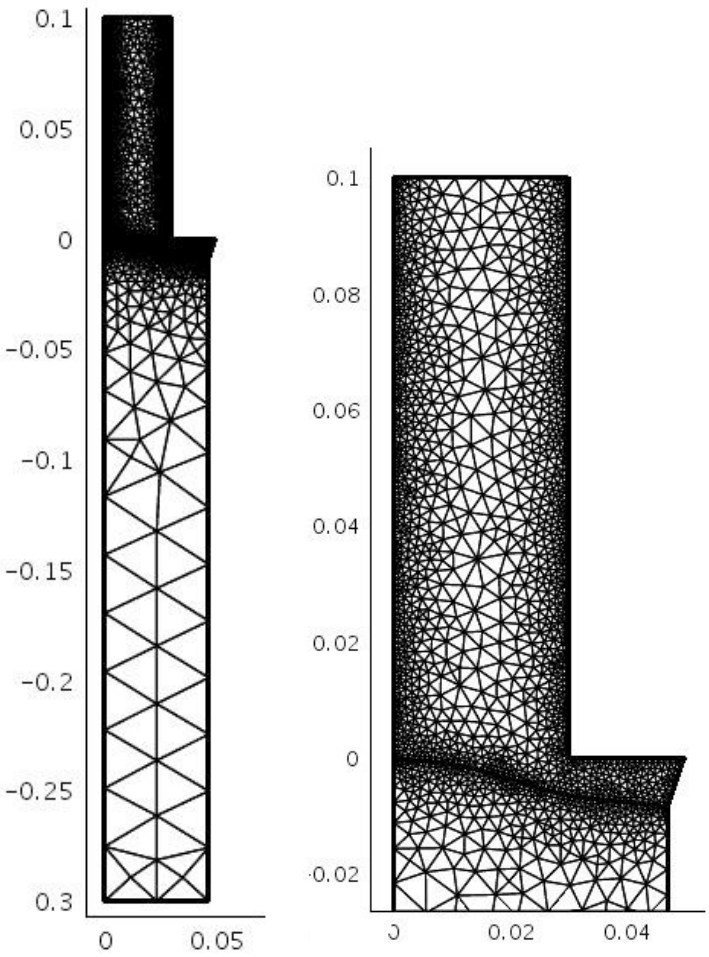

(a) Whole model (b) Close-up of subdomain 1

Figure 3.2: Mesh used for the calculations

3.5 Results

3.5.1 Temperature distribution

In figure 3.5, i.e. it is shown, that the calculated growth front is bent convex towards the melt. This is the case for all calculations and is comparable to the experimental observed growth front (figure 2.12). The temperature distribution is strongly dependent on the Rosseland and Planck mean absorption coefficients. In calculations without taking internal radiation into account, the temperature gradient results in unreal gradients of more than 1000 K/cm. But including internal radiation the calculated temperature distribution (figure 3.3) becomes comparable to the experimental obtained distribution. This gives an explanation why [Yoon et al., 1994] has found thermal gradients of 1500 K/cm for $LiNbO_3$, because in this case the internal radiation does not play an important role.

3.5.2 Melt flow

The calculated melt flow is shown in figure 3.4. The melt is slowed down close to the capillary wall. For type 1 growth the melt velocity increases drastically at the interior corner of the capillary outlet. This velocity increase is stronger, the stronger the growth interface is bend into the capillary region (figure 3.4c). Also the direction of the melt flow changes there. This is maybe a reason, in the case of growth of Yb:YAG, for the incorporation of Y_2O_3 and Yb_2O_3 rich melt in the cracks shown in figure 2.13b. The melt has its maximum velocity change, because of the strong change in flow direction, at the position where the facetted region has its transition to a rough region. This transition will have a ditch because the faceted region has some degree of supercooling and therefore a lowered growth front in contrast to the less supercooled rough interface. This ditch will also affect the melt flow and therefore the incorporation of melt from higher boundary layer positions with higher Y_2O_3 and Yb_2O_3 concentrations into this supercooled ditch region is supported (similar to constitutional supercooling). Cracking at this bump further increases this effect (see chapter 2.1.4).

The Marangoni convection creates a very small swirl at the melt/gas interface for type 1 growth and does not influence the concentration profile much. But for type 2 growth the Marangoni swirl becomes strong and extended (figure 3.4b). This also flattens the concentration profile in the rim region (figure 3.8).

Because of the lack of thermal and concentration volume expansion coefficients calculations have been performed with these coefficients as a param-

Compound, atmosphere	$F(c_1, c_2)$	D_1, D_2 $[cm^2/s]$	$\alpha_T[1/K]$	k_0
$(Cr, Al)_2O_3$, N_2	1.2*	$2 \cdot 10^{-5}$, $2 \cdot 10^{-5}$	0.015	1.5
$(Cr, Al)_2O_3$, CO_2	0.15 *	$2 \cdot 10^{-5}$, $2 \cdot 10^{-5}$	0.015	1.5
$(Ga, Al)_2O_3$, CO_2	0.01	$7.5 \cdot 10^{-5}$, $2 \cdot 10^{-5}$	0.015	0.35
Yb:YAG, N_2	0.34	$5 \cdot 10^{-6}$, $2.5 \cdot 10^{-6}$	0.045	1.5
Yb:YAG, N_2/forming gas	0.54	$5 \cdot 10^{-6}$, $2.5 \cdot 10^{-6}$	0.045	1.5

Table 3.3: Ratio of Yb^{3+}/Yb^{2+} $F(c_1, c_2)$ (* calculated with FactSage), diffusion constants D_1, D_2, thermodiffusion factor $\alpha_T = D^T/D$ and equilibrium distribution coefficient of the 3+ dopant oxide k_0 used for the calculations of the different compounds

eter. But for values in the range of $\beta = 10^{-4}$ no remarkable change in the fluid flow and the diffusion profile could be observed. Therefore, for micro-pulling-down growth the buoyancy convection can be neglected because of a temperature gradient in direction of the gravitational force and relatively high melt flow because of high pulling speeds.

3.5.3 Concentration profiles

Concentration profiles have been calculated for different equilibrium distribution coefficients of the 3+ dopant oxide, k_0, and different oxygen partial pressures (described by $F(c_1, c_2)$). The used $F(c_1, c_2)$, diffusion constants, thermodiffusion factors and k_0 are listed in table 3.3. The first calculations have been done for the model materials $(Cr, Al)_2O_3$ and $(Ga, Al)_2O_3$. The Cr_2O_3 (pure 3+) has a $k_0 \approx 1.5$ in Al_2O_3. But at a low oxygen partial pressure, as for the growth in N_2 atmosphere and therefore a higher amount of CrO in the melt the segregation profile (figure 3.5) is comparable to materials with $k_0 < 1$, like $(Ga, Al)_2O_3$ or Nd:YAG (figure 3.7 and 3.14), where the rim has a higher dopant concentration than the core. At a higher oxygen partial pressure, and therefore a low $F(c_1, c_2)$, the segregation profile stays similar to a material with $k_0 > 1$, where the rim has a lower dopant concentration than the core. This can be seen in the case of growth in CO_2 atmosphere with a higher oxygen partial pressure (figure 3.6). The $F(c_1, c_2)$ used for the calculations are taken from prior phase diagram calculations with the FactSage software for a N_2 and a CO_2 atmosphere. Therefore, the numerical calculations in combination with thermodynamical calculations fit well to the experimental data.

For type 2 growth the radial dopant distribution is flattened because of a flatter interface. In addition, the dopant distribution is further equalized

in the rim region by the Marangoni swirl (figure 3.8).

For the Yb:YAG we have a system with $k_0 \approx 1.5$ for the Yb_2O_3 (pure 3+) in YAG. For this system many pulling speeds have been investigated. For the calculations all parameters have been chosen as the same and only the pulling speed was variable. The calculations fit well to the experimental data. It is worth to mention that the experiments for lower pulling speeds have been performed after the predictions of the numerical calculations. As one can see, the lower the pulling speed is set the flatter the radial dopant distribution gets. But even with 0.01 mm/min, there is a little bump at the core in the radial dopant distribution for type 1 growth. But for type 2 growth at this slow pulling speed one gets a flat and homogeneous radial dopant distribution.

To calculate the ternary effect, a third convection-diffusion equation with an additional variable c_3 for the Y_2O_3 was introduced in the same way as equation 3.18. The result of the calculation for Y_2O_3 in type 1 growth can be seen in figure 3.10. For this component the same parameters have been used as for Yb_2O_3 but the growth front has been set to a Dirichlet condition

$$c_3 = 0.375 - c_1 \tag{3.34}$$

which accounts for a partial substitution of Y_2O_3 (c_3) by Yb_2O_3 (c_1) in the grown crystal and a total content of 37.5 mol% (stoichiometry of 3 in the chemical formula). This boundary has to be set as a "non-ideal" weak constraint in FEMLAB to have only the coupling of the c_1 to the c_3 equation and not vice versa (for "ideal" weak constraints a minimum for c_1 and c_3 in both coupled equations is calculated by variational principle). Also the thermodiffusion for Y_2O_3 was neglected, because the calculated thermodiffusion coefficients in chapter 4 are only valid for diluted components. But one can see the higher Y_2O_3 concentration in the outer region close to the melt/gas interface (figure 3.10). This is in good accordance to the WDS mapping in figure 2.13b.

Thermodiffusion

The effect of thermodiffusion can be seen for Yb:YAG. The Yb_2O_3 is enriched in the melt at the capillary wall close to the inner corner of the capillary (figure 3.9). This is enhanced in the case when there is a higher Yb^{2+} content, as for the growth in forming gas atmosphere (figure 3.13). This enrichment is in the region where also the melt flow speed is getting higher and cracking of the crystal is observed. Therefore, an enrichment of Yb_2O_3 can also be found in the cracks, as mentioned in the last section. It should be mentioned, that for high thermodiffusion factors the calculated dopant distribution of $k_0 > 1$

can be similar to a distribution of $k_0 < 1$. Therefore, the thermodiffusion factors cannot be chosen as a simple parameter and have to be estimated experimentally or in the case of this work by thermodynamical calculations shown in chapter 4 and table 4.1.

3.5.4 Mechanical stress

The calculated Tresca-stress for a type 1 Yb:YAG fiber is shown in figure 3.17. For the concentration dependent expansion coefficient, α_c, the correlation between the lattice constant and the Yb_2O_3 content was used (taken from [Swirkowicz et al., 2005]). One can see a higher stress in the trailing edge of the Yb_2O_3 profile. But the maximal calculated stress of 33 MPa ($3.3 \cdot 10^8$ *barye*) is much lower than the breaking stress of 200 MPa [RP-Photonics, 2008]. Calculations only for the thermal induced stresses show maximum Tresca-stress values of only 3 MPa. Therefore, internal cracking could not be induced by the dopant distribution nor the temperature gradients. For simplicity, the calculations have been performed in axial symmetry, which does of course not take faceting into account, but the strain patterns shown in chapter 2.1.4 can be concluded as an effect of the dopant distribution.

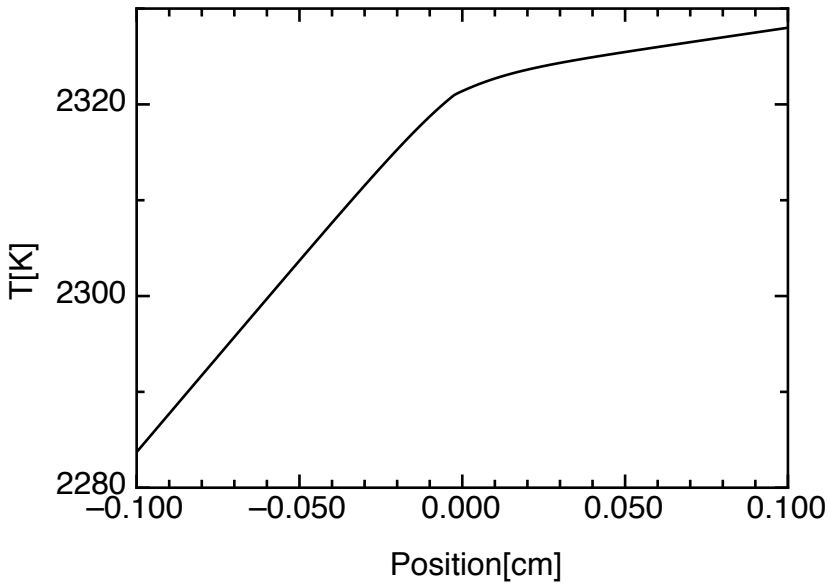

(a) $(Cr, Al)_2O_3$

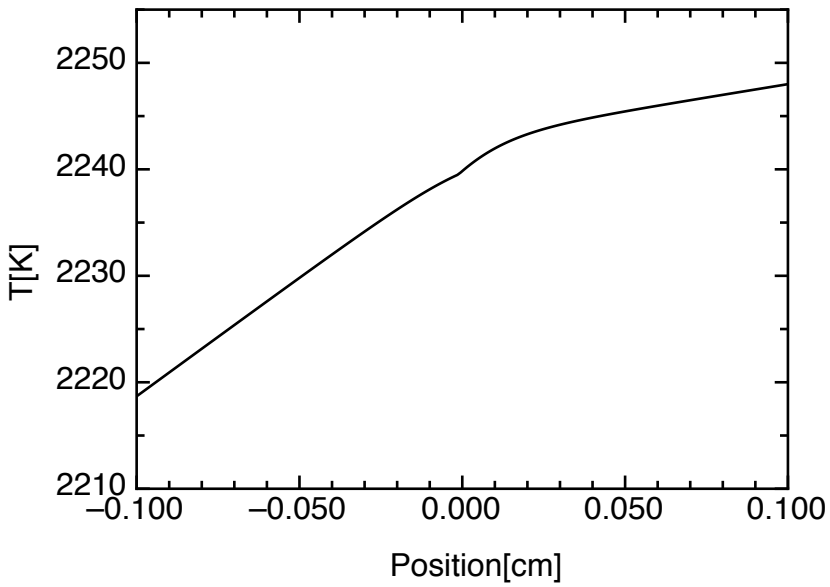

(b) Yb:YAG

Figure 3.3: Calculated temperature profiles for $(Cr, Al)_2O_3$ and Yb:YAG. The profile is calculated along a line 0.01cm parallel to the symmetry axis.

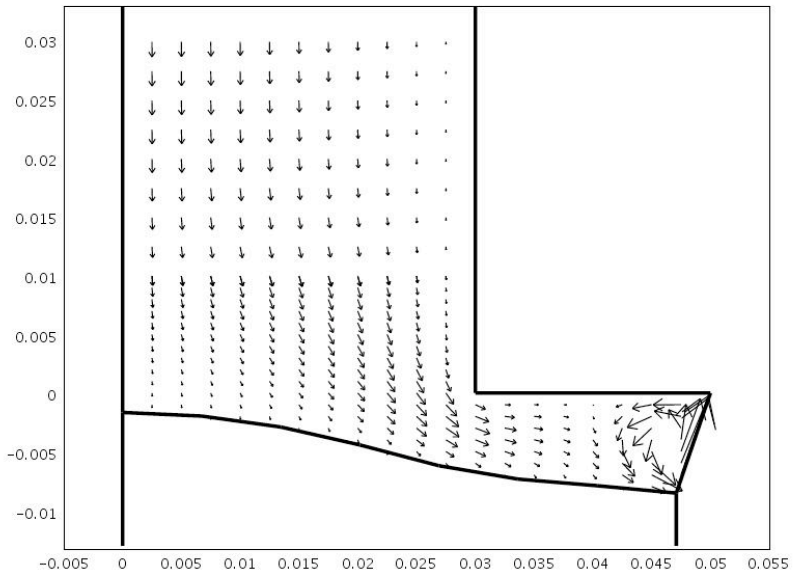

(a) $(Cr, Al)_2O_3$ type 1 growth with 0.5 mm/min

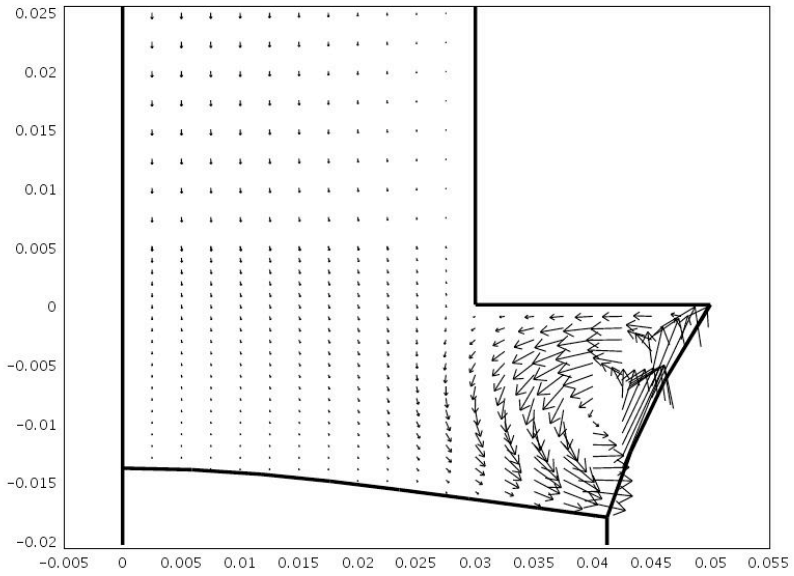

(b) $(Cr, Al)_2O_3$ type 2 growth with 0.5 mm/min

Figure 3.4: (continued)

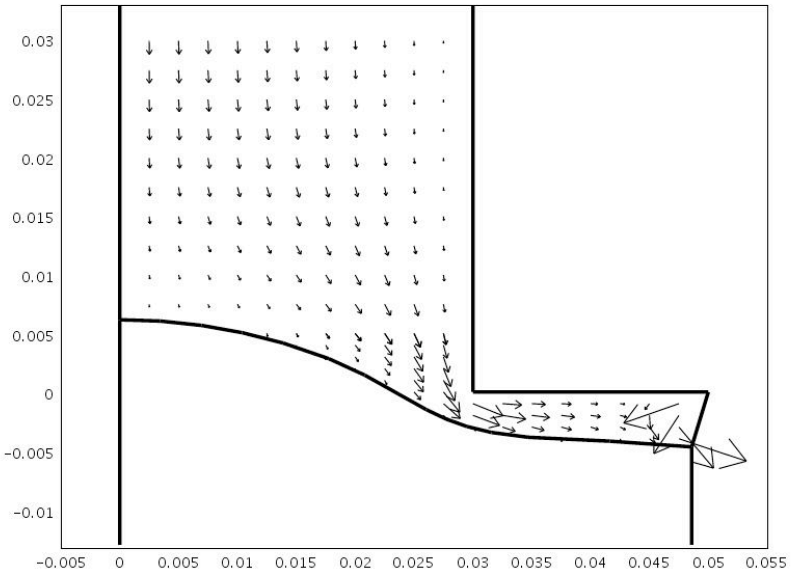

(c) Nd:YAG type 1 growth with very small melt zone and with 0.3 mm/min

Figure 3.4: Calculated flow patterns in the melt. The arrow length is proportional to the velocity

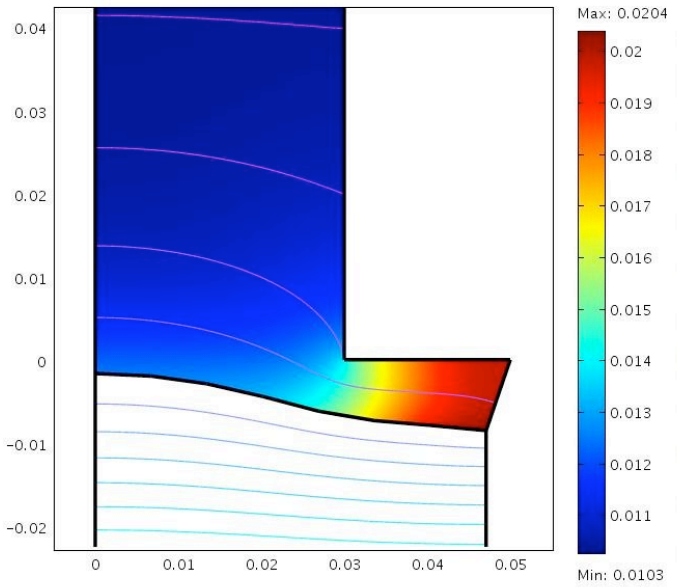

(a) 2D Cr_2O_3-concentration and temperature profile. The distance of the isotherms is 1K. The growth front is the isotherm of the melting point at 2323K.

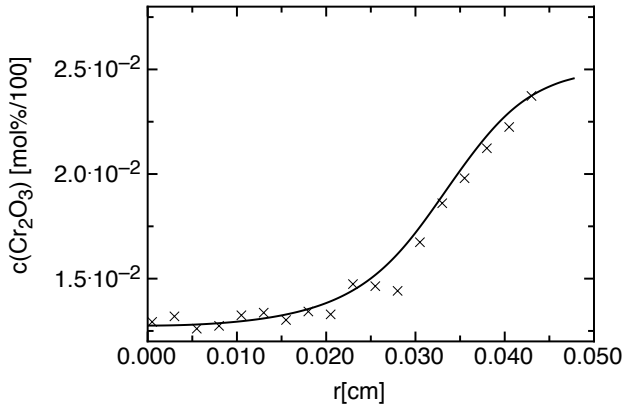

(b) Radial Cr_2O_3-concentration profile in the crystal. The crosses are experimentally measured points (see figure 2.9a

Figure 3.5: Calculated Cr_2O_3-concentration and temperature profiles for $(Cr, Al)_2O_3$ type 1 growth in N_2 atmosphere.

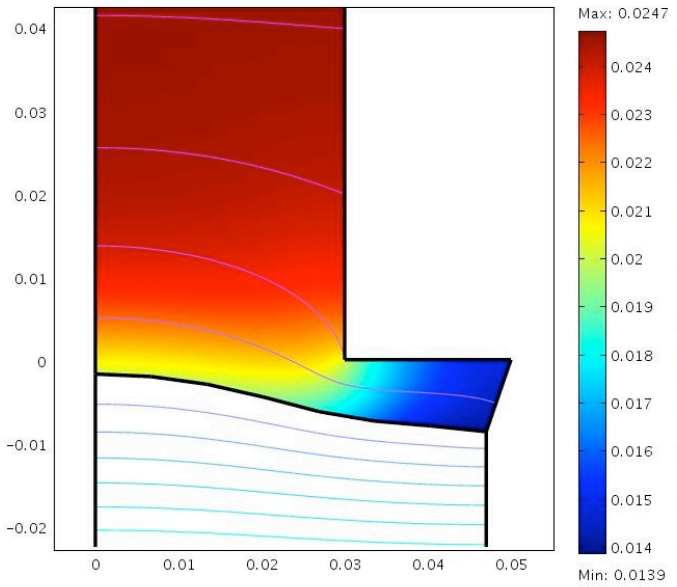

(a) 2D Cr_2O_3-concentration and temperature profile. The distance of the isotherms is 1K. The growth front is the isotherm of the melting point at 2323K.

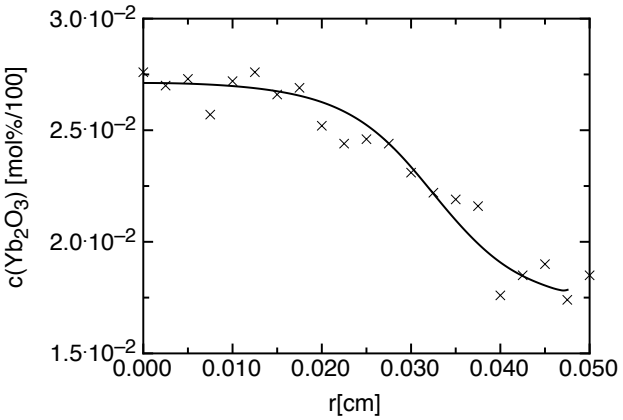

(b) Radial Cr_2O_3-concentration profile in the crystal. The crosses are experimentally measured points (see figure 2.9(b))

Figure 3.6: Calculated Cr_2O_3-concentration and temperature profiles for $(Cr, Al)_2O_3$ type 1 growth in CO_2 atmosphere.

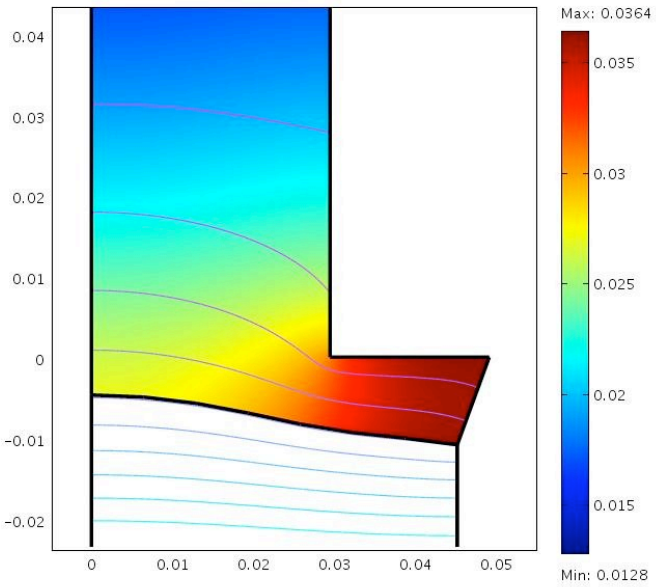

(a) 2D Ga_2O_3-concentration and temperature profile. The distance of the isotherms is 1K. The growth front is the isotherm of the melting point at 2315K.

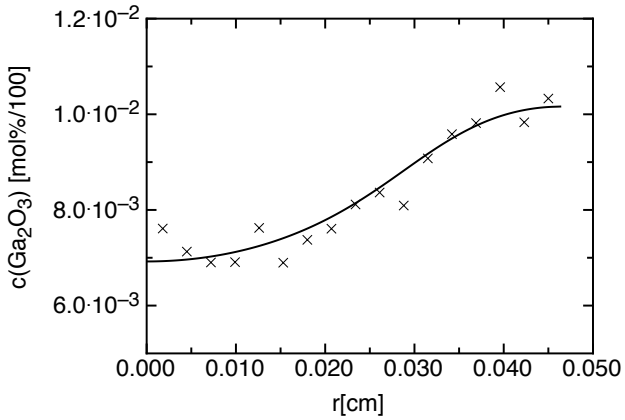

(b) Radial Ga_2O_3-concentration profile in the crystal. The crosses are experimentally measured points (see figure 2.9(c))

Figure 3.7: Calculated Ga_2O_3-concentration and temperature profiles for $(Ga, Al)_2O_3$ type 1 growth in CO_2 atmosphere.

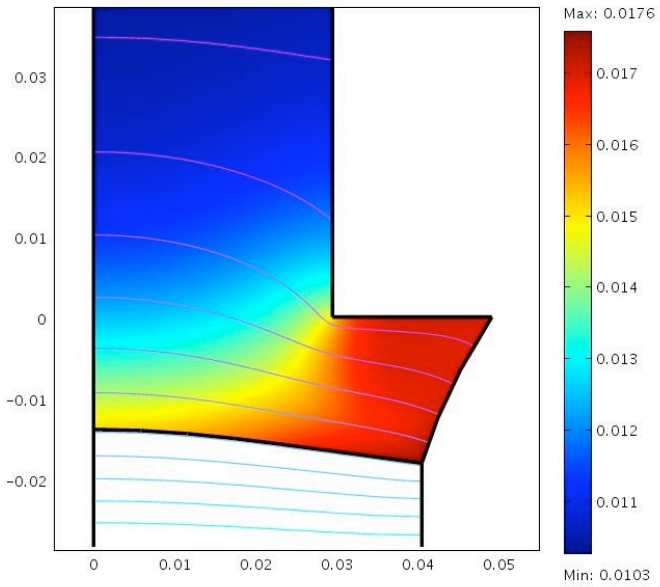

(a) 2D Cr_2O_3-concentration and temperature profile. The distance of the isotherms is 1K. The growth front is the isotherm of the melting point at 2323K.

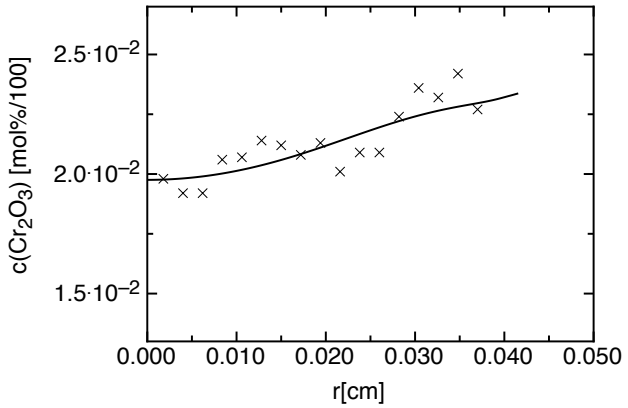

(b) Radial Cr_2O_3-concentration profile in the crystal. The crosses are experimentally measured points (see figure 2.11a)

Figure 3.8: Calculated Cr_2O_3-concentration and temperature profiles for $(Cr, Al)_2O_3$ type 2 growth in N_2 atmosphere.

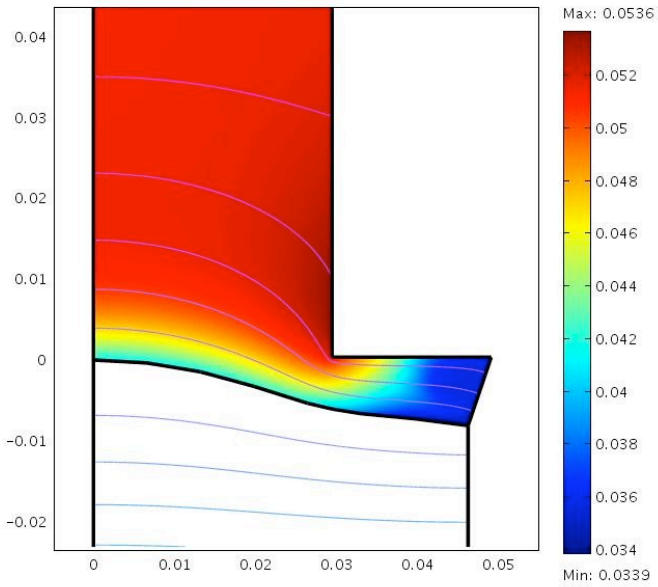

(a) 2D Yb_2O_3-concentration and temperature profile. The distance of the isotherms is 1K. The growth front is the isotherm of the melting point at 2253K.

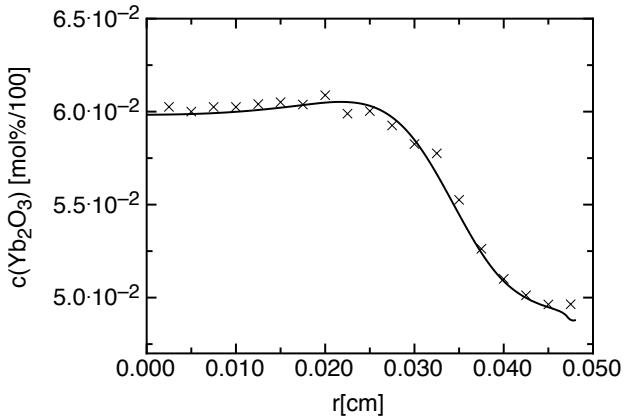

(b) Radial Yb_2O_3-concentration profile in the crystal. The crosses are experimentally measured points (see figure 2.10c)

Figure 3.9: Calculated Yb_2O_3-concentration and temperature profiles for Yb:YAG type 1 growth with 0.3 mm/min pulling speed in N_2 atmosphere.

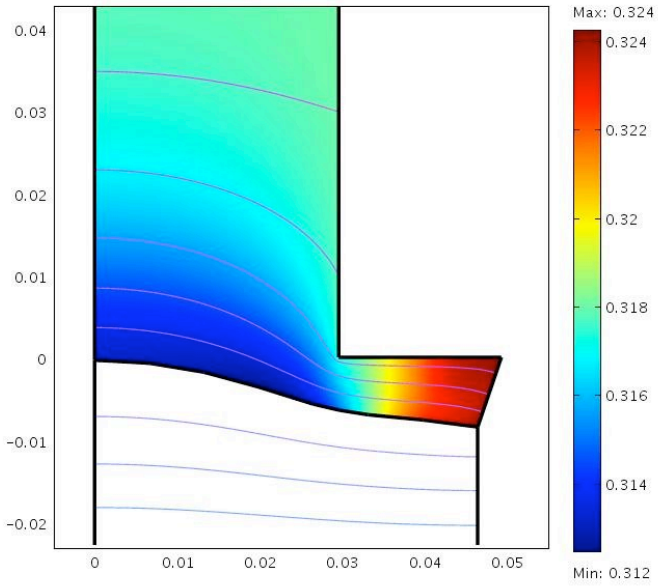

Figure 3.10: Calculated 2D Y_2O_3-concentration and temperature profiles for Yb:YAG type 1 growth with 0.3 mm/min pulling speed in N_2 atmosphere. The growth front is the isotherm of the melting point at 2253K. The distance of the isotherms is 1K.

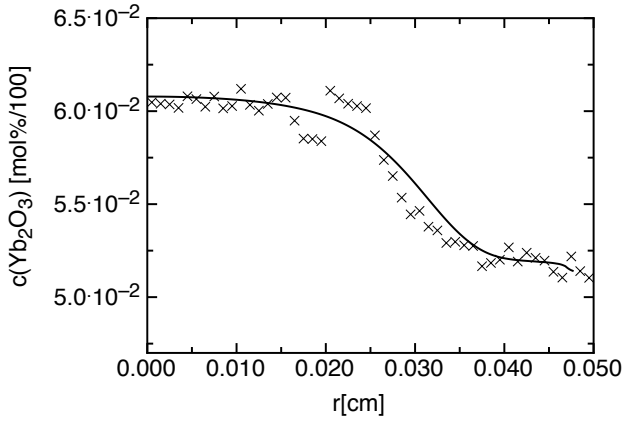

Figure 3.11: Radial Yb_2O_3-concentration profile in the Yb:YAG crystal for type 1 growth with 0.1 mm/min pulling speed in N_2 atmosphere . The crosses are experimentally measured points (see figure 2.10d)

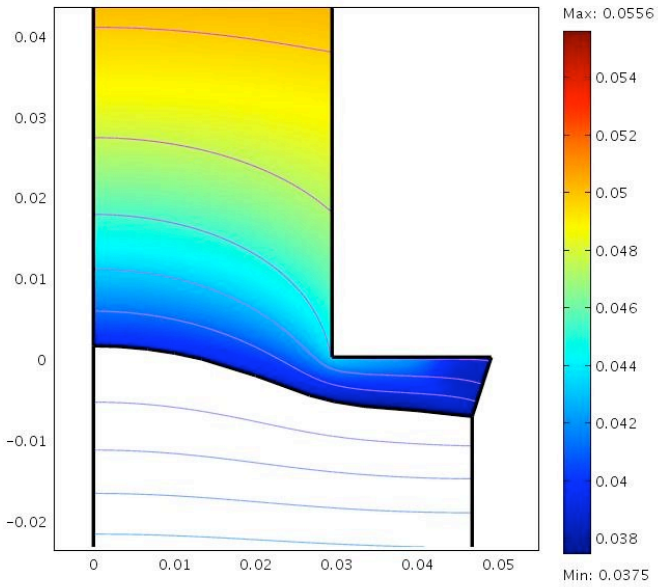

(a) 2D Yb_2O_3-concentration and temperature profile. The distance of the isotherms is 1K. The growth front is the isotherm of the melting point at 2253K.

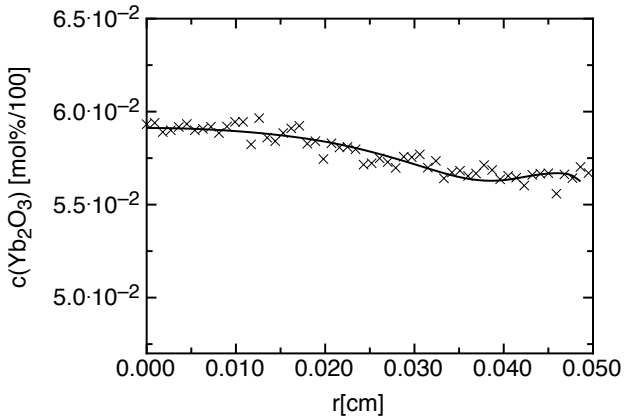

(b) Radial Yb_2O_3-concentration profile in the crystal. The crosses are experimentally measured points (see figure 2.10e)

Figure 3.12: Calculated Yb_2O_3-concentration and temperature profiles for Yb:YAG type 1 growth with 0.01 mm/min pulling speed in N_2 atmosphere.

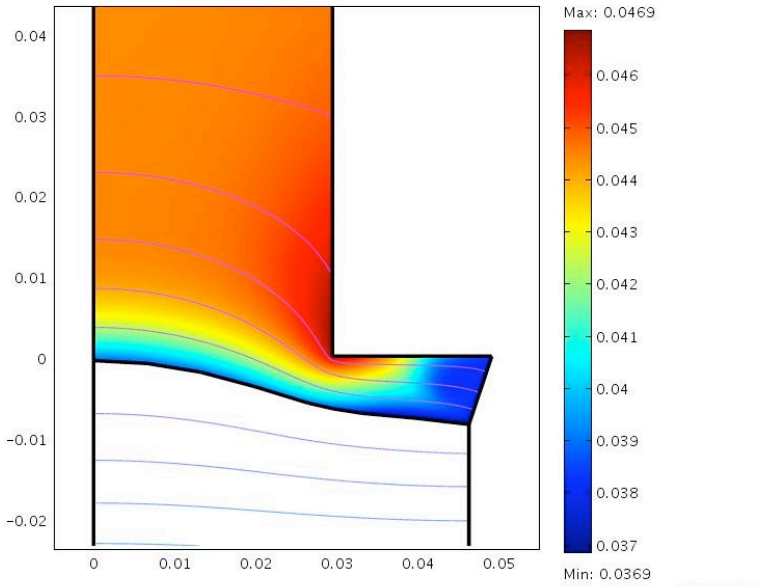

(a) 2D Yb_2O_3-concentration and temperature profile. The distance of the isotherms is 1K. The growth front is the isotherm of the melting point at 2253K.

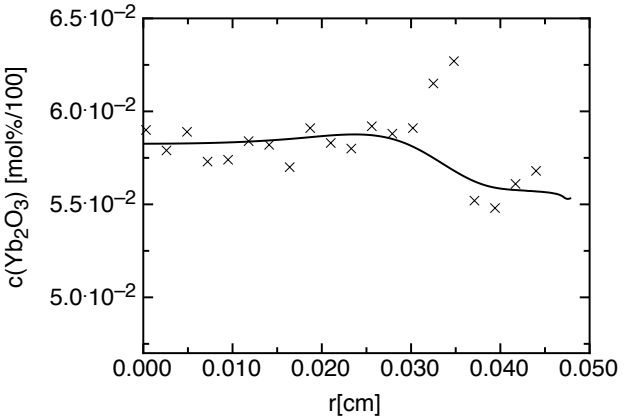

(b) Radial Yb_2O_3-concentration profile in the crystal. The crosses are experimentally measured points (see figure 2.10f)

Figure 3.13: Calculated Yb_2O_3-concentration and temperature profiles for Yb:YAG type 1 growth with 0.3 mm/min pulling speed in forming gas atmosphere.

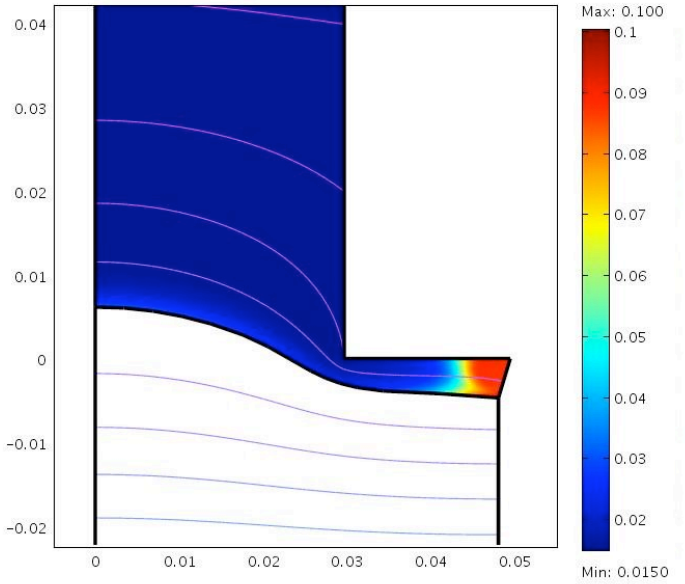

(a) 2D Nd_2O_3-concentration and temperature profile. The distance of the isotherms is 1K. The growth front is the isotherm of the melting point at 2253K.

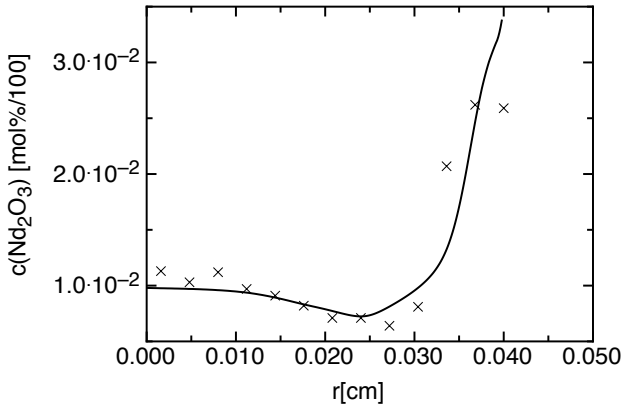

(b) Radial Nd_2O_3-concentration profile in the crystal. The crosses are experimentally measured points (see figure 2.10g)

Figure 3.14: Calculated Nd_2O_3-concentration and temperature profiles for Nd:YAG type 1 growth with 0.3 mm/min pulling speed in N_2 atmosphere.

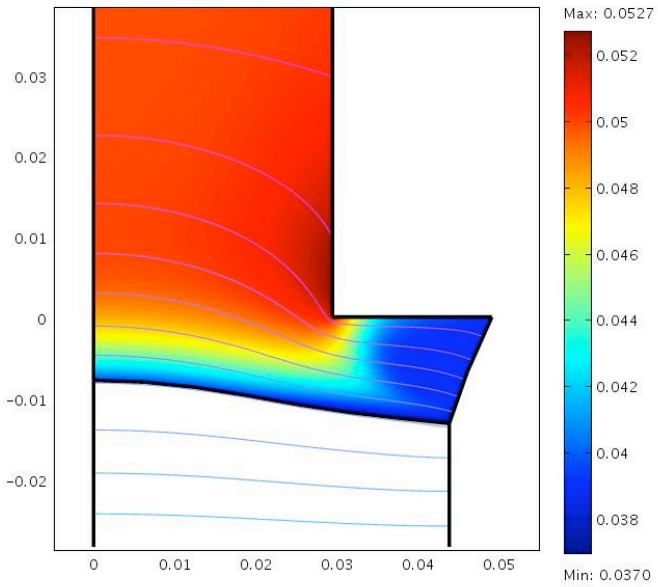

(a) 2D Yb_2O_3-concentration and temperature profile. The distance of the isotherms is 1K. The growth front is the isotherm of the melting point at 2253K.

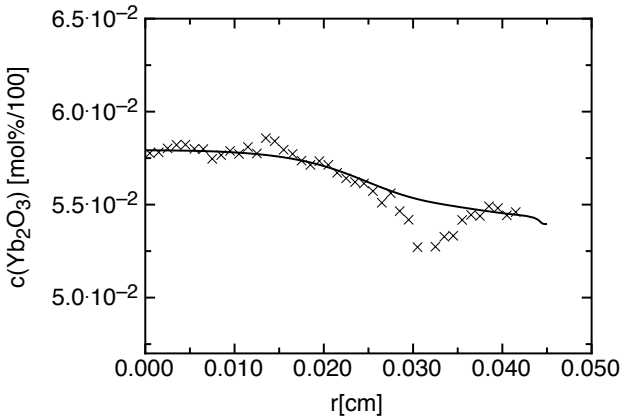

(b) Radial Yb_2O_3-concentration profile in the crystal. The crosses are experimentally measured points (see figure 2.11c)

Figure 3.15: Calculated Yb_2O_3-concentration and temperature profiles for Yb:YAG type 2 growth with 0.3 mm/min pulling speed in N_2 atmosphere.

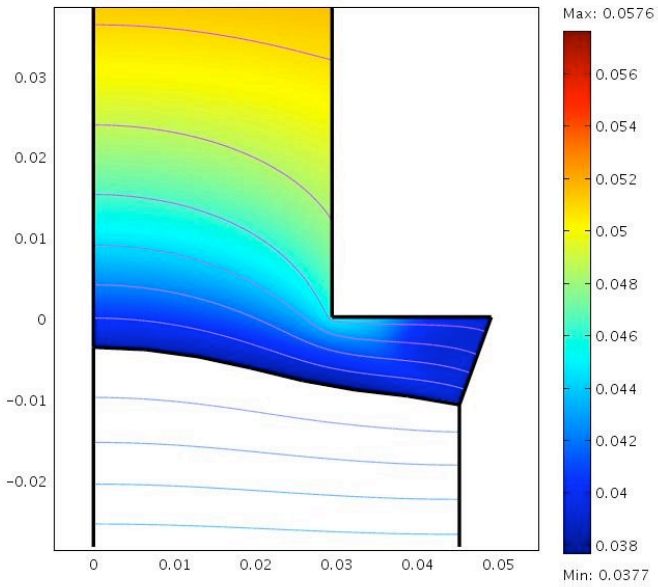

(a) 2D Yb_2O_3-concentration and temperature profile. The distance of the isotherms is 1K. The growth front is the isotherm of the melting point at 2253K.

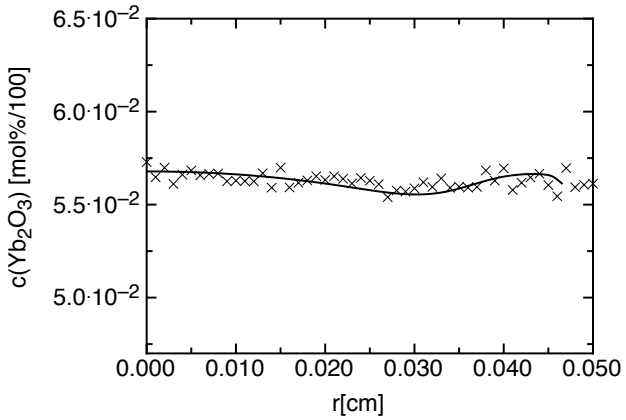

(b) Radial Yb_2O_3-concentration profile in the crystal. The crosses are experimentally measured points (see figure 2.11d)

Figure 3.16: Calculated Yb_2O_3-concentration and temperature profiles for Yb:YAG type 2 growth with 0.01 mm/min pulling speed in N_2 atmosphere.

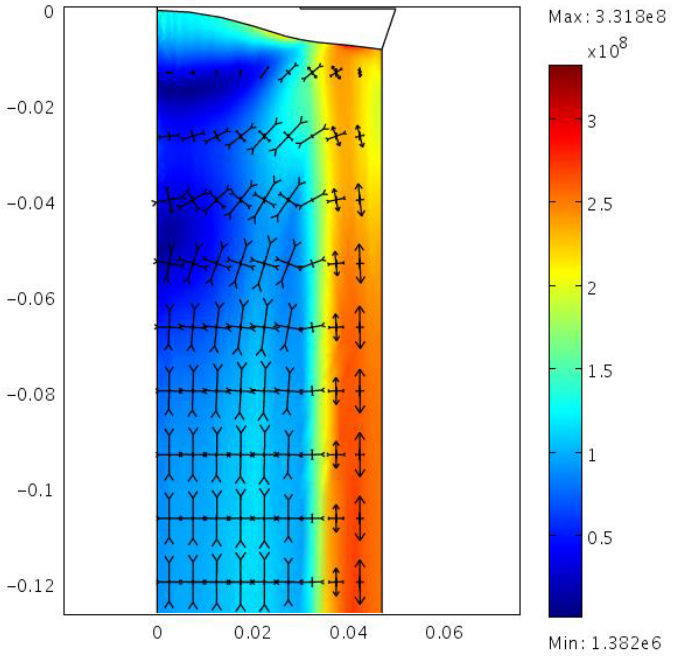

Figure 3.17: Calculated Tresca-stress (in barye) for an Yb:YAG type 1 fiber grown with 0.3 mm/min pulling speed in N_2 atmosphere. Arrows show the direction of the principal stresses

Chapter 4

Irreversible Thermodynamics

4.1 Introduction

In chapter 3, the thermodiffusion was included into the models and there is a need for thermodiffusion factors. Here the basics of thermodiffusion for a two component system [de Groot, 1951] are shortly shown and then a theory for the calculation of thermodiffusion factors is presented.

When a temperature gradient is given in a liquid mixture a concentration gradient will be set up. This will result in a diffusion process, that is called thermodiffusion. The mass diffusion flux is then

$$J = -\rho D \nabla C_1 - \rho D^T C_1 (1 - C_1) \nabla T \tag{4.1}$$

where D, D^T, ρ, C_1, T are the isothermal diffusion coefficient, the thermodiffusion coefficient, the density of the mixture, the concentration of the solute and the temperature, respectively. Between two boundaries in a thermal gradient and in absence of convection a steady state is reached. Then

$$\nabla \ln(C_1) = -\frac{D^T}{D} \nabla T = -\alpha \nabla \ln(T) \tag{4.2}$$

where $\alpha = \frac{D^T T}{D}$ is the thermodiffusion factor, is valid for a dilute mixture. Many theories for the calculation of thermodiffusion factors exist. Besides kinetic theories, reviewed in [van Vaerenbergh et al., 1998] the thermodiffusion factor could be derived by the thermodynamics of irreversible processes and using the theory of Onsager [de Groot, 1951]. Here the heat of transfer is introduced. It can readily be shown, the heat of transfer is the amount of energy transported across a given reference plane at uniform temperature. It is possible to explain the heat of transfer by a rate theory model [Dougherty

and Drickamer, 1955], but there is the need for temperature dependent viscosity data, which are barely available for melts. In [S. Glasstone, 1941], for this purpose some fraction of the latent heat of vaporization was used, but this works only for some materials. The model described below describes the heat of transfer for binary melts by means of the latent heat of fusion, which can be found for many materials in thermodynamic databases [GTT, 2007].

4.1.1 Irreversible thermodynamics

Here systems in which the state variables are dependent on time and space coordinates, like in mixtures of substances in which chemical reactions, diffusion, heat transfer and other cross phenomena can take place, are described. These systems are called continuous systems. Four fundamental equations are necessary to find the expression for the entropy balance.

Fundamental equations

1. Law of conservation of mass for component k

$$\partial\rho_k/\partial t = -\rho_k\vec{\nabla}\vec{v_k} + \nu_k J_c \tag{4.3}$$

where $\rho_k = M_k/V$ is the mass of component k M_k per unit volume V, $\vec{v_k}$ the velocity of k and $\nu_k J_c = \mathrm{V}^{-1} d_i M_k/dt$ the chemical production of k per unit volume ($d_i M_k$ is the amount of substance k taking part in the chemical reaction). This is the balance equation: the local change is equal to the negative divergence of a flow plus some source term giving the production or destruction of substance k. By introducing the flow $\vec{J_k}$ of substance k with respect to the center of mass movement

$$\rho = \sum_k \rho_k = \sum_k M_k/V = M/V = 1/\mathrm{v} \tag{4.4}$$

$$\vec{v} = \sum_k \rho_k \vec{v_k}/\rho \tag{4.5}$$

$$\vec{J_k} = \rho_k(\vec{v_k} - \vec{v}) \tag{4.6}$$

$$\sum_k \vec{J_k} = 0 \tag{4.7}$$

where v is the specific volume, equation 4.3 becomes

$$\rho\partial c_k/\partial t = -\vec{\nabla}\vec{J_k} + \nu_k J_c \tag{4.8}$$

where $c_k = \rho_k/\rho = M_k/M$. Summed over all substances and $\sum_k J_c\nu_k = 0$ equation 4.3 becomes

$$d\rho/dt = -\mathrm{v}^{-2}\mathrm{dv}/dt = -\rho\vec{\nabla}v \tag{4.9}$$

2. Force equation

$$d\vec{v}/dt = -\vec{\nabla}P + \sum_{k=1}^{n} \vec{F_k}\rho_k \tag{4.10}$$

where P is the pressure and F_k is the external force per unit of mass on substance k.

3. Energy equation for u the energy per unit of mass with the exclusion of the barycentric kinetic energy

$$\rho d(\frac{1}{2}\vec{v^2} + u)/dt = -\vec{\nabla}(P\vec{v} + \vec{J_q}) + \sum_{k=1}^{n} \vec{F_k} \cdot \vec{v_k}\rho_k \tag{4.11}$$

where $\vec{J_q}$ is the flow of heat

4. Second law of thermodynamics

$$Tds/dt = du/dt + Pdv/dt + \sum_k \mu_k dc_k/dt \tag{4.12}$$

where s, u, v, μ_k and c are the specific entropy, the specific internal energy, the specific volume, the partial specific chemical potential of component k and the concentration. The differentials are substantial derivatives with respect to the center of mass movement. The equation implies that the specific entropy does not depend on space and time coordinates, but only on the variables u, v, μ_k and c_k.

Entropy balance

When the force equation multiplied by $\vec{v}$ is subtracted from the energy equation, the kinetic energy of the center of gravity is eliminated.

$$\rho du/dt = -P\vec{\nabla}\vec{v} - \vec{\nabla}\vec{J_q} + \sum_k \vec{F_k} \cdot \vec{J_k} \tag{4.13}$$

Introducing this equation with the help of equation 4.9 and the mass balance equation 4.8 into the equation of the second law of thermodynamics 4.12 gives the entropy balance

$$\rho T ds/dt = -\vec{\nabla}\vec{J_q} + \sum_k \vec{F_k} \cdot \vec{J_k} + \sum_k \mu_k \vec{\nabla}\vec{J_k} - J_c \sum_k \mu_k \nu_k \tag{4.14}$$

An alternative form of equation 4.14 is

$$\rho ds/dt = -\vec{\nabla}\left(\frac{\vec{J_q} - \sum \mu_k \vec{J_q}}{T}\right) + \frac{\sum \vec{J_k} \cdot \vec{X_k} + \vec{J_q} \cdot \vec{X_u} + AJ_c}{T} = -\vec{\nabla}J_s + \sigma \tag{4.15}$$

where

$$\vec{X_u} = -(\vec{\nabla}T)/T \tag{4.16}$$

$$\vec{X_k} = \vec{F_k} - \vec{\nabla}(\mu_k/T) \tag{4.17}$$

$$A = \sum_k \mu_k \nu_k \tag{4.18}$$

A is the chemical affinity.
Therefore, the change of the specific entropy is due to the negative divergence of an entropy flow

$$\vec{J_s} = (\vec{J_q} - \sum_k \mu_k \vec{J_k})/T \tag{4.19}$$

and an entropy production with a source strength

$$\sigma = (\vec{J_q} \cdot \vec{X_u} + \sum_k \vec{J_k} \cdot \vec{X_k} + AJ_c)/T \tag{4.20}$$

which is a sum of the products of "fluxes" $\vec{J_q}$, $\vec{J_k}$ and J_c and corresponding "forces" $\vec{X_u}$, $\vec{X_k}$ and A.

Phenomenological equations

With the help of the scheme of Onsager's theory the relation between the "fluxes" and "forces" can be approximated linearly to the phenomenological equations

$$\vec{J_i} = \sum_{i=1}^{n} L_{ik}\vec{X_k} + L_{iu}\vec{X_u} \tag{4.21}$$

$$\vec{J_u} = \sum_{k=1}^{n} L_{uk}\vec{X_k} + L_{uu}\vec{X_u} \tag{4.22}$$

$$J_c = LA \tag{4.23}$$

Thermodiffusion

The general case of a mixture of n components in a non-uniform temperature field gives an entropy production

$$T\sigma = \sum_{k=1}^{n} \vec{J_i} \cdot \vec{X_i} + \vec{J_q} \cdot \vec{X_u} = \sum_{i=1}^{n-1} \vec{J_i} \cdot (\vec{X_i} - \vec{X_n}) + \vec{J_q} \cdot X_u \tag{4.24}$$

With the help of equation 4.7 it can be derived that between the phenomenological coefficients the following relations exist :

$$\sum_{k=1}^{n} L_{ik} = 0, \sum_{k=1}^{n} L_{uk} = 0 \tag{4.25}$$

$$\sum_{i=1}^{n} L_{ik} = 0, \sum_{i=1}^{n} L_{iu} = 0 \tag{4.26}$$

and the reciprocal Onsager relations

$$L_{ik} = L_{ki}, \; L_{iu} = L_{ui} \tag{4.27}$$

With the help of equation 4.25 the coefficients $L_{in}\,(i = 1, 2, ..., n)$ and L_{un} can be eliminated from the phenomenological equations 4.21 and 4.22.

$$\vec{J_i} = \sum_{k=1}^{n-1} L_{ik}(\vec{X_k} - \vec{X_n}) + L_{iu}\vec{X_u} \;\; (i = 1, 2, ..., n-1) \tag{4.28}$$

$$\vec{J_q} = \sum_{k=1}^{n-1} L_{uk}(\vec{X_k} - \vec{X_n}) + L_{uu}\vec{X_u} \tag{4.29}$$

This gives $n - 1$ independent flows J_i. With the help of equation 4.26 the coefficients $L_{ni}\,(i = 1, 2, ..., n)$ and L_{nu} can be eliminated and gives the expression

$$\vec{J_n} = -\sum_{i=1}^{n-1} \vec{J_i} \tag{4.30}$$

which indicates, that the flow $\vec{J_n}$ is dependent on the other flows. The coefficients L_{iu} can be defined by introducing new coefficients Q_k^*

$$L_{iu} = \sum_{k=1}^{n-1} L_{ik} Q_k^* \tag{4.31}$$

and equation 4.28 gets

$$\vec{J_i} = \sum_{k=1}^{n-1} L_{ik}(\vec{X_k} - \vec{X_n} + Q_k^* \vec{X_u}) \tag{4.32}$$

When the equations 4.28 are multiplied by Q_i^*, added, then the result is subtracted from equation 4.29, and the Onsager reciprocal relations 4.27 are applied

$$\vec{J_q} = \sum_{i=1}^{n-1} Q_i^* \vec{J_i} + (L_{uu} - \sum_{i=1}^{n-1} L_{iu} Q_i^*)\vec{X_u} \tag{4.33}$$

it gives the physical interpretation of Q_k^* as the heat transported across a given reference plane at uniform temperature by unit of mass of compound k and is called the "heat of transfer".

4.2 Theoretical model for thermodiffusion factors

Equation 4.28 in absence of external forces becomes with the "forces" 4.16 and 4.17

$$J_i = \sum_{k=1}^{n-1} L_{ik} \left(- \sum_{j=1}^{n-1} T \vec{\nabla} [(\mu_k - \mu_n)/T] - Q_k^*) \frac{\nabla T}{T} \right) \tag{4.34}$$

Since μ_k is a function of T, P and the concentrations c_j it follows

$$T \vec{\nabla} (\mu_k / T) = -h_k \vec{\nabla} T / T + \mathrm{v_k} \vec{\nabla} P + \sum_{j=1}^{n-1} \frac{\partial (\mu_k - \mu_n)}{\partial c_j} \nabla c_j \tag{4.35}$$

and equation 4.34 becomes

$$J_i = \sum_{k=1}^{n-1} L_{ik} \left(- \sum_{j=1}^{n-1} \frac{\partial (\mu_k - \mu_n)}{\partial c_j} \nabla c_j - (Q_k^* - h_k + h_n) \frac{\nabla T}{T} \right) \tag{4.36}$$

where $h_k = \mu_k + T s_k$ is the partial specific enthalpy. For two components with the help of the Gibbs-Duhem relation $c_1 d\mu_1 + c_2 d\mu_2 = 0$ and $c_1 + c_2 = 1$ at constant T and p equation (4.36) becomes

$$J_1 = -J_2 = L_{11} \left(-c_2^{-1} \frac{\partial \mu_1}{\partial c_1} \nabla c_1 - (Q_1^* - h_1 + h_2) \frac{\nabla T}{T} \right) \tag{4.37}$$

Let us now consider a microscopic region of the fluid which consists of one half of component 1 and one half of component 2 in mass fractions. The mean specific internal energy is then $u = \frac{1}{2}(u_1 + u_2)$ and the mean specific volume $\mathrm{v}_{mspec} = \frac{1}{2}(\mathrm{v}_1 + \mathrm{v}_2)$ with u_k and v_k as the partial specific internal energy and the partial specifc volume of component k, respectively. When the atoms of component 1 in this volume are moved to the next equilibrium position an amount of energy $Q_1^* dc_1$, which follows from the definition of Q^*, will be transferred by the diffusion flow. Since we consider temperature and pressure are constant a quantity of heat dq has to be absorbed and an amount of work $p\mathrm{v}_1 dc_1$ has to be done. When a mass fraction dc_1 of component 1 is transfered to the next equilibrium position also the same quantity of component 2 in unit of mass of component 2 is transfered from this position to the old equilibrium position of component 1. So there is additionally a work $p\mathrm{v}_2 dc_2$ done. Therefore, the change of the internal energy can then be written as

$$du = \frac{1}{2}(-u_1 dc_1 + u_2 dc_2) = -\frac{1}{2} Q_1^* dc_1 + dq + \frac{1}{2}(p\mathrm{v}_1 dc_1 - p\mathrm{v}_2 dc_2) \tag{4.38}$$

where u, Q^*, p, v, dq are the partial specific internal energy, the specific heat of transfer, the pressure, the partial specific volume and the heat absorbed of the region of the fluid. With $h = u + p\mathrm{v}$ the heat dq absorbed in this region of the fluid is then

$$dq = \frac{1}{2}\left[(Q_1^* - h_1)dc_1 + h_2 dc_2\right] \tag{4.39}$$

Therefore, we have to scale the second term of equation 4.37 by a factor of $\frac{1}{2}$ and get finally

$$J_1 = -J_2 = L_{11}\left(-c_2^{-1}\frac{\partial \mu_1}{\partial c_1}\nabla c_1 - \frac{1}{2}(Q_1^* - h_1 + h_2)\frac{\nabla T}{T}\right) \tag{4.40}$$

To get the thermodiffusion factor we can put the coefficient of ∇c_1 and the coefficient of ∇T of equation 4.40 equal to $-\rho D_{12}$ and $\rho D_{12}^T c_1 c_2$, respectively. D_{12} and D_{12}^T are the diffusion coefficient and the thermodiffusion coefficient of component 1 in 2, respectively. [de Groot, 1951]

$$\alpha = \frac{D_{12}^T T}{D_{12}} = \frac{1}{2}\frac{Q_1^* - h_1 + h_2}{c_1 \frac{\partial \mu_1}{\partial c_1}} \tag{4.41}$$

To find a physical explanation of the heat of transfer the model of Garai [Garai, 2004] for the physical interpretation of the latent heat of fusion is useful. It shows, the latent heat of fusion is the energy necessary to overcome the viscous drag and depends on the molar volume of the fluid, V_{mol}.

$$L_f = \frac{V_{mol}\eta v_{therm}}{(n+1)^2 d} \tag{4.42}$$

where L_f, V_{mol}, v_{therm}, d, η and n are the molar latent heat of fusion, the molar volume of the melt, the thermal velocitiy of the atoms, the atomic distance, the viscosity and the number of coupled atoms, respectively. When we are already in the molten state of a mixture of two components with different molar volume and we consider a microscopic region of the fluid where component 2 is exchanged with component 1 by a diffusional flow described above, we have a mean molar volume of this region

$$V_{mmol} = \frac{1}{2}(V_1 + V_2) \tag{4.43}$$

The latent heat of fusion of component 1 is then increased by the fraction of the mean molar volume to the molar volume of component 1. Therefore, the additional energy transported with component 1, which is by definition Q_1^*,

is the difference of the latent heat of fusion of component 1 in the mean molar volume of the mixture and the latent heat of fusion of the pure component 1

$$Q_1^* = \frac{L_f}{m_1}\left(\frac{\frac{1}{2}(V_1+V_2)}{V_1} - 1\right) \tag{4.44}$$

where m_1 is the molar mass of component 1. The latent heat of fusion is the difference of the entropy of the liquid and the entropy of the solid state at the melting temperature multiplied by the melting temperature. But in general the transport phenomena should be described at a different temperature than the melting temperature. So we have to use the difference of the entropy of the liquid and the entropy of the solid at the this temperature multiplied by this temperature. The entropy of the liquid and solid state can be found in the FactSage database, where the thermodynamic data is expressed by extrapolated polynomials. When the temperature of the transport process described is higher than the melting temperature of one of the pure components, where the solid state of this component naturally does not exist, the entropy of the solid state of this component at the process temperature is approximated by the extrapolated entropy function taken from the database. So the heat of transfer becomes

$$Q_1^* = \Delta s_1^{ls}(T) T \frac{V_{mmol} - V_{mol1}}{V_{mol1}} \tag{4.45}$$

where $\Delta s_1^{ls}(T)$ is the partial specific entropy difference between solid and liquid state of component 1 at temperature T. The derivative of the chemical potential of component 1 with respect to c_1 for diluted mixtures in units of mass 1 with $c_1 + c_2 = 1$ and mass fractions c_i is

$$\frac{\partial \mu_1}{\partial c_1} = \frac{\partial\left(\frac{R}{m_1} T ln\left(\frac{c1\rho_1}{c_1\rho_1 + c_2\rho_2}\right)\right)}{\partial c_1} = \frac{RTV_2m_1}{c_1(c_1V_1m_2 + V_2m_1 - V_2m_1c_1)} \tag{4.46}$$

where ρ_i is the density of component i and R the gas constant. The final equation of the thermodiffusion factor becomes then

$$\alpha = \frac{1}{2}\frac{(\Delta s_1^{ls}(T) T \frac{V_{mmol}-V_{mol1}}{V_{mol1}} - h_1 + h_2)(c_1V_1m_2 + V_2m_1 - V_2m_1c_1)}{RTV_2m_1} \tag{4.47}$$

4.3 Calculations

The model was compared to experimental results of van Vaerenbergh et al. [van Vaerenbergh et al., 1998]. They made measurements of thermodiffusion

Alloy	c_1 [wt%]	Mean temp. T [K]	Experimental α	Calc. α
Bi-Sn	4.0	773	0.758 ± 0.066	0.785
Ag-Sn	0.04	773	-0.175 ± 0.049	-0.162
Co-Sn	0.04	773	-1.86 ± 0.040	-1.712
Au-Sn	0.07	823	0.837 ± 0.012	0.934
Cr_2O_3-Al_2O_3	2.0	2314	-	-0.015·T
Yb_2O_3-Al_2O_3	13.0	2263	-	-0.045·T

Table 4.1: Experimental [van Vaerenbergh et al., 1998] and calculated (from equation 4.47) thermodiffusion factors of some diluted Sn alloys and of compounds used in this thesis

factors of diluted tin alloys with gold, silver, bismuth and cobalt in micro gravity. For the calculation using the described theory, the entropy difference and the enthalpy of the components have been taken from the FactSage database [GTT, 2007]. The experimental results compared to the calculated values are given in table 4.1. The calculated thermodiffusion factors show a reasonable agreement to the experimental thermodiffusion factors. Therefore, the model was used to calculate the thermodiffusion factors of the compounds used for the numerical simulation in chapter 3.

Acknowledgements

First of all, I want to express my gratitude to Prof. Dr. Roberto Fornari who gave me the opportunity to work in the Leibniz Institute for Crystal Growth. I am very grateful for his support and supervision of my work. He has always been there with advice and has always been ready for fruitful discussions.

I am very grateful to my supervisor Dr. Detlef Klimm for supporting me with his scientific experience and for encouraging me in every phase of this work. I would like to thank Steffen Ganschow for helpful discussions and Dr. Rainer Bertram for his support in chemical analyses.

I also would like to thank Dr. Reinhard Uecker and all members of the oxide group for creating an enjoyable atmosphere and being always ready to help me.

I would like to thank Albert Kwasniewski and Dr. Martin Schmidbauer for X-Ray measurments.

In particular I would like to thank Dr. Dieter Rhede from the Geo-Forschungs-Zentrum Potsdam for giving me the possibility to do WDS measurements and for all the helpful discussions.

Bibliography

J.S. Abell, I.R. Harris B. Cockayne, and J.G. Plant. DTA study of zone-refined $LiREF_4$. *J. Mat. Sc.*, 11:1807, 1976.

ACerS-NIST. *Phase Equilibria Diagrams Database*, Version 3.0.1.

R.L. Aggarwal, D.J. Ripin, J.R. Ochoa, and T.Y. Fan. Measurement of thermo-optic properties of $Y_3Al_5O_{12}$, $Lu_3Al_5O_{12}$, $YAIO_3$, $LiYF_4$, $LiLuF_4$, BaY_2F_8, $KGd(WO_4)_2$ and $KY(WO_4)_2$ laser crystals in the 80–300K temperature range. *J. Appl. Phys*, 98:103514, 2005.

J. Banerjee and K. Muralidhar. Role of internal radiation during Czochralski growth of YAG and Nd:YAG crystals . *Int. J. Therm. Sc. 45*, pages 151–167, 2006.

T. Bhutta, J.I. Mackenzie, D.P. Shepherd, and R.J. Beach. Spatial dopant profiles for transverse-mode selection in multimode waveguides. *J. Opt. Soc. Am. B*, 19(7):1539, 2002.

J.A. Burton, R.C. Prim, and W.P. Slichter. The distribution of solute in crystals grown from melt. *J. Chem. Phys.*, 21:1987, 1953.

Femlab 3.3a. Comsol Multiphysics GmbH, Berliner Str. 4, D-37073 Göttingen, http://www.femlab.de, 2007.

S.R. Coriell, R.F. Boisvert, and R.G. Rehm. Lateral solute segregation during unidirectional solidificationof a binary alloy with a curved solid liquid interface : II large deviations from planarity. *J. Cryst. Growth*, 54:167, 1981.

S.R. de Groot. *Thermodynamics of irreversible processes.* North-Holland Publ. Amsterdam, 1951.

S. Degterov and A.D. Pelton. Critical Evaluation and Optimization of the Thermodynamic Properties and Phase Diagrams of the CrO-Cr_2O_3, CrO-Cr_2O_3-Al_2O_3, and CrO-Cr_2O_3-CaO Systems. *J. Phase Equilb.*, 17:476, 1996.

B. Denker, B. Galagan, V. Osiko, S. Sverchkov, A.M. Balbashov, J.E. Hellstroem, V. Pasiskevicius, and F. Laurell. Yb^{3+}, Er^{3+} : YAG at high temperatures: Energy transfer and spectroscopic properties. *Opt. Comm.*, 271: 142, 2007.

J. Didierjean, D. Perrodin, M. Castaing, F. Balembois, K. Lebbou, A. Brenier, P. Georges, J.M. Fourmigue, and O. Tillement. High-power laser with Nd : YAG single-crystal fiber grown by the micro-pulling-down technique. *Opt. Lett.*, 31(23):3468, 2006.

M.J.F. Digonnet and C.J. Graeta. Theoretical analysis of optical fiber laser amplifiers and oscillators. *Appl. Opt.*, 24:333, 1985.

E.I. Dougherty and H.G. Drickamer. A theory of thermal diffusion in liquids. *J. Chem. Phys.*, 23:295, 1955.

D.E. Eakins, M. Held, M.G. Norton, and D.F. Bahr. A study of fracture and defects in single crystal YAG. *J. Cryst. Growth*, 267:502, 2004.

Z. Galazka, D. Schwabe, and H. Wilke. Influence of internal radiation on the heat transfer during growth of YAG single crystals by the Czochralski method. *Cryst. Res. Technol.*, 38:859, 2003.

S. Ganschow and D. Klimm. Growth of olivine single crystals by the micro-pulling-down method. *Cryst. Res. Technol.*, 40:359, 2005.

J. Garai. Physical model for the latent heat of fusion. *Chem. Phys. Lett.*, 398:98, 2004.

G.V. Gibbs and J.V. Smith. Refinement of crystal structure of synthetic pyrope. *Am. Min.*, 50:2023, 1965.

J. Goldstein. *Scanning Electron Microscopy and X-Ray Microanalysis.* Plenum Press, 1992.

FactSage 5.5. GTT Technologies, Kaiserstr. 100, 52134 Herzogenrath, Germany, http://www.gtt-technologies.de, 2007.

K. Kitamura, Y. Miyazawa, Y. Mori, S. Kimura, and M. Higuchi. Origin of difference in lattice spacings between on- and off-facet regions of rare-earth garnets grown from the melt. *J. Cryst. Growth*, 64:207, 1983.

H. Kopetsch. Numerical simulation of the interface inversion in Czochralski growth of oxide crystals. *J. Cryst. Growth*, 102:505, 1990.

S.A. Korpela, J. Ni, A. Chait, and M. Kassemi. Radiative heat transfer in fiber drawing and crystal pulling. *J. Cryst. Growth*, 165:455, 1996.

W.E. Langlois. Digital simulation of Czochralski bulk flow in microgravity. *J. Cryst. Growth*, 48:25, 1980.

C.Y. Lo, P.L. Huang, T.S. Chou, L.M. Lee, T.Y. Chang, S.L. Huang, L. Lin, H.Y. Lin, and C. Ho. Efficient Nd:$Y_3Al_5O_{12}$ crystal fiber laser. *Jpn. J. Appl. Phys.*, 41:L1228, 2002.

P. Malankiewicz, J. Szade, A. Winiarski, and Ph. Daniel. Bridgman-Stockbarger growth and X-ray photoelectron spectroscopy study of $LiY_{1-x}Eu_xF_4$ crystals. *Cryst. Res. Technol.*, 40:410, 2005.

K. Nassau. *Gems made by man.* Gemological Institute of America, 1980.

R.C. Pastor, M. Robinson, and W. M. Akutagawa. The relationship between crystal growth behaviour and constitution in the systems LiF-LuF_3, LiF-ErF_3 and LiF-YF_3. *Mat. Res. Bull.*, 10:501, 1975.

RP-Photonics. *Encyclopedia of Laser Physics*, 2008. URL `http://www.rp-photonics.com/yag_lasers.html`.

P. Rudolph and T. Fukuda. Fiber crystal growth from the melt. *Cryst. Res. Technol.*, 34(1):3, 1999.

H. Eyring S. Glasstone, K.J. Laidler. *Theory of Rate Processes.* McGraw-Hill Book Co., N.Y., 1941.

A.M.E. Santo, I.M. Ranieri, G.E.S. Brito, B.M. Epelbaum, S.P. Morato, N.D. Vieira Jr., and S.L. Baldochi. Growth of $LiYF_4$ single-crystalline fibres by micro-pulling-down technique. *J. Cryst. Growth*, 275(3-4):528, 2004.

K. Shimamura, H. Sato, A. Bensalah, V. Sudesh, H. Machida, N. Sarukura, and T. Fukuda. Crystal growth of fluorides for optical applications. *Cryst. Res. Technol.*, 36:801, 2001.

A.E. Siegman. Propagating modes in gain-guided optical fibers. *J. Opt. Soc. Am. A*, 20(8):1617, 2003.

B. P. Sobolev, P. P. Fedorov, D. B. Shteynberg, B. V. Sinitsyn, and G. S. Shakhkalamian. On the problem of polymorphism and fusion of lanthanide trifluorides. i. the influence of oxygen on phase transition temperatures. *J. Sol. Stat. Chem.*, 17:191, 1976.

M. Swirkowicz, M. Skorczakowski, J. Jabczynski, A. Bajor, E. Tymicki, B. Kaczmarek, and T. Lukasiewicz. Investigation of structural, optical and lasing properties of YAG:Yb single crystals. *Opto-electronics review*, 13:213, 2005.

M.H. Tavakoli. *Numerical analysis of seeding process during Czochralski growth of oxide single crystals*. PhD thesis, Brandenburgisch Technische Universität Cottbus, 2006.

R.E. Thoma, H. Insley, C.F. Weaver, H.A. Friedman, L.A. Harris, and H.A. Yakel. Phase equilibria in the system LiF-YF_3. *J. Phys. Chem.*, 65:1096, 1961.

S. Uda, J. Kon, K. Shimamura, J. Ichikawa, K. Inaba, and T. Fukuda. Interface field-modified solute partitioning during Mn : $LiNbO_3$ crystal fiber growth by micro-pulling down method. II. Radial distribution analysis. *J. Cryst. Growth*, 182:403, 1997.

S. van Vaerenbergh, J.P. Garandet, J.P. Praizey, and J.C. Legros. Reference soret coefficients of natural isotopes and diluted alloys of tin. *Phys. Rev. E*, 58(2):1866, 1998.

B. Velickov. Absorption spectra of ruby. private communication, 2006.

Wikipedia. *Ruby*, 2008. URL `http://en.wikipedia.org/wiki/Ruby`.

K.Th. Wilke and J. Bohm. *Kristallzüchtung*. Verlag Harry Deutsch Frankfurt/Main, 1988.

Q. Xiao and J.J. Derby. Heat transfer and interface inversion during the Czochralski growth of Yttrium Aluminium Garnet (YAG) and Gadolinium Gallium Garnet (GGG). *J. Cryst. Growth*, 139:147, 1994.

H. Yagi, T. Yanagitani, T. Numazawa, and K. Ueda. The physical properties of transparent $Y_3Al_5O_{12}$ Elastic modulus at high temperature and thermal conductivity at low temperature. *Ceram. Int.*, 33:711, 2007.

D.H. Yoon, P. Rudolph, and T. Fukuda. Morphological aspects of potassium lithium niobate crystals with acicular habit grown by the micro-pulling-down method. *J. Cryst. Growth*, 144:207, 1994.

List of Figures

List of Tables

Selbständigkeitserklärung

Hiermit erkläre ich, die vorliegende Dissertation selbständig angefertigt und nur die angegebene Literatur und Hilfsmittel verwendet zu haben.

Dirk Maier